STRUCTURE PREDICTION, GROWTH, AND CHARACTERIZATION OF PEROVSKITES

A Dissertation

Presented to the Faculty of the Graduate School

of Cornell University

in Partial Fulfillment of the Requirements for the Degree of

Doctor of Philosophy

by

Eva Helena Smith

August 2017

STRUCTURE PREDICTION, GROWTH, AND CHARACTERIZATION OF PEROVSKITES

Eva Helena Smith, Ph.D.

Cornell University 2017

The heart of materials science is understanding the relationship between structure (how molecules are connected at the atomic level, as well as in hierarchical building blocks) and properties. Historically this has been achieved by studying the properties of materials in hand, either found in nature or synthesized in the laboratory. As the understanding of the relationship between structure and properties has grown, and our ability to calculate and in particular to solve Schrödinger's equation for solids has improved, so too has our desire and ability to predict structures with enhanced properties through computation.

In this thesis I do each of those three tasks – prediction, synthesis, and characterization – on a system that is of interest in its own right and which I hope may yield results that can be applied to other materials systems as well. All of these systems are materials in the highly-versatile perovskite structure, which can accommodate most of the elements of the periodic table. Perovskites have been the object of much study in the laboratory as well as being used extensively in industrial applications, with such properties as ferroelectricity, piezoelectricity, ferromagnetism, and superconductivity.

First, I delineate the chemical factors that determine the ground-state structure of $CsPbF_3$. I use $CsPbF_3$ as a guide to search for rules to rationally design from first principles new polar fluoride and halide perovskites with stoichiometry ABX_3 and as a model compound to study the interactions of lone pair electrons, antipolar structural distortions, and the different coordination requirements of A and B cations. I show that the coordination requirements of the A-site cation Cs^+ and the stereoactivity of the B-site lone pair cation Pb^{2+} compete or cooperate via the anionic displacements that accompany polar

distortions, and consider the generalizability of my findings to other halide and oxide perovskites.

Next, I describe the chemical reactions that govern growth of $PbTiO_3$ and $BiFeO_3$ by molecular-beam epitaxy. $PbTiO_3$ and $BiFeO_3$ are among two dozen complex oxides that are grown by MBE using thermodynamic composition control. I show that kinetics are also critical to growing phase-pure materials by this method, and that oxidation of lead or bismuth can be the rate-limiting step in the synthesis of $PbTiO_3$ or $BiFeO_3$, respectively, from component elements. I establish a simple kinetic model for the growth of these materials that complements the existing thermodynamic theories and delineate the factors controlling the range of temperatures and pressures in which kinetics permit these materials to be grown by thermodynamic control.

Finally, I detail how to predict and verify the presence of hybrid reflections in x-ray diffraction patterns of phase-pure epitaxial oxide thin films grown on single-crystal substrates. I present symmetric θ-2θ scans of such films of $PbTiO_3$, $Ba_xSr_{1-x}TiO_3$, and layered perovskite-relative La_2NiO_4, in which there occur peaks (reflections) that correspond to neither the film nor the substrate crystal structure, and argue that these peaks are the result of multiple diffraction from both the film and substrate. I describe a simple method to predict and identify peaks resulting from hybrid reflections.

BIOGRAPHICAL SKETCH

After growing up in Concord, Massachusetts, Eva did her undergraduate work at Scripps College, a small liberal arts college roughly 40 miles east of Los Angeles. In 2009 Eva received B.A.'s in mathematics and in chemistry. When she is not in the lab, Eva enjoys gardening, bird-watching, and riding her bicycle. In July, 2017 Eva and her family will move to Boise, ID where she will join Intel as an Integration Technologist.

Prediction is very difficult, especially about the future. – attributed to Niels Bohr.

Well, there are some questions for which the answer may be "it just is so", but equally there are other questions whose answers lead into deeper physical insights. – Martin T. Dove, "Theory of displacive phase transitions in minerals," 1997.

This dissertation is dedicated to my friends, especially my best friends: my parents, my grandmother, and my husband. Though it didn't always appear this way, getting my PhD has made me very happy and I'm grateful for all ways in which you helped me.

ACKNOWLEDGEMENTS

Thank you to Richard and Bruce for teaching me from scratch about computational materials science and vacuum deposition techniques, for giving me the freedom to explore the ideas that I thought were exciting, and for lighting a fire in my belly to be part of a continuous loop of materials design, synthesis, characterization, and improved design again.

Thank you to Craig and Nicole for everything you taught me.

Thank you to Frank DiSalvo for being my advocate from the very beginning through the very end, and thank you to Frank Wise, Lara Estroff, and everyone in the AEP department, MSE department, and graduate school who stepped in to give me additional support when the task of supporting me grew very big.

Thank you to everyone in the Schlom group for your incredible patience, generosity with your time, and for welcoming me into your group. It's been a blast!

Thank you to Dieter for friendship, support, and advice, and for doling out commiseration and kicks in the pants in equal measure and each just when needed.

I owe the greatest debt of gratitude to Darrell, without whom I surely could not have completed my PhD. Thank you, Darrell, for giving me the chance to prove myself, for showing me what great leadership looks like, and for everything you have taught me, especially about hard work and patience. Seeing what can grow from the rich soil of the freedom to follow ideas wherever they go, an unwavering foundation of support, and honesty with one's results has been an inspiration that I will not forget.

I would like to acknowledge my funding sources: the National Science Foundation and the Department of Energy. Specific grants are mentioned in the Acknowledgement sections of this dissertation's body chapters. I would like to give special thanks to the National Science Foundation Graduate Research Fellowship, which I had from 2010-2013.

Last but not least, I would like to help everyone who helped me through eight long years. To everyone who made me laugh, thank you. And now, time's up; let's do this!

TABLE OF CONTENTS

LIST OF FIGURES

LIST OF TABLES

CHAPTER 1

INTRODUCTORY MATERIAL

1.1 Introduction

This thesis is on three topics united by a common current: the unusual properties of lead, the eighty-second element on the Periodic Table. In Chapter 2, I discuss how the chemistry of lead in the 2+ oxidation state interacts with the chemistry of the other ions in the compound $CsPbF_3$ to drive its ground state structure. In Chapter 3, I discuss how the kinetics of lead oxidation and the thermodynamics of PbO adsorption/desorption control the conditions under which $PbTiO_3$ may be grown by molecular-beam epitaxy. In Chapter 4, I describe and document instances of multiple x-ray diffraction events in oxide films, motivated by results from strongly-scattering $PbTiO_3$ thin films.

While the unusual chemistry and physics of lead make it an excellent example for study, the principles found in this dissertation may be equally applied to systems that do not contain lead. For example, one of the most interesting properties of $CsPbF_3$, its ferroelectricity, is found in lead-free materials such as $BaTiO_3$ and $KNbO_3$. $CsPbF_3$ is a handy example system because of the coexistence between ferroelectricity and another, more-common but generally less-technologically-useful structural distortion. The growth mechanism of $PbTiO_3$ by MBE is analogous to that of many other materials, such as $BiFeO_3$, $SrRuO_3$, and $SrIrO_3$; the difficulty in oxidizing lead relative to most other metallic elements allows facile study of the role of oxidation kinetics in isolation from other factors. Lastly, the strong scattering of the lead atom allows the signature of multiple diffraction events to be easily observed in x-ray patterns, but the findings of double-diffraction from lead-containing films and their substrates applies similarly to systems that scatter x-rays more weakly. Thus, while this dissertation focuses upon lead-containing materials, I hope

that the results will be of broad interest.

In the introduction to this dissertation I include two quotations, the spirit of which I hope is captured in this dissertation: first, that answering "why" has value in itself. The Chapters of my dissertation address:

Why does $CsPbF_3$ form in the structure that it does?

Why is a very large excess of lead relative to the titanium flux required to grow stoichiometric, phase-pure $PbTiO_3$ by molecular-beam epitaxy?

Why does the x-ray diffraction pattern of epitaxial thin films of $PbTiO_3$ grown on $SrTiO_3$ show diffraction peaks not corresponding to either $PbTiO_3$ or $SrTiO_3$?

There intrinsic value in answering these "why" questions. In addition, however, I hope that answering these "why" questions may help us to make predictions (even about the future!), and about systems besides $CsPbF_3$ and $PbTiO_3$. A few of the great "how" questions of materials science and materials scientists are:

How does a collection of atoms decide what structure to take in the solid state?

How can I facilitate the growth of the crystal phases and structures that I want?

How do I confirm that my interpretation of an x-ray diffraction pattern is correct?

The chapters of my dissertation, I hope, may be small contributions to answer these questions.

1.2 Relevant crystal chemistry

All materials considered in this dissertation are crystalline solids. Perovskites are considered in all chapters; Ruddlesden-Poppers are also described in Chapter 4.

1.2.1 Crystal structures

The perovskite structure in its highest-symmetry form may be described as a cube with anions X on the face centers, cations A on the corners, and cations B in the cube body-centers. This structure is shown in Figure 1.1(a)-(c) and has space group $Pm\bar{3}m$. By geometry the A cation occupies a larger site than the B cation. Approximating the ions as hard spheres with radii r, crystal packing within the cubic perovskite structure is optimal when the tolerance factor [72],

$$tol = \frac{r_A + r_X}{\sqrt{2}(r_B + r_X)}, \tag{1.1}$$

is equal to unity. The perovskite structure is very versatile, accommodating nearly every element of the periodic table in one of the three crystallographic sites [174]. In order to do so the structure undergoes a number of symmetry-lowering distortions, described in Section 1.2.2.

Oxygen is a common anion in ABX_3 perovskites. While oxygen is more electronegative than the elements on the A and B sites, the large formal charges on the cations, and the B cation especially, allow them to compete with O^{2-} in electrophilicity. Thus, the bonds in oxide perovskites, especially the B-O bonds, have mixed ionic and covalent character [161]. Fluorine is more electronegative than oxygen and so A-F or B-F bonds in fluoroperovskites are considered to be more ionic and less covalent than in oxide perovskites [68].

The Ruddlesden-Popper structure, shown in Figure 1.1(d)-(f), is a structural relative

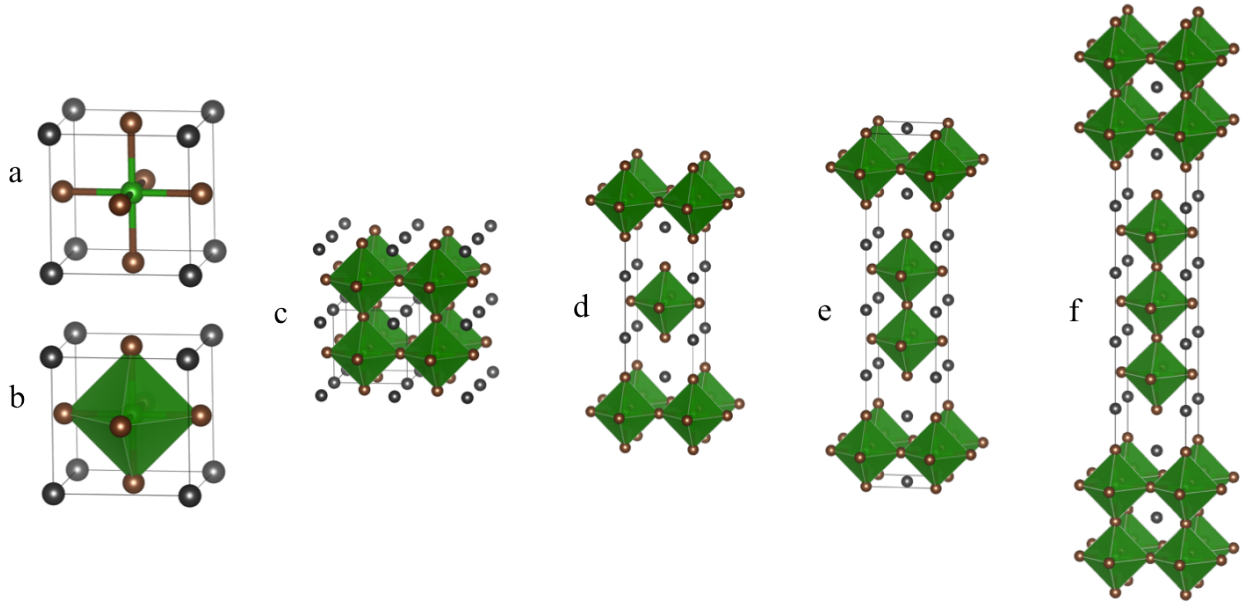

Figure 1.1: Unit cell of the perovskite in its high-symmetry state, space group $Pm\bar{3}m$ (a-c) and Ruddlesden Poppers with (d) n=1; (e) n=2; and (f) n=3, all in the high-symmetry space group $I4/mmm$. Body-centered unit cells are shown for the Ruddlesden Poppers, though this is not the primitive unit cell. In this figure black spheres represent the A-site cations, green spheres represent the B-site cations, and brown spheres represent the anions. Green octahedra envelop the octahedral B-site coordination polyhedra.

of the perovskite. It is traditionally described as an integral number n of two-dimensional ABX_3 perovskite sheets interspaced with a layer of AX rocksalt, giving a stoichiometry $A_{n+1}BX_{3n+1}$. In nature n is generally 1, 2, or 3 [59, 169, 170], though higher numbers of n are possible and in oxides have been synthesized in thin-film form [77, 197, 198].

1.2.2 Phase transitions in perovskites

When the tolerance factor given in Eq. (1.1) differs from unity, the perovskite structure may undergo symmetry-lowering structural distortions from the cubic structure. The high-symmetry structure is known in crystallographic terms as the *aristotype*, and the lower-symmetry, distorted stuctures are known as *hettotypes*. Among perovskites at most half a dozen compounds occur in the high-symmetry structure at room temperature [96],

so study of these symmetry-lowering distortions is very important to understanding the functional properties of perovskites.

When the tolerance factor is less than unity and the *A* cation are undersized relative its site in the aristotypic structure, the BX_6 octahedra may rigidly rotate while maintaining corner connectivity, decreasing the volume of the *A* cation coordination polyhedron and the *A* cation coordination number [195, 215] while leaving the *B* cation environment relatively unchanged. Because octahedra in perovskites share corners (anions) with neighboring octahedra, there are some restrictions on how neighboring octahedra can rotate. Glazer notation [71] is used to describe octahedral rotation patterns, describing the sense of rotation about each of the three Cartesian axis. For example, $a^+b^0b^0$ describes rotation in the "in-phase" sense about the *x* axis, and no rotation about *y* or *z*, while $a^0b^-b^-$ describes no rotation about *x* and "out-of-phase" rotation about the *y* and *z* axes. By convention, the first unique magnitude is labelled a, the second b, and the third c. For example, $a^+b^0b^0$, $a^0b^+a^0$, and $a^0a^0b^+$ all correspond to symmetry-equivalent structures in which rotation has occurred in an in-phase sense about the *x*-, *y*-, or *z*-axis, and no rotation about the other axes, respectively. A few common Glazer tilt patterns are shown in Figure 1.2, as well as the space groups of structures with these patterns and the irreducible representation (symmetry) of the distortions relating the aristotype and hettotypes. Distortion modes are described more below.

When the tolerance factor is greater than unity, or when a lone pair-active cation (see Section 1.2.3) is present, a ferroelectric distortion might instead occur of octahedral rotations. Ferroelectricity was historically considered to involve displacement of the *B* cation against a mostly rigid anion cage [122]. A breakthrough discovery was that in most perovskite ferroelectrics, this distortion is stabilized by strong orbital rehybridization (increase in bond strength) between the *B* cation and the anions that it approaches [44, 45, 220]. Similar rehybridization is also seen between stereoactive lone pair cations

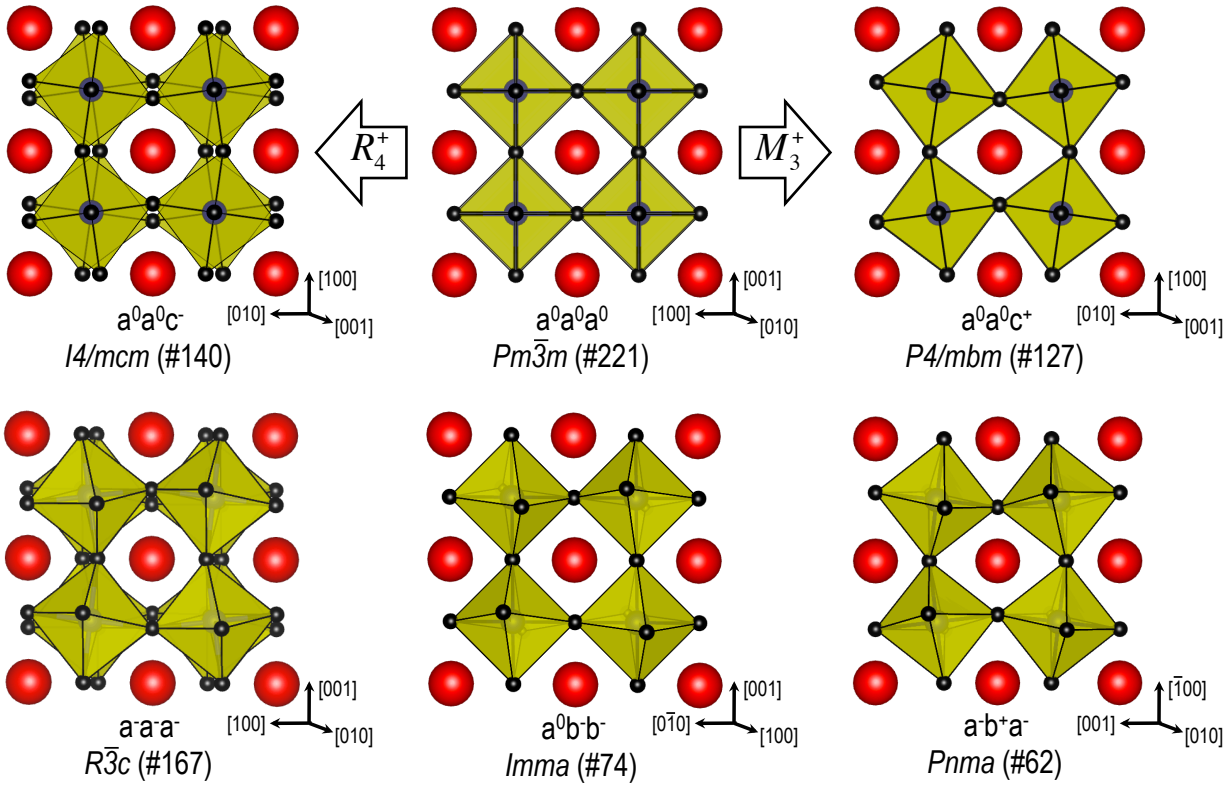

Figure 1.2: Illustration of in-phase (corresponding to a phonon mode of irreducible representation M_3^+, top right) and out-of-phase (corresponding to a phonon mode of irreducible representation R_4^+, top left) octahedral rotations about the [001] axis acting on the $Pm\bar{3}m$ aristotype (top center), as well as illustration of how rotations about multiple axes modify the structure (bottom row). Magnitudes a, b, and c are chosen arbitrarily for structures shown. Axes are with respect to the pseudocubic cell. *A*-site cations are shown as red spheres, and *B*-site cations sit in the centers of the yellow anion octahedra. From Smith et al, 2015 [183], which is reproduced in Chapter 2.

that drive ferroelectric distortions [44, 45, 207, 208]. The shift in electron density associated with this orbital rehybridization increases the polarization that results from such distortions [220].

Octahedral rotations and ferroelectricity rarely coexist in the ground state structure due to the fact that the most common octahedral rotation pattern lowers the structural symmetry such than antipolar rather than polar displacement patterns are favored, and always occur to some degree [21]. The octahedral rotation pattern $a^-a^-a^-$, however, is observed to coexist at equilibrium with ferroelectricity, as in mulitferroic $BiFeO_3$ and, as

we will discuss in Chapter 2, $CsPbF_3$ [23]. By studying $CsPbF_3$ we will see that different structural distortions – ferroelectricity driven by the *B*-site lone-pair cation Pb^{2+} and octahedral rotations driven by the *A*-site cation Cs^+ – both modify the anion sublattice and "compromise" with each others' chemical requirements in the ground state structure.

In Chapter 2 I study rotations and ferroelectric displacements in perovskites within the paradigm of soft-mode displacive phase transition theory [54]. Within soft-mode theory, symmetry-lowering phase transitions such as octahedral rotations and ferroelectricity in perovskites occur when a low-frequency phonon mode of the high-symmetry structure decreases in frequency (softens) until its frequency approaches zero. With null restoring force acting on this displacement pattern, the mode "freezes in," distorting the structure. The close relationship between a (hard) phonon mode that is present in a high-symmetry structure above a phase transition, and the structural distortion that characterizes the low-symmetry structure below the phase transition temperature, allows one to computationally predict the low-temperature ground-state structure of a perovskite by considering the phonon modes of the high-symmetry, $Pm\bar{3}m$ structure, as will be described in Section 1.3. Mode crystallography [157] complements the soft mode theory of phase transitions by relating a lower-symmetry ground-state structure to the high-symmetry aristotype through the magnitude and irreducible representation (symmetry) of various orthonormal distortion modes.

Several of the compounds studied in Chapters 3 and 4 are ferroelectrics below what is know as their Curie temperature, and paraelectric above it. These compounds are $PbTiO_3$, $BiFeO_3$, and $Ba_{0.2}Sr_{0.8}TiO_3$, with Curie temperatures of 490°C [180], roughly 820°C [163], and -153°C [22] in the bulk, respectively. All of these compounds were grown as strained films; as strain has a strong, positive influence on Curie temperature [42, 76, 181, 182], the Curie temperatures of these films are likely to be higher than these bulk values [206]. Note that both tensile and compressive strain tends to increase the overall Curie temperature of

the film, with tensile strain stabilizing to higher temperatures in-plane polarization and compressive strain stabilizing to higher temperatures out-of-plane polarization. The only film whose Curie temperature we measured, a $Ba_{0.2}Sr_{0.8}TiO_3/SrTiO_3$ (001) thin film, had a Curie temperature of -103°C, [185] as predicted using Landau-Devonshire theory based on its nominal strain and stoichiometry [181, 182].

1.2.3 Lone pair chemistry

One special case of covalent bonding deserves specific mention. In heavy main group elements the energetic separation between the s and p valence states is too great for s-p hybridization to occur. s-p hybridization is very common in compounds with second row main-group elements like carbon and oxygen, and is responsible for the tetrahedral bond geometry characteristic of organic molecules and diamond, as well as the bent shape of a water molecule. Rather, in the heavier $3p$, $4p$, and $5p$ main group elements, the s and p orbitals are separated by up to a few eV and thus are oxidized or form bonds separately from each other. In some main group cations such as Tl, Sn, Pb, Bi, and Sb, an $ns^2\ np^0$ valence, *e.g.* $6s^2\ 6p^0$ in Pb^{2+} or $5s^2\ 5p^0$ in Sb^{3+} [214], is common.

The s^2 electrons are referred to as a lone pair, and, while they have traditionally been referred to as an "inert" pair [214], recent work has shown that they are in fact a product of covalent bonding and thus not chemically inert [208]. When a cation with the s^2 electron configuration bonds to a closed-shell anion – *e.g.* F^-, O^{2-} – both the resulting bonding σ and antibonding σ^* orbitals will be filled, as shown in the molecular-orbital diagram in Fig. 1.3. Such a configuration is energetically unfavorable.

Based on the cation-anion bond strength and the energetic proximity of the cationic s and p orbitals, the formally-empty cationic p orbital may be able to hybridize with and thereby stabilize the σ^* orbital. The orbital that is observed as a result of this three-atomic-

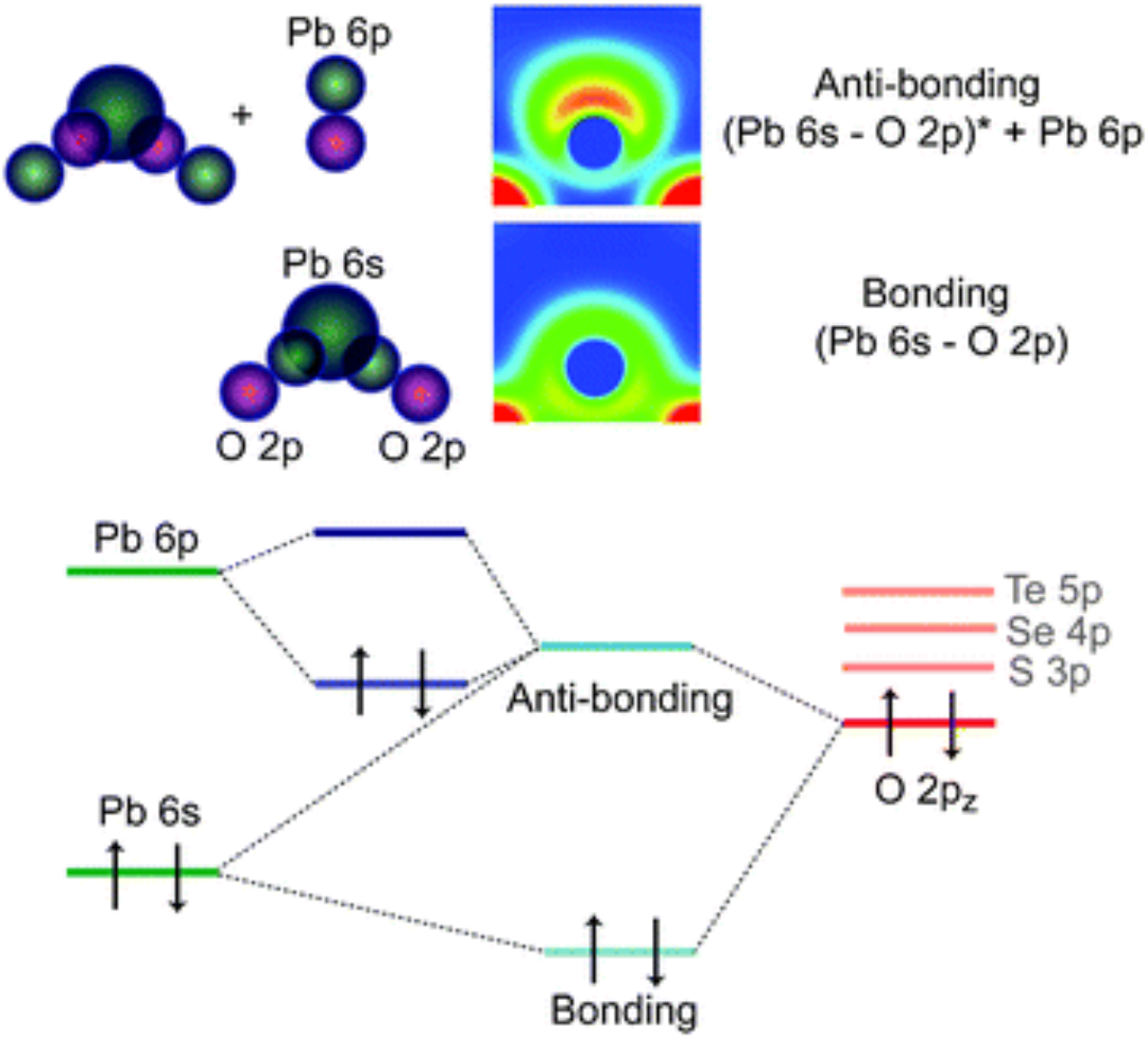

Figure 1.3: (Top left) Pictorial representation of the bonding *vs.* antibonding Pb *s*-O *p* interactions and how the antibonding Pb-O σ^* orbital overlaps in space with the formally-empty Pb *p*. (Top right) Calculated real-space electronic density of the Pb *s*-O *p* σ and Pb *s*-O *p* σ^*-Pb *p* orbitals in litharge PbO. (Bottom) Molecular-orbital diagram of the interaction, with the energies of other calcogenide *p* orbitals shown in addition to those of oxygen. Reproduced from Walsh et al [208].

orbital interaction is what is commonly referred to as a "stereoactive" lone pair, though note that the term "stereoactive" does not have exactly the same meaning as when used in organic chemistry. The electronic density of such a stereoactive lone pair orbital is strongly asymmetric about the cation nucleus.

Such hybridization is only allowed by symmetry if inversion symmetry is broken about the lone-pair cation. Lone pair chemistry may stabilize either ferroelectric ground states, such as in $PbTiO_3$ and $BiFeO_3$, or antiferroelectric ground states, such as in $PbZrO_3$. The crystallographic cite at which a stereoactive lone pair cation sites is forbidden by symmetry from being a center of inversion, but there may be a center of inversion elsewhere in the crystallographic unit cell.

Breaking inversion symmetry carries a steric energetic cost [161]. For it to be energetically favorable for the lone pair to localize and inversion center to be broken, the stabilization of the σ^* orbital must be greater than this cost. In cases when the energetic and spatial overlap between then empty p orbital and the σ^* orbital is poor, it may be more energetically favorable to retain centrosymmetry. The conditions under which it will or will not be favorable for a lone pair to localize are discussed at length in Chapter 2.

1.3 First-principles calculations

While most applications of material science require the existence of a physical material, using a computer to study the properties of hypothetical materials can still give valuable insight on real materials. Computational modeling allows a user to have full control of her system, placing atoms where-ever she would like and eliminating confusing effects from defects or impurities. Computational modeling may also be used to make systems that are difficult or impossible to synthesize, such as unstable or metastable structures. In

Chapter 2 I will study why $CsPbF_3$ forms the structure that is observed experimentally by comparing the properties of this measured ground state structure to the properties of various never-observed but closely-related structures. I use density functional theory, which has its foundation in quantum mechanics, as my physical approach, due to its ability to predict materials properties from a minimum number of adjustable user inputs.

1.3.1 Hamiltonian of a system with many electrons and nuclei

This section is after Chapter 1 of Engel and Dreizler [57].

Within quantum mechanics, the Hamiltonian of a system with multiple nuclei and electrons in the absence of an external field is given by a Hamiltonian $\hat{H}$:

$$\hat{H} = \hat{T}_{\mathrm{n}} + \hat{T}_e + \hat{V}_{\mathrm{n-n}} + \hat{V}_{\mathrm{n-e}} + \hat{V}_{\mathrm{e-e}} \tag{1.2}$$

for $\hat{T}$ the kinetic energy and $\hat{V}$ the potential energy of the nuclei (n), electrons (e), and interactions among them.

The nuclear kinetic energy operator $\hat{T}_n$ is the sum of contributions over all K of the nuclei:

$$\hat{T}_{\mathrm{n}} = \sum_{\alpha=1}^{K} \frac{(-i\hbar\nabla\vec{R}_\alpha)^2}{2M_\alpha} \tag{1.3}$$

with nucleus α having mass M_α and position $\vec{R}_\alpha$. The electron kinetic energy $\hat{T}_{\mathrm{e}}$ is quite similar.

The nuclear-nuclear Coulombic potential energy term $\hat{V}_{\mathrm{n-n}}$ is given by

$$\hat{V}_{\mathrm{n-n}} = \sum_{\alpha,\beta=1;\alpha<\beta}^{K} \frac{Z_\alpha Z_\beta e^2}{|\vec{R}_\alpha - \vec{R}_\beta|} \tag{1.4}$$

for the K nuclei. $\hat{V}_{\mathrm{e-e}}$ is similar but with Z_α=Z_β=1 and the sum over the N electrons; $\hat{V}_{\mathrm{n-e}}$ is also similar but negative (attractive rather than repulsive), and no stipulation that the

counting index for the nuclei α have any relationship (including being different from) the electron counting index β.

The wave function Ψ describes the position $\vec{R}$ of each of the K nuclei, the position $\vec{r}$ of each of the N electrons, and the spin $\vec{\sigma}$ of each of the N electrons. The Schrödinger Equation relates Ψ and the Hamiltonian as

$$\hat{H}\Psi(\vec{R}_1, ...\vec{R}_K; \vec{r}_1\vec{\sigma}_1, ...\vec{r}_N\vec{\sigma}_N) = E\Psi(\vec{R}_1, ...\vec{R}_K; \vec{r}_1\vec{\sigma}_1, ...\vec{r}_N\vec{\sigma}_N). \tag{1.5}$$

To solve this equation, the Born-Oppenheimer approximation is traditionally used. Within this approximation, the wavefunction Ψ_a may be split into separate wavefunctions for the electrons and for the nuclei, such that

$$\Psi = \Psi^m\Psi^e. \tag{1.6}$$

The electron wavefunction will depend on the position of the nuclei $\vec{R}_\alpha$, but the electrons will be approximated as responding very quickly to changes in nuclear position, much more quickly than the nuclei themselves move.

Even within the Born-Oppenheimer approximation, solving this equations is computationally very expensive (in terms of both processing and memory): for each electron there are four variables (three spatial and one spin) [106]. Systems of interest to materials scientists will have hundreds of electrons; for example, just a single unit cell of $PbTiO_3$ has 128 electrons. The approach that I have used in this thesis to solve the many-electron wavefunction is density functional theory, described in the next section.

1.3.2 Density-functional theory

The Hohenberg-Kohn Theorem [87] simplifies the problem of a many-electron wavefunction (with N^3 variables, excluding spin) to a problem of electron density in space (with

3 variables only, excluding spin) [57]. The electron density is simply the sum over all electrons of the probability density for each electron at a particular point in space. Essentially, the Hohenberg-Kohn Theorem proves that there are unique, one-to-one mappings among: external potentials that are unique to within a constant; ground-state wave functions; and ground state electron densities. In other words, one can express a ground state of a system within a particular external potential with no loss of information as either a many-particle wavefunction or as an electron density. Within density functional theory (DFT), the energy of a system is expressed as a function of the electron density; because the electron density itself is a function (of position in space), the energy is thus a "functional" (function of a function) and written $E[\rho]$ or $E[\rho(\vec{r})]$ for $\rho = \rho(\vec{r})$ the density function.

The functional F that would act on ρ to give the energy E is similar in form to Equation 1.2 for the electronic contribution [106]:

$$F[\rho(\vec{r})] = T[\rho(\vec{r})] + V[\rho(\vec{r})] + E_{ncl}[\rho(\vec{r})] \tag{1.7}$$

for $T[\rho(\vec{r})]$ the kinetic energy, $V[\rho(\vec{r})]$ the classical Coulomb interaction, and $E_{ncl}[\rho(\vec{r})]$ the so-called non-classical portion of the functional; this portion includes self-interaction, the antisymmetry of the electrons (which are fermions), and correlation between electronic motion.

$V[\rho(\vec{r})]$ is easy to calculate but $T[\rho(\vec{r})]$ and $E_{ncl}[\rho(\vec{r})]$ are not. Within the Kohn-Sham density functional theories [70, 106, 107], $T[\rho(\vec{r})]$ is approximated by calculating the kinetic energy of a system of non-interacting electrons whose summed orbital densities equals the density of the real system [81]. The contribution to the kinetic energy from the electron correlations is included in with $E_{ncl}[\rho(\vec{r})]$ to make what is known as the exchange-correlation functional $E_{XC}[\rho(\vec{r})]$. Various methods to approximate $E_{XC}[\rho(\vec{r})]$ are given in the next section.

1.3.3 Practical approximations

A number of approximations are necessary for the practical and accurate calculation the electronic wavefunctions with DFT. By practical, I mean: sufficiently economical with computational time and memory such that the wavefunctions of systems large enough to be interesting can be calculated with real computers in a reasonable amount of time and at a reasonable financial cost.

Only the electrons in the outer few shells of an atom participate in bonding; the inner-shell electrons do not participate in bonding. However, the inner-shell electrons do occupy (and thus exclude the valence electrons from) lower energy orbitals. The higher energy orbitals occupied by the valence electrons have many nodes; their electronic density varies rapidly with position, especially near the nucleus, requiring larger planewave basis sets to accurately describe them [158]. About the atomic nucleus the Coulomb potential diverges; however, the potential of the nucleus is largely shielded by the core electrons. Essentially, inclusion of all electrons and the full nuclear Coulomb potential greatly complicates calculations without having a significant effect on the chemistry or physics of the atom. Thus it is common to approximate the nucleus plus core electrons with a so-called pseudopotential, which also has the effect of smoothing the valence wave functions [158]. Schematics of the radial dependence of the real and pseudopotential and real and pseudo-orbitals is shown in Figure 1.4.

A drawback of using pseudopotentials is that there is no one unambiguously-defined best pseudopotential for a given atom; different pseudopotentials are used for different applications, with the choice being driven by the application and computational requirements. Furthermore, generation of pseudopotentials is "a tricky, cumbersome, error-prone and time-consuming task" [114]. For these reasons, a given set of pseudopotentials will commonly be shared by many researchers. In this way the strengths and weaknesses

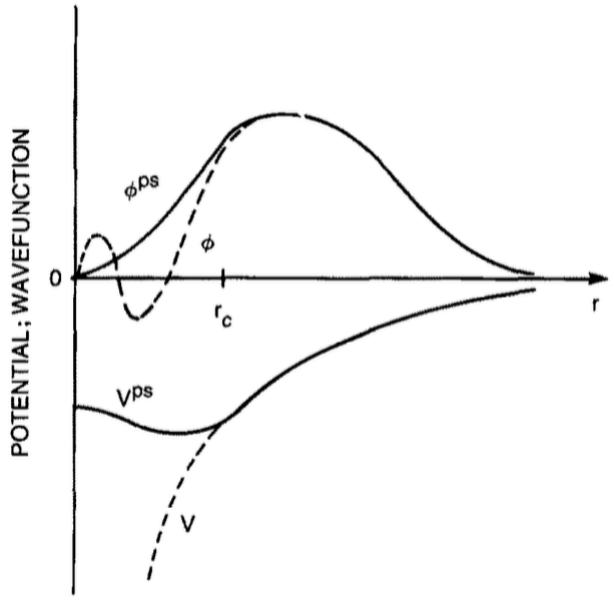

Figure 1.4: The all-electron potential V and orbital ϕ are altered to the pseudopotential V^{ps} and pseudo-orbital ϕ^{ps} inside the core radius r_c. From Pickett [158], Figure 1.

become well documented and either corrected, avoided, or simply acknowledged.

Approximation of the exchange-correlation functional is also done in various ways, depending on the property of interest of the calculation as well as restrictions to computer power. The local-density approximation (LDA) bases the exchange-correlation energy on that of a homogeneous electron gas (HEG). The exchange-correlation energy of a real system is approximated as being locally the same as that of a HEG of the same density [57]. The LDA has the advantages of not having any free parameters and of relative simplicity and computational inexpensiveness [57, 105]. The generalized-gradient approximation (GGA) also includes contributions from the gradient of the electronic density. There are many varieties of GGA, optimized for various purposes; PBEsol is optimized for solids [156] was used in Chapter 2 of this dissertation.

1.3.4 Applications of DFT

Density functional theory was implemented in this dissertation by the Vienna Ab-initio Simulation Package (VASP) [111, 112]. Many, many different kinds of calculations may be done with VASP or other DFT software. The following are a list of the different types of calculations I did.

Electronic structure calculation Input a set of nuclear coordinates, pseudopotentials, basis set for the wavefunction, and a grid of points in reciprocal space. VASP calculates the ground state electronic wave function. The ability of VASP to accurately approximate the true ground state wavefunction depends on supplying a large enough basis set and a sufficiently dense grid of points of reciprocal space.

Structure relaxation Find the electronic structure for a particular set of atomic coordinates. Calculate forces (change in energy with respect to position) on each atom. Move each atom in the direction of steepest descent. Repeat electronic structure calculation, force calculation, and structure modification steps until energy (or forces) are minimized.

Phonon calculation Find the electronic structure for a particular set of atomic coordinates. Calculate the force constant matrix for every pair of atoms and each Cartesian direction. The dynamical matrix is related to the force constant matrix through the masses of the atom pairs. The phonon frequencies are eigenvalues of the dynamical matrix.

Structure prediction among hettotypes of a particular aristotype Find the force constant matrix and the dynamical matrix of the relaxed aristotype structure. Find the eigenvectors of the force constant matrix. Create test structures, one for each unstable (imaginary frequency) phonon mode; into each test structure freeze in one of the force constant matrix eigenvectors, or, in the case of eigenvectors corresponding to degenerate modes, eigenvectors along different directions to give structures in different space groups. Relax

each child structure and repeat the process until all child structures are dynamically stable (have no unstable phonon modes). The child structure with the lowest energy is the ground state structure, at least within the manifold of that aristotype.

1.4 Thin film growth by molecular-beam epitaxy

Molecular-beam epitaxy (MBE) is the Cadillac – or, if one prefers, the Tesla – of thin-film growth techniques for high crystal quality [149]. Films grown by MBE may be characterized by atomically-sharp interfaces [28, 161] and a high degree of control over beam flux and growth conditions [86], film crystal structural [77, 78, 136], and film oxidation state [136, 176, 192, 204]. The films in this dissertation were grown by MBE.

1.4.1 Hardware: chamber, *in situ* characterization, and ozone

Molecular-beam epitaxial growth is done by evaporation or sublimation of atoms from elemental sources onto a heated substrate in a vacuum chamber. In reactive MBE, a reactive gas such as oxygen or ozone is also introduced to produce, in this example, an oxide. All MBE described hereafter in this dissertation is reactive oxide MBE.

The background pressure of the MBE (pressure without oxygen or ozone introduced) is generally in the ultra-high vacuum range, *i.e.* $< 1 \times 10^{-9}$ Torr [86]. However, when reactive gases are introduced the pressure may reach 1×10^{-4} Torr; the fundamental upper pressure limit for MBE is determined by the greatest pressure at which the mean free path of the relevant (source) atoms is greater than the distance from source to substrate [175]. When the mean free path of the molecular beam is less than the distance to the substrate, calibration and control of flux is complicated by pressure-dependent and atomic mass-

dependent scattering of the molecular beam [175].

Besides the long mean free path of gas-phase atoms, the high vacuum environment gives another advantage: facilitation of *in-situ* analysis [28]. Reflection high-energy electron diffraction (RHEED) is such a technique; I utilized RHEED in all the thin film growths described in Chapters 3 and 4. In RHEED, a beam of electrons from an electron gun strikes a sample at a low angle (0.5°-2.5°[28]), giving surface-sensitive structural information. Because of the sensitivity to the surface in particular, RHEED may be used for real-time feedback about the growing film, for example for flux calibrations (described in the next section).

Besides through changing of the source temperatures, fluxes may be controlled through opening and closing metal shutters that physically block the molecular beam. These shutters can open or close in less than $^1/_{10}$ s. During growth by reactive oxide MBE, fluxes are generally such that an atomic layer is deposited in 30 s. Opening and closing the shutters gives rapid, cleanly punctuated, and reproducible bursts of molecules.

Ozone – O_3 – is much more reactive than dioxygen (O_2) and thus an appealing oxidant for MBE, especially when oxidizing species that are difficult to oxidize in O_2 at MBE-amenable pressures [24, 176]. Ozone may be generated from dioxygen by a number of methods, including electric discharge, irradiation with ultraviolet light (as occurs in the upper levels of Earth's atmosphere by sunlight), and certain chemical reactions [89]; in the Schlom group laboratory at Cornell University, ozone is generated by electric discharge.

The commercial ozone generator owned by the Schlom group at Cornell University will produce a gas mixture that is approximately 16% ozone and the rest dioxygen [133] at the default operating conditions set by the control unit [83]; the mixture introduced into the chamber is roughly 10% ozone. The concentration of ozone may be increased by exploiting the difference in vapor pressures between the two molecules at cryogenic

temperatures [89]. Caution must be taken when creating concentrated ozone due to its explosive nature; ozone may be safely collected in modest amounts by adsorption onto silica [176].

1.4.2 Shuttered growth

Within oxide MBE, films are generally grown by what is known as shutter-controlled (or shuttered) growth. Under this growth regime, multicomponent films are grown layer-by-layer by depositing doses of the constituent elements. For example, the perovskite $SrTiO_3$ (isostructural to the perovskite shown in Figure 1.1(a)-(c)) may be grown by sequential deposition of Sr and Ti. Oxidant is supplied continuously so that the resulting layers are SrO and TiO_2. This process is repeated to grow a film of desired thickness.

This growth regime gives a large amount of control to the grower, allowing her to potentially grow materials that are not thermodynamically stable or which do not exist in nature. Rather, she may grow films by kinetic control: she deposits atoms in the order that she wishes at a temperature at which there is sufficient surface diffusion to ensure good crystallographic quality, but little enough bulk diffusion to "lock in" the metastable structure of interest [161, 218]. With this power to control the structure and composition of the film, however, comes the responsibility for the grower to have extremely good knowledge (calibration) of the atomic fluxes, such that the chosen deposition time supplies the precise quantity of atoms desired. Such a quantity would be unit monolayers of Sr(O) and Ti(O_2) in the growth of $SrTiO_3$, for example. Sources are generally deposited in series. A cartoon of growth within this regime is shown in Figure 1.5(a).

Fluxes may be calibrated with great precision by monitoring the growing film surface with RHEED [78]. This calibration process is can be very time-consuming, however, and is made difficult by the fact that source fluxes may drift by 1% an hour [190], a significant

rate of change considering that a growth rate of 30s per atomic layer (25 nm per hour) is typical for oxide MBE, and films may be grown to be 300 nm or more, a growth time of 12 hours at those rates. One approach that avoids some of the challenges of shuttered growth is to grow within an adsorption-controlled growth regime, described in the next section.

1.4.3 Adsorption-controlled growth

Within an adsorption-controlled growth regime, temperature and pressure conditions are chosen such that the desired phase will be formed on the growing film surface and any secondary phases will either not form or will not stick to the surface. The range of temperatures and pressures in which this occurs is known as the adsoprtion-controlled growth window. This conditions of this window has been predicted from thermodynamics for a number of compounds, such as $PbTiO_3$ [53, 192], $BiFeO_3$ [93], $LuFe_2O_4$ [31], and $SrTiO_3$ (thought it was not grown under these conditions) [97]; the growth window may also be found empirically. In practice there will also be a finite window in source flux, allowing a grower to spend much less time with flux calibrations than would be necessary to grow a film of comparable quality by shutter-control. Sources are generally codeposited (deposited in parallel) as this reduces growth time. A cartoon of growth within this regime is shown in Figure 1.5(b).

For a multicomponent oxide that may be grown by adsorption-control, in the vicinity of the growth window generally one element will display near-unity sticking and one component will have sticking that depends strongly on oxidation state and/or surface composition. For example, in the growth of $PbTiO_3$, Ti^0 readily oxidizes to Ti^{IV} and then exhibits unity sticking as TiO_2 [192]. On the other hand, Pb^0 does not oxidize particularly easily to Pb^{II}; and Pb^{II} in the form of PbO has a highly-variable volatility, such that

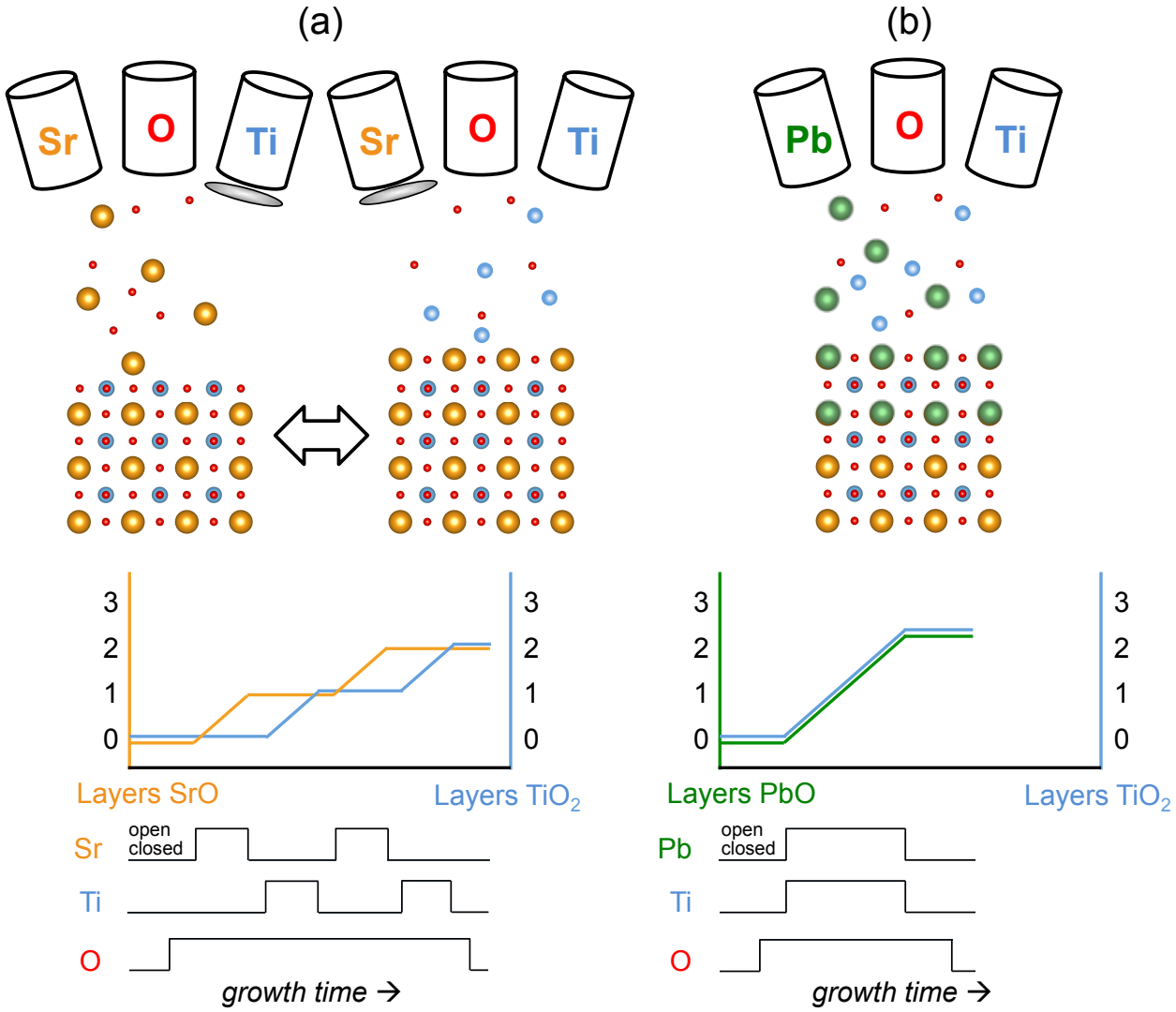

Figure 1.5: Schematics of two growth regimes. On top is a cartoon of the elemental sources either depositing atoms or being closed with a shutter. Deposited atoms form the surface of the growing film. At middle and bottom are an illustrative plots of number of metal oxide layers of various kinds deposited as a function of growth time, and open or closed status of the three shutters. (a) Schematic of shutter-controlled growth of homoepitaxial $SrTiO_3$. Layers of Sr(O) and Ti(O_2) are deposited in series. A typical growth temperature is 800°C. (b) Schematic of adsorption-controlled growth of heteroepitaxial $PbTiO_3$ on a $SrTiO_3$ substrate. Lead, titanium, and oxidant are continuously codeposited. A typical growth temperature for adsorption-controlled growth of $PbTiO_3$ is 600°C; adsorption-controlled growth is highly sensitive to substrate temperature and chamber pressure.

within the adsorption-controlled growth window, a molecule of PbO will only stick to the growing film surface if that surface is terminated with TiO_2 [192]. Pb^0 has an extremely-high volatility near the growth window of $PbTiO_3$, and lead metal is not expected as an impurity in films grown close to the growth window.

The thermodynamic picture of adsorption-controlled growth does not, by its nature, consider the growth rate (kinetics). Thermodynamics describes the relative energies of different chemicals and says nothing about the reaction path that might connect them. In Chapter 3 I discuss the importance of oxidation kinetics to the growth of $PbTiO_3$ and $BiFeO_3$ by adsorption control.

1.5 X-ray diffraction

Typical crystal structures have periodicity on the order of a few Å and x-rays are electromagnetic radiation with wavelength on the order of a few Å; thus, crystal structures may diffract x-rays under suitable geometric conditions. The diffracted pattern (geometric conditions under which the diffraction conditions are met) for a particular crystal structure and x-ray wavelength is distinctive to that crystal structure. For these reasons, x-ray diffraction is an indispensable tool for both qualitative and quantitative analysis of condensed matter, especially crystalline structures [48].

1.5.1 X-ray scattering in real and reciprocal space (non-dynamic theory)

This section approximately follows section 3-5 in Cullity and Stock, 2001 [48].

The conditions for constructive interference, *e.g.* x-ray diffraction, are as follows.

First, consider reflection of an x-ray beam from two separate real space lattice points O and A, schematically depicted in Figure 1.6(a). The incident vector $\vec{S_0}$ is reflected to vector $\vec{S}$; the angle between the incident and diffracted beams is defined as 2θ. There will be constructive interference between the reflected beams $\vec{S}$ reflected from O and from A when the path difference for those reflected beams is an integer multiple of the x-ray wavelength λ. For the vector connecting O and A, $\overline{OA}$, this path length difference δ is given by

$$\delta = -\overline{OA} \cdot (\vec{S_0} - \vec{S}). \tag{1.8}$$

Because O and A are lattice points, $\overline{OA}$ is some integral linear combination of lattice vectors $\vec{a_1}$, $\vec{a_2}$, and $\vec{a_3}$,

$$\overline{OA} = p\vec{a_1} + q\vec{a_2} + r\vec{a_3}, \tag{1.9}$$

for integers p, q, and r.

We relate the diffraction condition to the reciprocal lattice in the following way. Let

$$\mathscr{S} \equiv \frac{\vec{S_0} - \vec{S}}{\lambda} = h'\vec{b_1} + k'\vec{b_2} + l'\vec{b_3}, \tag{1.10}$$

for reciprocal lattice vectors $\vec{b_1}$, $\vec{b_2}$, and $\vec{b_3}$ and h', k', l' as yet undefined numbers. The reciprocal lattice vectors $\vec{b_i}$ are defined as follows:

$$\vec{b_1} = \frac{\vec{a_2} \times \vec{a_3}}{\vec{a_1} \cdot \vec{a_2} \times \vec{a_3}}; \quad \vec{b_2} = \frac{\vec{a_3} \times \vec{a_1}}{\vec{a_1} \cdot \vec{a_2} \times \vec{a_3}}; \quad \vec{b_3} = \frac{\vec{a_1} \times \vec{a_2}}{\vec{a_1} \cdot \vec{a_2} \times \vec{a_3}}. \tag{1.11}$$

Of particular importance to this derivation is the fact that for $i \neq j$, $\vec{a_i} \cdot \vec{b_j} = 0$.

What can we say about h', k' and l'? Substituting in to Equation 1.8 the equation for $\overline{OA}$ given by Equation 1.9 and the diffraction condition that $\delta = n\lambda$ for n an integer gives

$$n\lambda = -(p\vec{a_1} + q\vec{a_2} + r\vec{a_3}) \cdot \lambda(h'\vec{b_1} + k'\vec{b_2} +' \vec{b_3}) \tag{1.12}$$

Because $\vec{a_i} \cdot \vec{b_j} = 0$ for $i \neq j$, the above may be simplified to

$$n = ph' + qk' + rl' \tag{1.13}$$

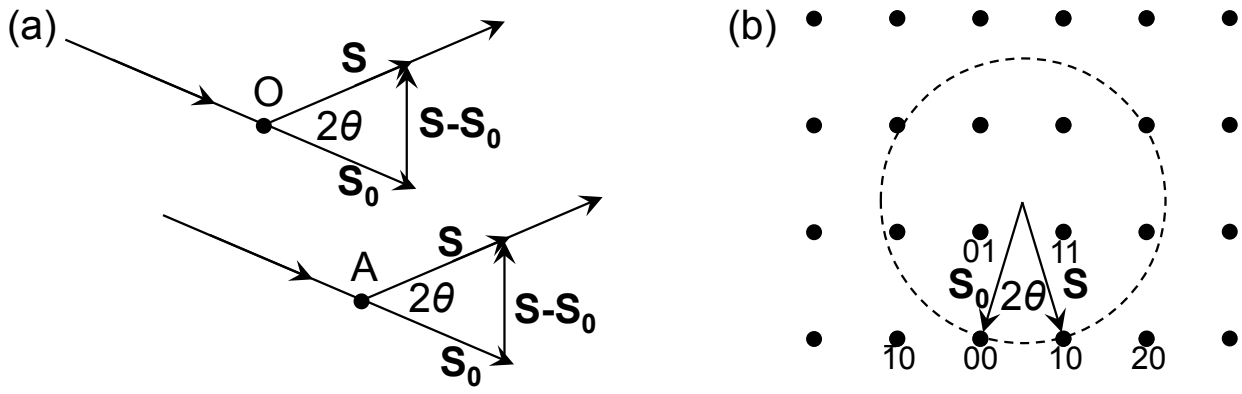

Figure 1.6: (a) Diffraction shown schematically on a real-space lattice, with reflection from two lattice points O and A. (b) Reciprocal lattice representation of 10 diffraction.

where n is still an integer (the negative sign being dropped because the negative of an integer is still an integer). Because p, q, and r are integers, for the above equality to be true in general, h', k', and l' must also be integers. By convention the primes are dropped when h, k, and l are defined to be integers, and the scattering vector $\mathscr{S} \equiv (\vec{S_0} - \vec{S})/\lambda = h\vec{b_1} + k\vec{b_2} + l\vec{b_3}$ connects two reciprocal lattice points.

The diffraction condition may be represented graphically with respect to the reciprocal lattice using the Ewald sphere, a sphere with radius $1/\lambda$ for λ the x-ray wavelength, intersecting the origin of the reciprocal lattice. This construction is shown schematically in Figure 1.6(b); for simplicity in representation on a sheet of paper, only a single plane of the reciprocal lattice is shown, and the Ewald sphere appears like a circle. The points in the reciprocal lattice besides the origin that sit on the Ewald sphere meet the diffraction condition, and may be measured when the angle between the incident and diffracted beams is 2θ. The vectors in the reciprocal lattice are physically parallel to their counterpart vectors in the real space lattice; as explained by Cullity and Stock, 2001 [48], "the direction from the Ewald sphere center to the reciprocal lattice point *hkl* on the sphere is $\vec{S}$ and defines the direction [in real space] along which the diffracted beam $\vec{S_{hkl}}$ is observed." Different reciprocal lattice points are brought in to the diffraction condition by changing the value of 2θ, the angle between $\vec{S_0}$ and $\vec{S}$. If multiple reciprocal lattice points sit on the

Ewald sphere at the same time then they may both diffract simultaneously; this idea is explored and evidence of this phenomenon presented in Chapter 4 of this dissertation.

The angles 2θ at which reflections are detected may be related to the corresponding lattice plane spacing d by Bragg's law:

$$\lambda = 2d\sin(\theta). \tag{1.14}$$

For an orthorhombic crystal, d relates to the h, k, and l and lattice parameters a=$|\vec{a_1}|$, b=$|\vec{a_2}|$, c=$|\vec{a_3}|$ as [48]:

$$\frac{1}{d^2} = \frac{h^2}{a^2} + \frac{k^2}{b^2} + \frac{l^2}{c^2}. \tag{1.15}$$

The collection of angles 2θ as well as spatial orientations of a physical (single) crystal (discussed in the next section) that meet the diffraction condition are directly related to crystalline structure. The collection of such angles forms a "fingerprint" for the particular crystal structure; the (near) uniqueness of a structure x-ray diffraction pattern is why x-ray diffraction is such an essential and quintessential tool for structural characterization. How these fingerprints are measured is discussed in the Section 1.5.3.

1.5.2 Hardware: x-ray generation, optics, and detectors

The diffraction experiments done in this dissertation were done using benchtop x-ray diffractometers. X-rays were generated with rotating anode tubes, in which a few amps of current are supplied through a hot cathode filament that is held at a few tens of kV relative to the anode target, resulting in an emission current of a few tens of mA. The anode target is water-cooled and continuously-rotated anode to prevent heat buildup [48]. X-rays are generated when the high-voltage electrons strike the target. A schematic of a sealed x-ray tube is shown in Figure 1.7(a), reproduced from Cullity and Stock [48];

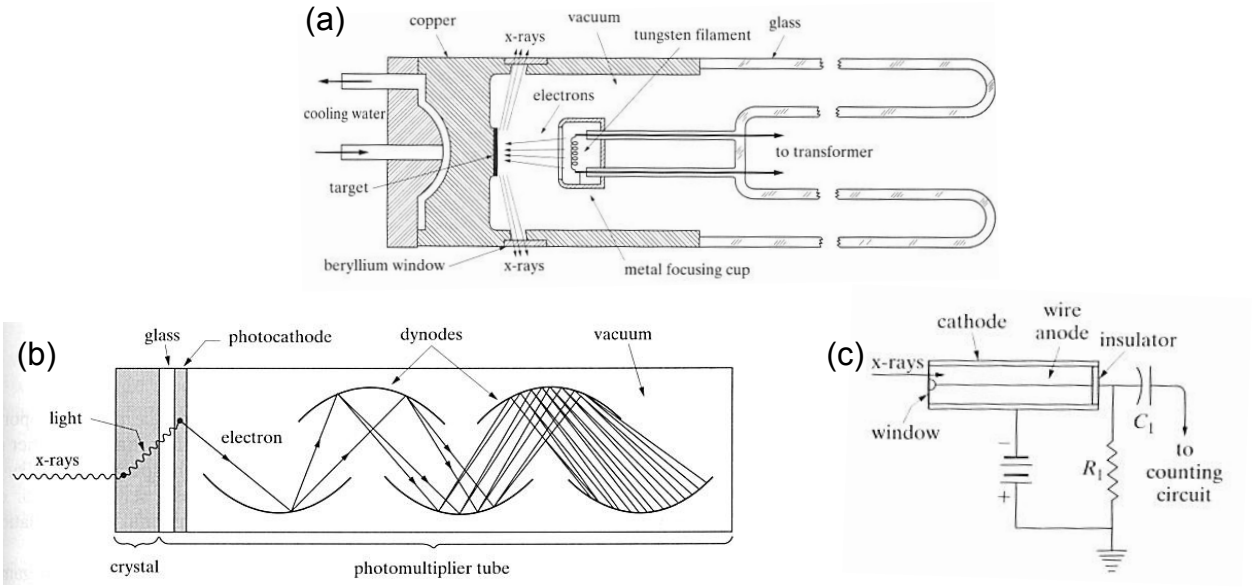

Figure 1.7: (a) Cross-section of sealed x-ray tube, reproduced from Figure 1-15 of Cullity and Stock, 2001 [48]. (b) Scintillation detector, schematic, reproduced from Figure 6-21 of Cullity and Stock, 2001 [48]. (c) Sealed proportional detector, schematic, reproduced from Figure 6-17 of Cullity and Stock, 2001 [48].

a rotating-anode tube is similar, except, of course, the anode is continuously rotated to constantly bring fresh, cooler target material into the electron beam.

The elemental composition of the target determines the wavelengths of x-rays emitted; in this dissertation copper targets were used, emitting x-rays with wavelengths between 1.392 (the $K\beta_{1,3}$ line) and 1.5406 (the Cu $K\alpha_1$ line) [88]. The x-rays were monochromated by diffracting the beam either twice or four times from germanium single crystals, to select only the Cu Kα_1 radiation.

The beam may be collimated with a soller, a collection of thin objects such as wires or foils that block the divergent portions of the beam in the diffraction plane. This serves the purpose of reducing error in 2θ measurements [67]. Slits may also be used to block divergent portions of the beam in planes perpendicular to the soller slit planes. The beam may also attenuated to reduce its intensity and not damage the detector through oversaturation.

After the beam is diffracted by the sample, it may pass again through similar pieces of optics as did the incident beam (soller, slits, attenuator, second monochromater). In the diffraction experiments reported here, x-rays are detected by either a scintillation counter in the Rigaku SmartLab [95] or a sealed proportional detector in the Panalytical X'Pert PRO [154].

In the scintillation counter, x-rays first are converted to light *via* a NaI crystal doped with a small amount of thallium. X-ray quanta excite an electron from the valence to conduction band of NaI; some of this energy is transferred to a Tl^+ ion, and that energy is released as violet light. This light ejects electrons from a photocathode, and these electrons are multiplied by dynodes until the signal from a single x-ray quantum is on the order of a volt [48]. The process of converting a single x-ray photon into a large electronic signal is shown in Figure 1.7(b), reproduced from Cullity and Stock, 2001 [48].

The sealed proportional counter, reproduced in Figure 1.7(c) from Cullity and Stock, 2001 [48], is a sealed cylinder of xenon and methane gas, with an x-ray transparent window at one end, a wire anode running the length of the cylinder, and the cathode cylinder walls at roughly 1000 V relative to the anode [48, 154]. X-rays ionize the xenon atoms; the electrons are attracted to the anode. The electric field is strong enough that these electrons can also ionize other gas atoms along the way, amplifying the signal. The anode detects the current pulse. The methane gas atoms serves as a "quenching gas" and neutralize the ionized Xe^+ [48, 154].

Neither the scintillation counter [95] nor the proportional detector have any spatial resolution, meaning that to detect different lattice spacings (changes to 2θ) or crystallites with different orientations in space, the sample and/or x-ray hardware must be moved. Definitions of angles and distances that may be changed in a typical commercial thin-film diffractometer such as a Rigaku SmartLab are shown in Figure 1.8. How those angles are scanned to measure different qualities of the sample is described in Section 1.5.3.

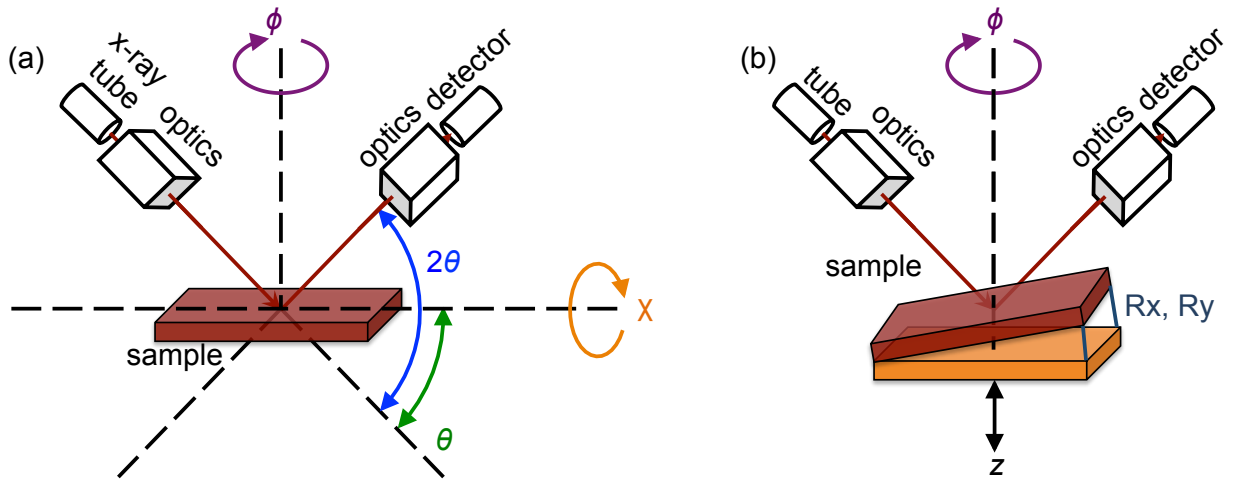

Figure 1.8: Angles controlled within thin-film x-ray diffraction. (a) χ and ϕ are controlled by rotating the sample (possibly secured to the stage with tape), while 2θ and θ are controlled by moving the tube and incident optics and/or the detector and receiving optics. (b) Rx and Ry tilt the sample (maroon) relative to the stage (orange) to effectively allow ϕ rotation to occur about an arbitrary angle relative to the sample normal. In this dissertation Rx and Ry are adjusted so that the substrate (001) is perfectly normal to the ϕ rotation axis. z adjusts the sample height so that samples of different thicknesses may be analyzed on the same diffractometer. ω is defined in Figure 1.9.

1.5.3 X-ray diffraction for structural characterization

Symmetric 2θ scans are very appealing due to their simple experimental set-up. They are used for verification of phase purity or identification of impurity phases. They have limitations, however, in particular only measuring lattice spacing of planes parallel to the sample surface [95]. Besides phase characterization with 2θ scans, x-ray diffraction can be used to gather information about epitaxy (relative orientation of two different crystal lattices in ϕ, in particular the orientation of the film lattice relative to the substrate lattice), strain, and mosaicity (spatial distribution of the scattering vectors of symmetric reflections).

A film that is mosaic will have a spatial distribution of crystallites (Figure 1.9(a)). Mosaicity is measured in x-ray diffraction through "rocking curve" scans, in which a particular value of 2θ is fixed and $\omega \equiv \theta - 2\theta/2$ is varied ("rocked") (Figure 1.9(b)). Misfit

dislocations such as those that are created during strain relaxation [128, 205] will increase mosaicity, as shown in Figure 1.9(c); comparing the full width at half-maximum intensity (FWHM) of the film rocking curve relative to that of the substrate may be used to assess whether a film has relaxed [42] and as a measure of film crystal quality [61, 121, 174]. Coexistence of *a*- and *c*-oriented domains in a ferroelectric such as $PbTiO_3$ may also be revealed in a rocking curve [61]; how *a*- and *c*-domains manifest through crystallite orientation (mosaicity) is shown in Fig. 1.9(d-e), from Ref. [35].

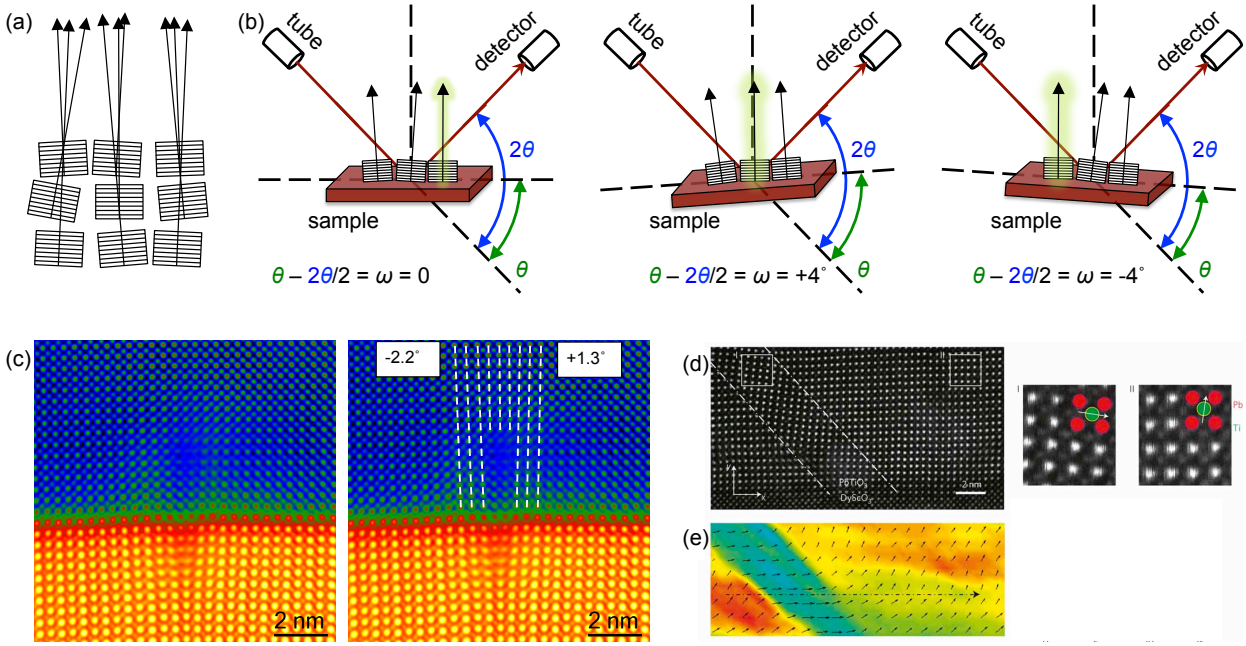

Figure 1.9: (a) Schematic illustration of mosaic crystallites. Each crystallite has the same crystal structure as the other crystallites, but their spatial orientation is different relative to the film normal. The scattering vector of a symmetric reflection is shown with an arrow for each crystallite. (b) Schematic of how mosaicity is measured by holding 2θ constant and rocking ω, to bring the scattering vectors of each crystallite into the diffraction condition (highlighted). In this figure the tube and detector are held while the sample is rocked, though in practice the sample is held fixed while the tube and detector are moved together. (c) TEM/EELS image of a $SrTiO_3$ film grown epitaxially on $DyScO_3$ (110) [pseudocubic (001)]. The misfit dislocations increase mosaicity. White lines are a guide for the eye. Angles mark atomic plane angles relative to substrate surface normal [1]. (d) TEM of a film of $PbTiO_3$ grown on $DyScO_3$ showing the different orientations of the lattice in *a* domains (outset I) and *c* domains (outset II). (e) Map of out-of-plane strain (color) and electric polarization (vectors) in the film shown in (d). Electric polarization is intimately linked with crystallite orientation in $PbTiO_3$, with polarization strongly favored along the *c* axis. (d) and (e) are from Catalan et al, 2011 [35].

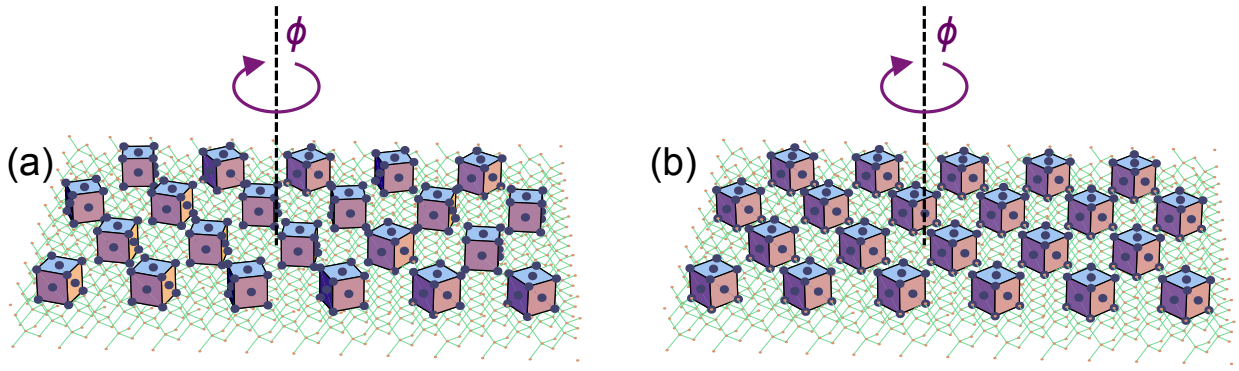

Figure 1.10: Illustration of the difference between (a) a fiber-textured film and (b) an epitaxial film. Both films are platinum grown on (100) silicon. From Schlom [172]; I added the ϕ rotation axis label.

A scan about the azimuthal angle ϕ gives information on the orientation of crystallites in the in-plane direction. If the film has a defined (rather than random) crystallographic orientation with respect to the substrate crystal lattice, then the film is considered to be epitaxial. An illustration [172] of the difference between a fiber-textured film and an epitaxial film is shown in Figure 1.10; note that both films will appear the same in a symmetric 2θ scan. The geometry of performing a ϕ scan, using the $SrTiO_3$ 101 reflection as an example, is shown and described in Figure 1.11.

1.6 Arrangement of materials in this thesis

The specific arrangement of this dissertation are as follows:

Chapter 2 This chapter describes the structural chemistry of $CsPbF_3$, the only experimentally synthesized ABF_3 fluoride perovskite with a polar ground state. We use $CsPbF_3$ (tolerance factor: 0.94) as a guide in our search for rules to rationally design new ABX_3 polar fluorides and halides from first principles and as a model compound to study the interactions of lone pairs, octahedral rotations, and *A*- and *B*-site driven ferroelectricity. We find that the lone pair cation on the *B*-site serves to stabilize a polar ground state,

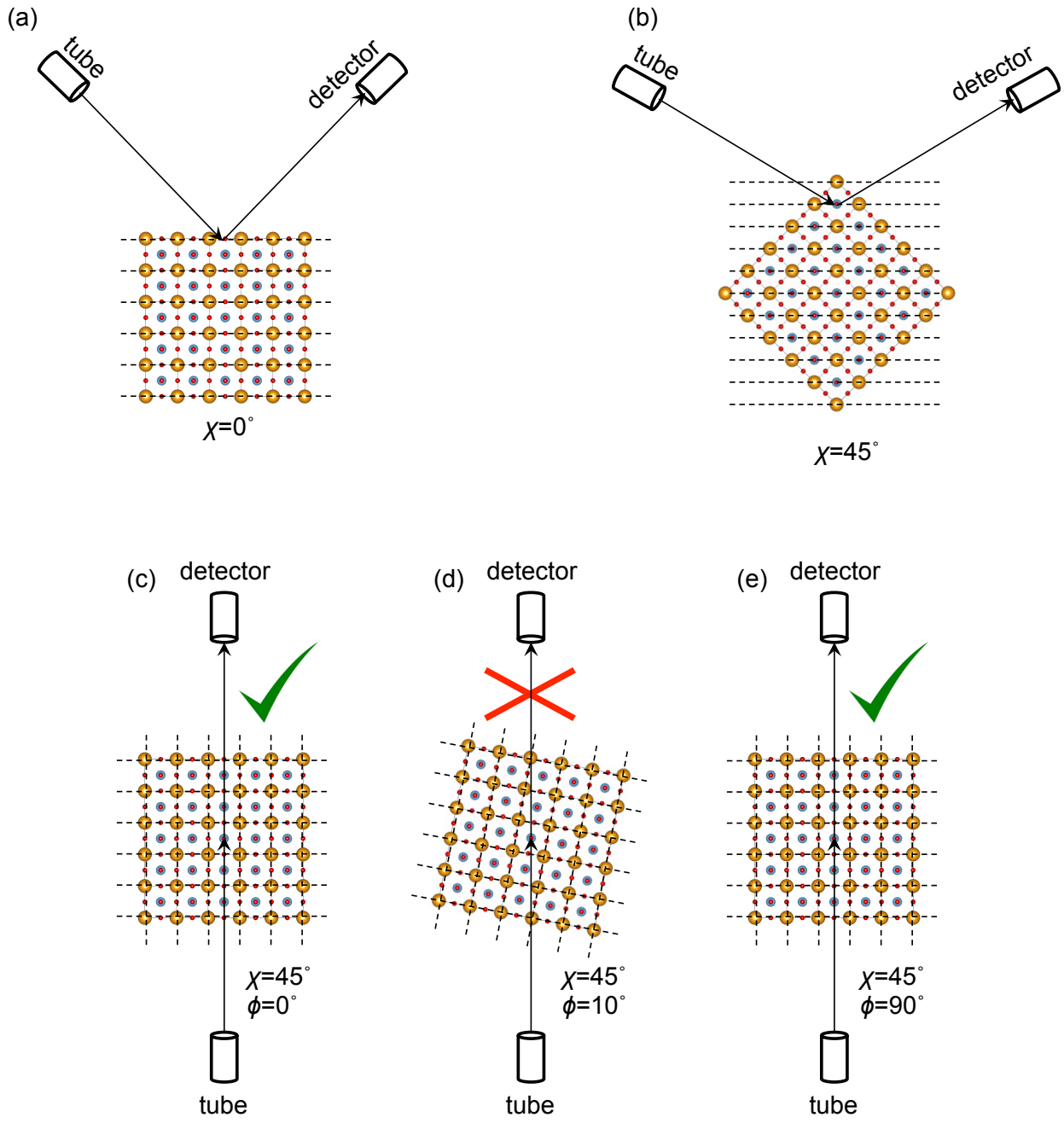

Figure 1.11: Schematics of how samples are aligned in 2θ and χ to measure reflections of cubic $SrTiO_3$. (a) The symmetric 001 reflection; (b) the 101 reflection; (c)-(e) a ϕ scan of the 101 reflection. (a) and (b) are viewed normal to the diffraction plane while (c)-(e) are viewed down the azimuthal direction. Intensity of the 101 reflection is only measured when 2θ, χ, and ϕ are all aligned, while the symmetric 001 reflection may be measured with no special ϕ alignment. 2θ and χ can be calculated *a priori* but the sample must be scanned to find the proper ϕ angle. In the example of measuring the 101 reflection of $SrTiO_3$, χ is 45° because that is the angle between the substrate normal direction [001] and the [101] direction.

analogous to the role of lone pair cations on the *A*-site of oxide perovskites. However, we also find that the lone pair determines the pattern of non-polar structural distortions – rotations of the PbF_6 octahedra – that characterize the lowest energy structure. This result is surprising since rotations are typically associated with bonding preferences of the *A*-site cation (here Cs^+), whereas the Pb^{2+} cation occupies the *B*-site. We show that the coordination requirements of the *A*-site cation and the stereoactivity of the *B*-site lone pair cation compete or cooperate via the anionic displacements that accompany polar distortions. We consider the generalizability of our findings for $CsPbF_3$ and how they may be extended to the oxide perovskites as well as to the organic-inorganic hybrid halide perovskite photovoltaics.

Chapter 3 In this chapter we report the growth of $PbTiO_3$ thin films by molecular-beam epitaxy utilizing continuous codeposition. Contrary to what would be expected from thermodynamics, whether the resulting film is single-phase $PbTiO_3$ or not at a particular temperature depends on the incident fluxes of all species, including titanium. We develop a theory of kinetics of lead oxidation on the growing film surface and find that it explains the manner in which the adsorption-controlled growth window of $PbTiO_3$ depends on lead flux, oxidant flux, and titanium flux. We successfully apply the kinetic theory to the dependence of the growth of $BiFeO_3$ on oxidant type and surmise that the theory may be generally applicable to the adsorption-controlled growth of complex oxides by MBE.

Chapter 4 This chapter describes double-diffraction in thin films. We have observed in symmetric θ-2θ scans of phase-pure thin films grown on single-crystal substrates peaks that correspond to neither the film nor the substrate crystal structure. We argue here that these peaks are the result of multiple, sequential diffraction events that occur from both the film and substrate. The occurrence of so-called "hybrid" reflections, while described in the literature, is not widely reported within the thin-film community. We describe here a simple method to predict and identify peaks resulting from hybrid reflections. To

demonstrate the use of these methods, as well as to argue that hybrid reflections may be widespread in thin epitaxial films, we give four examples in which we have identified such reflections from our own samples.

Chapter 5 This chapter summarizes the conclusions from this dissertation and presents possible future directions for work.

1.7 Contributions

Chapter 2 In this chapter, $CsPbF_3$ was studied using density-functional theory. I designed experiments, performed simulations, constructed arguments, and was the primary writer of the manuscript. Nicole had the original idea to investigate ferroelectricity in $CsPbF_3$ and gave guidance on the science and presentation of the manuscript. Craig oversaw the project and offered guidance at all stages.

Chapter 3 In this chapter, $PbTiO_3$ and $BiFeO_3$ were grown by MBE and a theory for oxidation kinetics described. I grew the $PbTiO_3$ films, formulated the kinetic theory, and was the primary writer of the manuscript. Jon Ihlefeld grew the $BiFeO_3$ films, contributed to discussions of oxidation kinetics, wrote portions of the manuscript, and gave guidance on the science and presentation of the manuscript. Hanjong and Yuefeng taught me how to grow $PbTiO_3$ and had taught me that growth rate (kinetics) were very important in this system. Carolina helped Jon with growing $BiFeO_3$. Tassilo was heavily involved with designing and building the ozone distillation system for the $BiFeO_3$ and $PbTiO_3$ growths. Zi-Kui performed thermodynamic calculations for the growth window of $BiFeO_3$. Darrell oversaw the project, was actively involved in improving the science and presentation, and offered guidance at all stages.

Chapter 4 In this chapter, thin films of several materials were analyzed by x-ray

diffraction. I designed and performed the x-ray diffraction experiments, analyzed and contextualized the data, and was the primary writer of the manuscript. Phil grew the La_2NiO_4 film. Natalie grew the $Sr_2BaTi_2O_7$ film and offered feedback on the manuscript. Darrell oversaw the project, was actively involved in improving the science and presentation, and offered guidance at all stages.

Chapter 5 In this chapter I summarize the conclusions from this dissertation and present possible future directions for work, including ongoing projects not otherwise described in this dissertation. I was the primary writer of this chapter.

CHAPTER 2

INTERPLAY OF OCTAHEDRAL ROTATIONS AND LONE PAIR FERROELECTRICITY IN $CsPbF_3$

Adapted slightly with permission from: Smith, Eva H.; Benedek, Nicole A.; and Fennie, Craig J. *Inorg. Chem.*, **2015**, *54* (17), pp 8536-8543.

2.1 Abstract

$CsPbF_3$ is the only experimentally synthesized ABF_3 fluoride perovskite with a polar ground state. We use $CsPbF_3$ as a guide in our search for rules to rationally design new ABX_3 polar fluorides and halides from first principles and as a model compound to study the interactions of lone pairs, octahedral rotations, and *A*- and *B*-site driven ferroelectricity. We find that the lone pair cation on the *B*-site serves to stabilize a polar ground state, analogous to the role of lone pair cations on the *A*-site of oxide perovskites. However, we also find that the lone pair determines the pattern of non-polar structural distortions – rotations of the PbF_6 octahedra – that characterize the lowest energy structure. This result is remarkable since rotations are typically associated with bonding preferences of the *A*-site cation (here Cs^+), whereas the Pb^{2+} cation occupies the *B* site. We show that the coordination requirements of the *A*-site cation and the stereoactivity of the *B*-site lone pair cation compete or cooperate via the anionic displacements that accompany polar distortions. We consider the generalizability of our findings for $CsPbF_3$ and how they may be extended to the oxide perovskites as well as to the organic-inorganic hybrid halide perovskite photovoltaics.

2.2 Introduction

While a great body of research has been devoted to the study of and search for design principles for polar and ferroelectric oxide perovskites, polar or ferroelectric *fluoride* perovskites have not received nearly as much attention. There are about 120 combinations of monoatomic cations A^+ and B^{2+} that, if combined with F^- in stoichiometry ABF_3, would exhibit Goldschmidt tolerance factors [72] between 0.76 and 1.13, the criterion for stability for fluoride perovskites [14]. Between the Inorganic Crystal Structure Database [59] and the Landolt-Börnstein tables [6] we located structural reports for nearly 70 stoichiometric ABF_3 perovskites. The great majority of these reports are for experimentally synthesized structures characterized at room temperature. Computational and low-temperature reports are scarce.

$CsPbF_3$ (tolerance factor, t: 0.94) is the only ABF_3 perovskite experimentally observed to form in a polar structure and is one of few inorganic ABX_3 perovskites with a lone-pair cation (here Pb^{2+}) on the B-site. Rather than being merely a curiosity, on the contrary this positions $CsPbF_3$ as a bridge between the the extensive inorganic (mostly oxide) perovskite literature, and the rapidly-growing field of hybrid organic-inorganic halide perovskite photovoltaics in which the A-site cation is a small organic molecule, the B-site cation is most often Pb^{2+} but occasionally another 2+ lone-pair cation, and the anions are halides [73, 108, 118]. Because of the great technological importance of the oxide perovskites and of the hybrid perovskite photovoltaics, we use our findings for $CsPbF_3$ to shed light on both families of materials.

The low-temperature polar $R3c$ phase (space group #161) of $CsPbF_3$ is reached by a discontinuous transition at 186 K from the high-temperature $Pm\bar{3}m$ (space group #221) cubic perovskite structure [23]. The $R3c$ structure is obtained from $Pm\bar{3}m$ by a rotation of the PbF_6 octahedra about the [111] axis with respect to the cubic perovskite cell

(Glazer tilt pattern [71] $a^-a^-a^-$) followed by polar displacements along the same axis. It is surprising that $CsPbF_3$ adopts a rhombohedral structure because extensive crystal chemical studies of oxides have shown that the stability of the rhombohedral distortion depends on the crystal Madelung energy [215] and therefore decreases as the charge of the *A*-site cation decreases. In addition, although first-principles and lattice energy calculations have shown that the Glazer tilt patterns $a^-b^+a^-$(leading to space group *Pnma*, #62) and $a^-a^-a^-$ (leading to space group $R\bar{3}c$, #167) are energetically comparable in most perovskites, repulsive anion-anion interactions in $a^-a^-a^-$ increase as the tilting angle increases [195, 215]. Given these observations, an ABF_3 perovskite with a monovalent *A*-site cation would not be expected to adopt a rhombohedral structure. Indeed, Berastegui and co-workers [23] noted that of the perovskite fluorides reported in the ICSD, none except $CsPbF_3$ are rhombohedral. The fact that $CsPbF_3$ is polar is also somewhat surprising, since the greater ionicity of the fluoride bond [14] (compared to oxides) is generally thought [68] to disfavor the acentric displacements required for ferroelectricity.

We have used first-principles calculations and simple crystal chemical models to demonstrate that the Pb^{2+} lone pair of polar fluoride perovskite $CsPbF_3$ is responsible for both the ferroelectricity and particular octahedral rotation pattern of its lowest energy structure. The Pb^{2+} cation occupies the *B*-site, while octahedral rotations primarily affect the *A*-site coordination polyhedron; we consider the mechanisms by which the two cationic sites influence each other. We demonstrate that localization of the Pb^{2+} lone pair requires significant anionic displacements, which also modify the *A*-site environment. Whether these modifications are favorable or unfavorable depends strongly on octahedral rotation pattern; unfavorable interactions suppress lone pair localization, while favorable interactions characterize the lowest energy structure. Our work thus demonstrates the mechanism by which cationic lone pairs may influence both polar and non-polar structural distortions, as well as how the interplay between the chemistries of the *A* and *B* cations gives rise to the ground state.

2.3 Computational methods

Calculations were performed using the PBEsol functional [156] as implemented in the Vienna *ab initio* Simulation Package (VASP) [111, 112], with a plane wave cutoff of 600 eV and a $5 \times 5 \times 5$ Γ-centered k-point mesh. Lattice dynamical properties (phonon modes and frequencies) were calculated using Density Functional Perturbation Theory [17, 66], and phonon frequencies were converged to within 5 cm^{-1} with respect to energy cutoff and k-point mesh. Relaxations were considered complete when residual forces on all atoms were less than 0.25 meV/Å. PAW potentials supplied by the VASP package [113] were used, with the following valence states. Cs: $5s^2 5p^6 6s^1$; Sr: $4s^2 4p^6 5s^2$; Pb: $5d^{10} 6s^2 6p^2$; F: $2s^2 2p^5$. Tolerance factors and bond valences were calculated using Brese and O'Keeffe's bond valence parameters [29] assuming a 12-coordinate *A*-site cation and a 6-coordinate *B*-site cation unless otherwise noted. The *b* value of 0.37 typically used in the literature was used throughout. Our crystallographic analyses were performed using the ISOTROPY package [186] and the AMPLIMODES program of the Bilbao Crystallographic Server [10, 11, 12, 151, 157]. Wannier90 [142] was used to find the orbital-projected densities of states [109] starting from a high-accuracy electronic structure calculated with VASP. For density of states calculations, a 12×12×12 k-point mesh was used. Crystal structures were visualized using VESTA [135]. Software version information is given in the Supplementary Information.

All Miller indices are with respect to the cubic perovskite cell. We use the terms "ferroelectric" and "ferroelectricity" to refer a polar structure within a family of symmetry-equivalent structures with equal polarization magnitude but different polarization directions. When multiple settings of a space group are allowed, we give the International notation symbol corresponding to a unique *b* axis. LO-TO splitting of zone-center phonon mode frequencies is found using Phonopy [199].

Irrep	$CsPbF_3$ ω, cm^{-1}	$CsSrF_3$ ω, cm^{-1}	Description
Γ_4^-	*i*60, *i*58	25, 73	Polar mode
Γ_5^-	*i*33	61	Antipolar F motion
M_3^+	*i*76	*i*52	In-phase octahedral rotation
M_5^-	*i*45	13	Antipolar Pb motion
R_4^+	*i*79	*i*58	Out-of-phase octahedral rotation
X_5^-	*i*38	47	Antipolar F motion

Table 2.1: Comparison of phonon modes for $CsPbF_3$ and $CsSrF_3$ in the fully relaxed cubic perovskite structure (space group $Pm\bar{3}m$). Modes with imaginary frequencies indicate structural instabilities. All unstable modes for both compounds are listed. In $CsSrF_3$, the softest LO and softest TO Γ_4^- phonon frequencies are given. The two types of octahedral rotations are illustrated in Figure 2.1. Phonon band structures and phonon densities of states for $CsPbF_3$ and $CsSrF_3$ are given in the Supplementary Information, Figure 2.7.

2.4 Results and discussion

2.4.1 Influence of the lone pair in the structural distortions and ground state of $CsPbF_3$ compared to $CsSrF_3$

Stereoactive cationic lone pairs drive ferroelectricity in a number of perovskite oxides (*e.g.* $PbTiO_3$, $BiFeO_3$) but are not localized in others (*e.g.* $PbCrO_3$ [168], $BiScO_3$ [19], $BiGaO_3$ [20]). To elucidate the role of the Pb^{2+} lone pair in the ferroelectricity of $CsPbF_3$, we compare $CsPbF_3$ to $CsSrF_3$; Sr^{2+} has almost the same ionic radius (1.18 Å) as Pb^{2+} (1.19 Å) [179] in octahedral coordination, but no lone pair. Table 2.1 shows that whereas $CsPbF_3$ is unstable to both polar distortions and octahedral rotations, $CsSrF_3$ is only unstable to octahedral rotations and has no polar instability, indicating that ferroelectricity in $CsPbF_3$ is driven by the Pb^{2+} lone pair. We find that the lowest energy structure of $CsSrF_3$ is *Pnma* (established by a combination of rotation distortions transforming like the irreducible representations [irreps] M_3^+ and R_4^+, bottom right corner of Figure 2.1), consistent with what

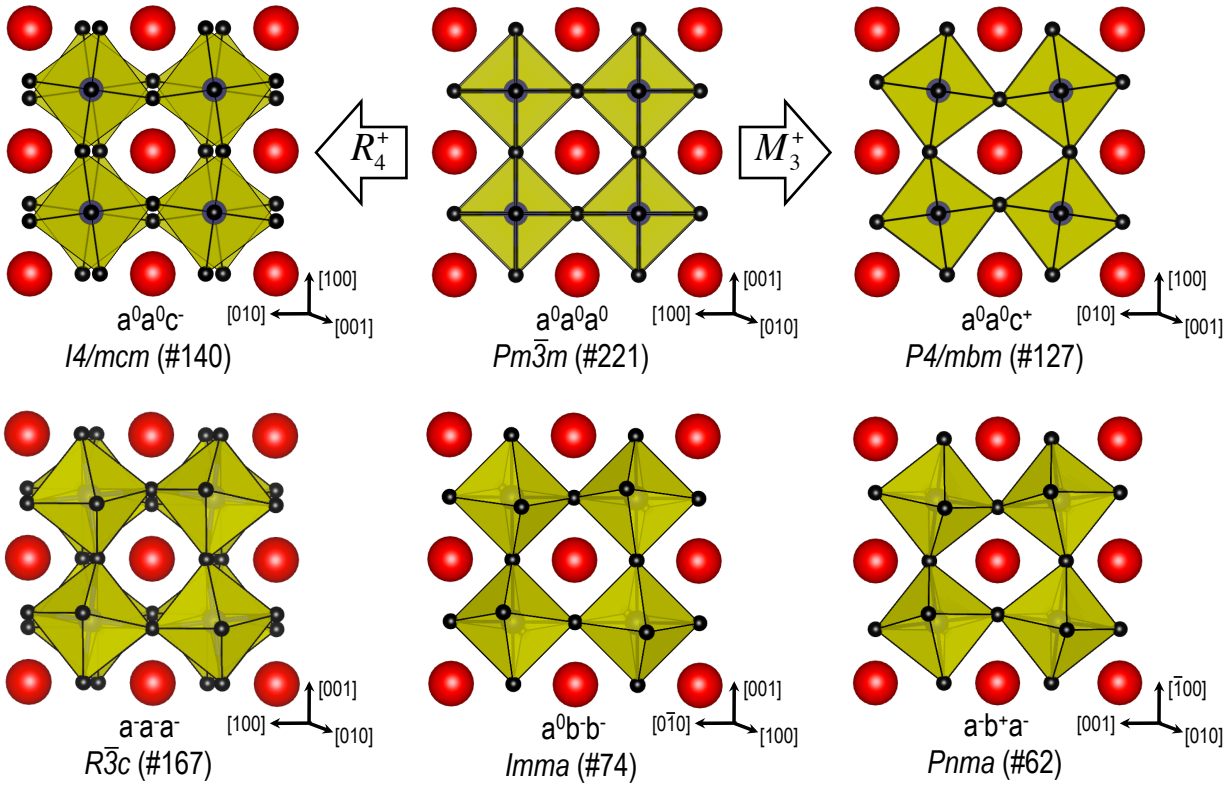

Figure 2.1: Illustration of "in-phase" (irrep M_3^+, top right) and "out-of-phase" (irrep R_4^+, top left) octahedral rotations about the [001] axis acting on the $Pm\bar{3}m$ aristotype (top center), as well as illustration of how rotations about multiple axes modify the structure (bottom row). Magnitudes a, b, and c are chosen arbitrarily for structures shown. Axes are with respect to the cubic aristotype unit cell, hereafter referred to as the pseudocubic unit cell. A-site cations are shown as red spheres and B-site cations sit in the centers of the yellow anion octahedra.

one would expect [125] for an oxide perovskite of the same tolerance factor (0.95).

In contrast to $CsSrF_3$, we find that the ground state structure of $CsPbF_3$ is $R3c$, in agreement with the reported experimental low-temperature structure [23]. The reported and as-calculated $R3c$ structures are compared in the Supplementary Information, Table 2.3, with good agreement. Interestingly, although Table 2.1 shows that the octahedral rotation instabilities (M_3^+ and R_4^+) are present in both materials, $CsPbF_3$ adopts a structure with the $a^-a^-a^-$ tilt pattern, which is associated with R_4^+ only. As Figure 2.2 shows, $R3c$ and $Pnma$ structures are in close energetic competition in $CsPbF_3$, as is the case in many oxide perovskites. How does the lone pair mediate the competition among different octahedral

rotation patterns and between polar and non-polar structures to make *R*3*c* the ground state of $CsPbF_3$? Why does the (polar) ground state of $CsPbF_3$ exhibit the $a^-a^-a^-$ rotation pattern rather than the much more common $a^-b^+a^-$?

2.4.2 Lone pair stereoactivity is not sensitive to octahedral rotation pattern

Since the ferroelectricity of $CsPbF_3$ appears to be driven by the stereoactivity of the Pb^{2+} lone pair, we compare the lone pair stereoactivity in structures with the $a^-a^-a^-$ and $a^-b^+a^-$ rotation patterns. We define *stereoactivity* as the chemical tendency (described below) of a lone-pair cation to undergo an inversion-breaking distortion (lone pair localization), while *lone pair-driven ferroelectricity* describes whether such a distortion is energetically favorable.

The stereoactivity of the Pb^{2+} lone pair is the result of mixing of the formally empty Pb 6*p* orbital with the Pb 6*s*-F 2*p* σ^* orbital [207, 208]. Such mixing requires both spatial overlap and energetic proximity between the Pb 6*p* and the σ^* orbitals. The Pb 6*p* and 6*s* orbitals are both localized about the Pb^{2+} cation; thus, the degree of spatial overlap between the Pb 6*p* and the σ^* orbitals is dependent upon the amount of Pb 6*s* character in the σ^* orbital. The σ^* orbital sits at the top of the valence band of $CsPbF_3$, while the bottom of the conduction band is primarily Pb 6*p*. Thus, the energetic proximity between these orbitals is described by the bandgap. Octahedral rotation patterns or other distortions that increase the Pb 6*s* character in the σ^* orbital and decrease the bandgap would enhance lone pair stereoactivity.

While only the R_4^+ and M_3^+ octahedral rotation modes are necessary to establish the *Pnma* symmetry, three other secondary modes are allowed by that symmetry as well. The

X_5^+ mode, corresponding to antipolar *A*-site motion, is one such mode and the one that in oxide perovskites is typically the largest in magnitude after the R_4^+ and M_3^+ modes [21]. Because of the known role of the X_5^+ mode in suppressing the ferroelectric instability in *Pnma* perovskites [21], we consider both the fully-relaxed *Pnma* structure and *Pnma* with antipolar displacements manually removed [5]. We refer to this artificially-constructed structure as a*Pnma*, in which the "a" stands for "antipolar displacement-free," and the fully-relaxed structure as r*Pnma*.

We examine the densities of states of $CsPbF_3$ in the $R\bar{3}c$, a*Pnma*, and r*Pnma* structures to determine how their different octahedral rotation patterns and antipolar displacements affect the lone pair stereoactivity, and find no qualitative differences (see Figure 2.8, Supplementary Information). In particular, among these three structures there is no qualitative difference in the amount of Pb 6*s* character in the σ^* orbital, indicating comparable Pb 6*p*-σ^* spatial overlap; nor is there a qualitative difference in the bandgap, indicating comparable Pb 6*p*-σ^* energetic proximity. Hence, the chemical stereoactivity of the Pb^{2+} lone pair is not sensitive to the octahedral rotation pattern or to antipolar displacements in these non-polar space groups.

2.4.3 *A*-site coordination can be optimized by polar displacements in structures with $R\bar{3}c$ but not *Pnma* symmetry

Although the ferroelectricity in $CsPbF_3$ is driven by the Pb^{2+} lone pair, the Cs^+ cation plays a significant role in the crystal chemistry of this compound. As Table 2.2 shows, Cs makes a larger contribution than Pb to the ferroelectric eigenvector of $Pm\bar{3}m$, a*Pnma*, r*Pnma*, and $R\bar{3}c$ $CsPbF_3$. What role does the Cs^+ cation play in the ferroelectricity of $CsPbF_3$ and in determining the octahedral rotation pattern?

	$Pm\bar{3}m$	$R\bar{3}c$	a*Pnma*	r*Pnma*
Cs	0.4103	0.2366	0.4851	0.1414
Pb	0.1381	0.1296	0.2763	0.0296
$F_{\parallel}$	0.3592	0.3781	0.5564	0.3105
$F_{\perp}$	-0.5846	-0.6262	-0.4352	-0.6644

Table 2.2: Normalized decomposition of the softest polar force constant matrix eigenmode of various $CsPbF_3$ structures. Anionic displacements are labelled as either parallel ($F_{\parallel}$) or perpendicular ($F_{\perp}$) to the Pb-F bond.

To test whether the antipolar displacements present in r*Pnma* are responsible for suppressing ferroelectricity in this structure, we calculated the frequency of the polar modes in a*Pnma*. In agreement with the results of Benedek and Fennie [21], removing antipolar displacements does restore ferroelectricity, but the frequency of the polar mode in a*Pnma* ($i17$ cm^{-1}) is much harder than in $R\bar{3}c$ ($i58$ cm^{-1}). Both polar modes, however, are associated with lone pair localization: a localized Pb^{2+} lone pair is visible in the electron densities of polar subgroups of both $R\bar{3}c$ and a*Pnma* (shown in Figure 2.2).

Figure 2.2 further shows that if we freeze in the polar eigenmode of a*Pnma* to form a structure of space group $P2_1ma$ (#26), the structure is stabilized by only 1.0 meV. This is substantially less than the amount that $R\bar{3}c$ is stabilized by its own polar mode (8.0 meV) and also less than the energy difference between r*Pnma* and fully-relaxed $R3c$ (1.6 meV). Even if the antipolar displacements of r*Pnma* had no effect on its ferroelectricity, $R3c$ would still be lower in energy than a polar subgroup of *Pnma*. Hence, the hardening effect of *A*-site antipolar displacements is not sufficient to explain why the ground state of $CsPbF_3$ is a polar subgroup of $R\bar{3}c$ rather than of *Pnma*. As we will see however, *A*-site coordination preferences do play an important role both in the ferroelectricity of $CsPbF_3$ and in determining its ground state octahedral rotation pattern.

We use the bond valence model [32, 33] to explore the Cs coordination in various structures. Brese and O'Keeffe [29] give a bond valence parameter $R_{\text{Cs-F}}$ of 2.33±0.02 Å for a Cs-F bond. This is an empirical value calculated through averaging over many

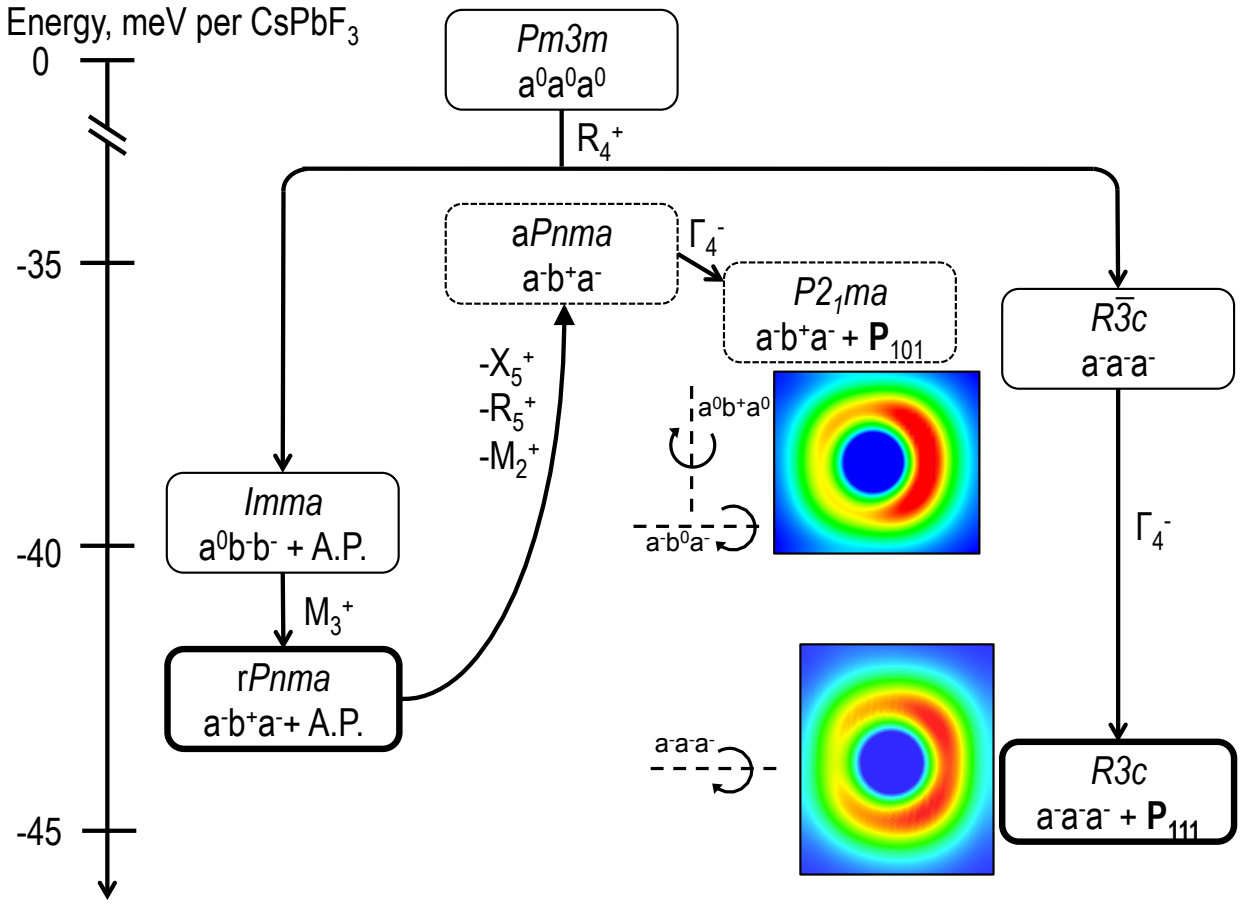

Figure 2.2: Stabilization per $CsPbF_3$ stoichiometric unit of structures with the $a^-b^+a^-$ and $a^-a^-a^-$ rotation patterns by polar and antipolar *A*-site displacements. Electron density maps are of the band corresponding to the σ^* orbital, spatially projected about the Pb^{2+} cation and cut in cross-section. Red corresponds to areas of greatest electron density. "A.P." denotes any and all antipolar displacement patterns that are commensurate with the space group produced by a given rotation pattern. Bold outlines indicate dynamically-stable structures, thin solid outlines metastable structures, and dashed lines "frozen" structures that are not stable under internal relaxations. For both electron density maps, the polar mode is frozen in at an amplitude of $0.06a$ per formula unit, where a is the $Pm\bar{3}m$ lattice constant. All irreducible representations are with respect to a $Pm\bar{3}m$ basis.

structures. Because fully-relaxed *Pnma* optimizes the *A*-site cation environment, we use it as a guide to adjust $R_{\text{Cs-F}}$ for $CsPbF_3$ such that Cs in r*Pnma* has a bond valence sum of +1.000, its nominal value. We find that an appropriate value of $R_{\text{Cs-F}}$ is 2.3505 Å.

By tracking changes to the Cs bond valence sum as the softest polar modes of $R\bar{3}c$, a*Pnma*, and r*Pnma* are frozen in at increasing magnitude, we compare how well a polar mode optimizes the *A*-site coordination environment in these different space groups. Figure 2.3 shows that for all structures considered, the polar mode increases the Cs bond valence sum. The polar mode of $R\bar{3}c$ brings the Cs bond valence sum closer to unity. However, the bond valence sums of non-polar r*Pnma* and a*Pnma* are already at or above unity, and the increase results in overcoordination of the *A*-site cation. While by our definition and construction the Cs coordination of r*Pnma* cannot be improved by any distortion, the same cannot be said for that in a*Pnma*. The X_5^+ and other antipolar modes found in r*Pnma* move the Cs^+ cations to improve their coordination. Why can the antipolar modes improve the Cs bond valence sum of a*Pnma*, but a polar mode does not?

Woodward [215] describes in detail the crystal chemistry of the antipolar cationic displacements that stabilize the *A*-site cation coordination environment in *Pnma*. As octahedral rotations become large, the bonds between the *A*-site cation and its three anionic nearest neighbors become too short. To lengthen these bonds and stabilize the structure, the *A*-site cation shifts away from them, along the black vector shown in Figure 2.4a (reproduced with permission from Woodward [215]). The spatial arrangement of the CsF_3 units in a*Pnma* $CsPbF_3$, as well as the three shortest Cs-F bond lengths, is shown in Figure 2.4b.

Due to the symmetry of space group *Pnma*, each CsF_3 polyhedron is inverted relative to its neighbors along the pseudocubic [010] axis (the axis about which the in-phase octahedral rotations have occurred), inverting these displacement vectors as well. The resulting globally-antipolar displacement pattern optimizes the bonding environment of

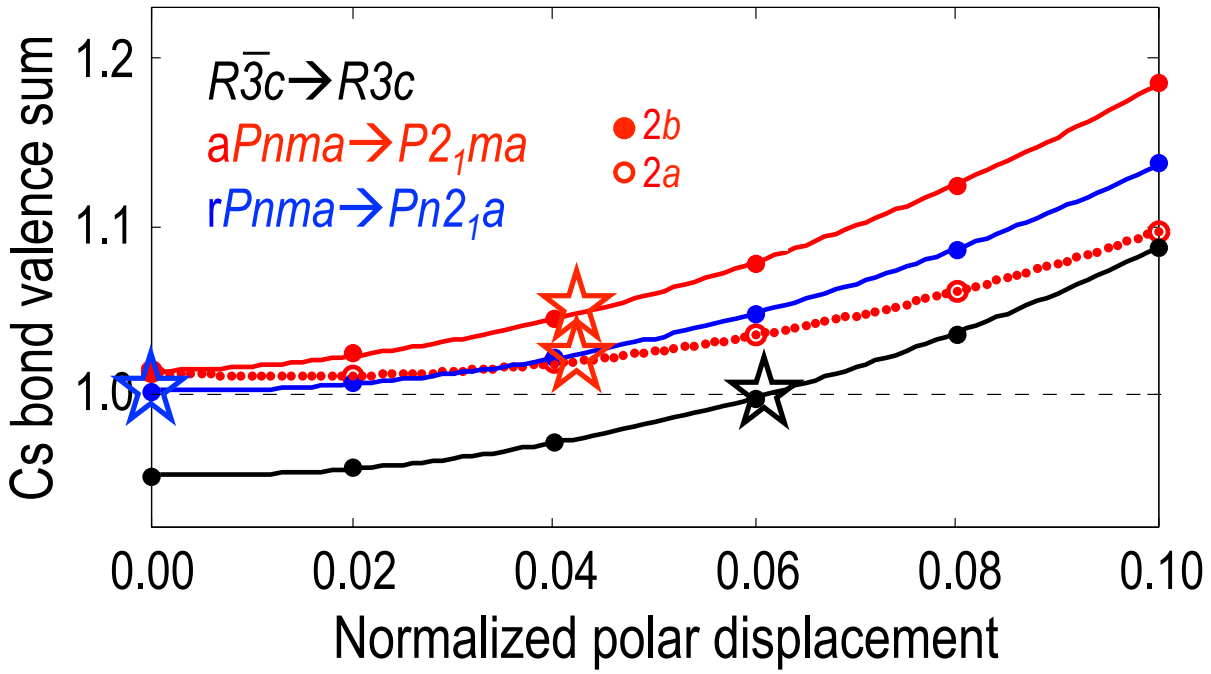

Figure 2.3: Cs bond valence sum for subgroups of $CsPbF_3$ calculated using our modified $R_{Cs\text{-}F}$ value of 2.3505 Å. Use of Brese's $R_{Cs\text{-}F}$ of 2.33 instead would cause a nearly-static shift to slightly lower values (0.898 for non-polar $R\bar{3}c$, 0.946 for non-polar r*Pnma*, 0.956 for non-polar a*Pnma*). The polar subgroup of a*Pnma*, $P2_1ma$, has two inequivalent Cs^+ cations, whose bond valences are plotted individually and which are labeled by Wyckoff position in $P2_1ma$; all other non-polar parent structures and polar subgroups have just one unique Cs^+ site. Stars indicate the frozen polar structure with the lowest energy for each subgroup. Polar displacement magnitudes are given with respect to the lattice constant of $Pm\bar{3}m$ per formula unit. Curves are to guide the eye. The polar subgroup of the r*Pnma* structure is $Pn2_1a$, #33.

all *A*-site cations in the crystal simultaneously, as shown in Figure 2.4c. A globally-polar (ferroelectric) displacement pattern, on the other hand, breaks the symmetry of the CsF_3 units. Figure 2.4d shows the change to the CsF_3 units and the Cs-F bond lengths when the softest polar mode of a*Pnma* is frozen in, to give a structure of space group $P2_1ma$, along with the displacement vectors taken by each Cs^+ cation. In half of the CsF_3 units of $P2_1ma$ the Cs-F bonds are longer than in a*Pnma*; in the other CsF_3 units of $P2_1ma$ the Cs-F bonds have been *shortened*! As the Cs displacements are driven by the need to lengthen the bonds of the CsF_3 units, it is easy to see why such a polar displacement pattern is less favorable than the antipolar one.

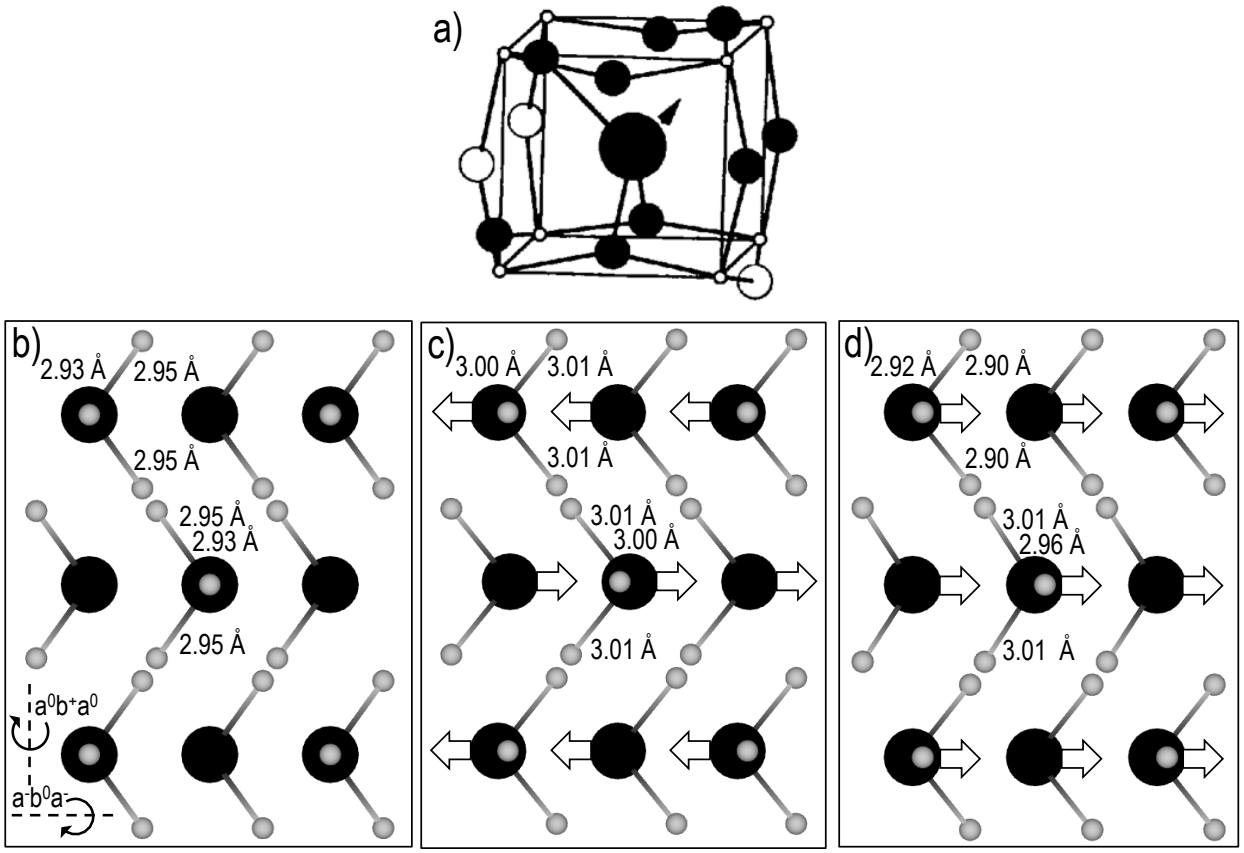

Figure 2.4: *A*-site coordination environments in $CsPbF_3$. Cs^+ or the *A*-site cations are shown as large black spheres throughout. In parts b-d the F^- are shown as light gray spheres and polar or antipolar displacements taken by the Cs^+ cations relative to the anion sublattice as white arrows. Bond lengths given for the three shortest Cs-F bonds. a) The *A*-site cation and the bonds to its three nearest neighbor anions in a structure with *Pnma* symmetry, with the optimal cationic displacement vector shown as a black arrow. Reproduced from Woodward [215] with permission of the International Union of Crystallography: http://dx.doi.org/10.1107/S0108768196012050. b) The CsF_3 units of a*Pnma* $CsPbF_3$. c) The CsF_3 units of r*Pnma* $CsPbF_3$. d) The CsF_3 units of a*Pnma* $CsPbF_3$ with its softest polar phonon mode frozen in giving space group $P2_1ma$.

We now turn from space group *Pnma* to $R\bar{3}c$. Unlike in a*Pnma*, the *A*-site of $R\bar{3}c$ is undercoordinated, not overcoordinated (as seen in Figure 2.3). The *A*-site cation of $R\bar{3}c$ sits in a 3+6 coordinate environment, with the 3 short bonds co-planar with the *A* cation. The displacements that transform $R\bar{3}c$ to $R3c$ lengthen the 3 shortest *A*-*X* bonds while shortening 3 of the other 6 by moving the *A* cation along the pseudocubic [111] axis (the axis about which the octahedra have rotated) [21]. Based on the site symmetry of the

A-site in $R\bar{3}c$, displacements of a given *A*-site cation in either the [111] direction or the antiparallel $[\bar{1}\bar{1}\bar{1}]$ direction are equivalent by symmetry. Thus, moving the *A*-site cations in a globally-parallel pattern has the same effect on their local environments as moving them in an antiparallel one. As a result of $R\bar{3}c$ symmetry, *unlike in Pnma, displacing all A-site cations of* $R\bar{3}c$ *in parallel can optimize all the A-site coordination environments simultaneously.*

Our findings are consistent with previous work regarding the stabilization of polar subgroups of *Pnma* perovskites using biaxial tensile strain. In both $CaTiO_3$ [56] and $CaMnO_3$ [25], +2% biaxial strain in the pseudocubic (010) plane (normal to the M_3^+ rotation axis) softens polar phonon modes of *Pnma* and stabilizes a polar subgroup. For both compounds the stabilized polarization vector lies in the (010) plane; in $CaTiO_3$ polarization in the pseudocubic $[10\bar{1}]$ direction (resulting in subgroup $Pnm2_1$, #31) is slightly more favorable than in the [101] (resulting in subgroup $P2_1ma$, the same as the polar subgroup of a*Pnma* $CsPbF_3$), through structures with polarization in either direction are dynamically-stable. Bhattacharjee and co-workers [25] comment that tensile strain "provides more space for the ferroelectric distortion" – in concord with our finding that overcoordination of the *A*-site cation by polar distortions is responsible for the disfavoring of polar instabilities in *Pnma*.

2.4.4 Anionic displacements mediate the interaction between *B*-site lone pair-driven ferroelectricity and *A*-site coordination environment

We now address how the *A*-site bonding preferences, which disfavor polar phonon instabilities, suppress the *B*-site lone pair-driven ferroelectricity in *Pnma* $CsPbF_3$. Historically, ferroelectric distortions in perovskites have been described as polar displacements

of the cations against rigid anion octahedra [122]. However, it is now appreciated that distortions of the anion octahedra, in addition to cationic displacements, are important [69, 74, 116].

We refer back to Table 2.2 for the contribution of anionic displacements to the polar force constant matrix eigenvectors of $CsPbF_3$ in structures with $R\bar{3}c$ and *Pnma* symmetry, the latter both with and without antipolar displacements. In all three structures the anionic displacements are large. As seen in the inset of Figure 2.5, the polar eigenvectors of these structures distort the PbF_6 octahedra substantially, which will have the effect of changing not just the *B*-site environment but the *A*-site one as well.

We compare in Figure 2.5 how the energy of $R\bar{3}c$, a*Pnma*, and r*Pnma* evolves when freezing in to each structure its complete softest polar eigenvector, to how the energy evolves when the anionic displacements are suppressed. We give the displacement magnitude of the complete eigenvector with respect to the $Pm\bar{3}m$ lattice constant per formula unit. Freezing in the complete eigenvectors of $R\bar{3}c$ and a*Pnma* lowers the energy of both structures. However, when anionic displacements are suppressed, the energy of both structures instead increases monotonically. (The softest polar eigenvector of r*Pnma* has a positive force constant, so even the complete eigenvector increases the energy when frozen in.)

As shown in Figure 2.10 (see Supplementary Information), anionic displacements increase the mixing of the Pb 6*p* with the Pb 6*s*-F 2*p* σ^* orbital, and thus lone pair stereoactivity. Furthermore, structures in the polar subgroups of $R\bar{3}c$, a*Pnma*, and r*Pnma* all exhibit more Pb *s* in the conduction band and more Pb *p* in the valence band when the anionic displacements are present. Hence, the stereoactivity of the lone pair is sensitive to the anionic displacements that accompany the polar distortion. This is in contrast to its insensitivity, shown earlier, to the anionic displacements that characterize the octahedral rotation patterns of non-polar $R\bar{3}c$, a*Pnma*, and r*Pnma*. *Anionic displacements, which mod-*

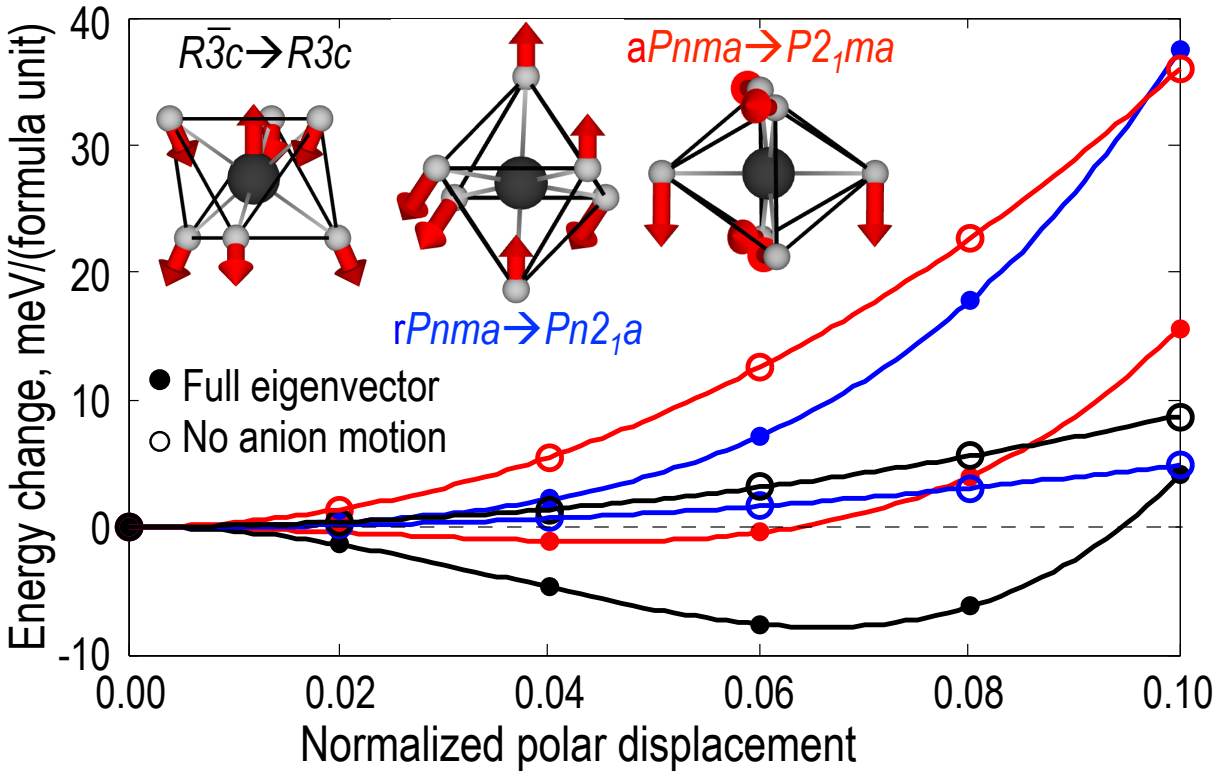

Figure 2.5: Variation of the total energy per formula unit with increasing polar displacement amplitude. Polar structures with F motion are made by freezing in the softest polar force constant matrix eigenvector of the relevant structure at the given magnitude times the $Pm\bar{3}m$ lattice constant per formula unit. Polar structures without F motion are made in the same way but with the anionic displacements from the non-polar structure set to zero. Displacement vectors are not renormalized after F motion is removed. Lines between points serve as a guide for the eye. Results are qualitatively the same for polar distortions of $Pm\bar{3}m$ (see Supplementary Information Figure 2.9). Inset: manner in which the softest polar force constant matrix eigenvectors distort the PbF_6 octahedra. Octahedra are oriented such that motion of the Cs^+ cations (not shown) is towards the top of the page.

ify both the A- and the B-site environments, are essential to lone pair-driven ferroelectricity in $CsPbF_3$.

2.4.5 Lone pair-localizing modes favor polar rather than antipolar displacement patterns

Localization of the Pb^{2+} lone pair requires breaking local inversion symmetry about the *B*-site. This may occur as part of a global displacement pattern that is either polar or antipolar in nature. Corner connectivity of the PbF_6 octahedra dictates that as the octahedra distort with an inversion-breaking distortion in space group $R3c$, all *B*-site displacements will occur in parallel rather than in antiparallel [196]. As we show below, the same requirement of connectivity of the BX_6 octahedra also requires parallel rather than antiparallel *B*-site displacements along the pseudocubic [101] direction, the direction of the softest polar mode of a*Pnma* as well as of the antipolar displacements found in r*Pnma*. Thus the structural preference for antipolar *A*-site displacements resulting from the $a^-b^+a^-$ rotation pattern are in direct competition with the *B*-site-driven ferroelectricity.

The most pronounced structural change to the PbF_6 octahedra when distorted by the polar mode of a*Pnma*, as seen in the inset to Figure 2.5, is the elongation of one F-F edge and the shortening of the opposite edge. Figure 2.6a gives a simplified picture of how such a polar mode changes these F-F bond lengths, using a $Pm\bar{3}m$ parent structure for visual clarity. The resulting octahedral shapes, greatly exaggerated to emphasize the effects of these distortions, is shown in Figure 2.6b, as well as the orientation of the Pb^{2+} lone pairs that would localize as a result of such a distortion.

As we showed in the previous section, these anionic displacements are necessary for stabilization of polar structures and substantially enhance the orbital mixing associated with lone pair stereoactivity. The octahedral distortion pattern schematized in Figure 2.6 results in a polar arrangement of localized Pb^{2+} lone pairs. To flip half of the Pb^{2+} lone pair orientations and create a globally-antipolar lone pair pattern, the local Pb^{2+} coordination environments, *i.e*. the associated PbF_6 octahedra, would have to be flipped as well. Such

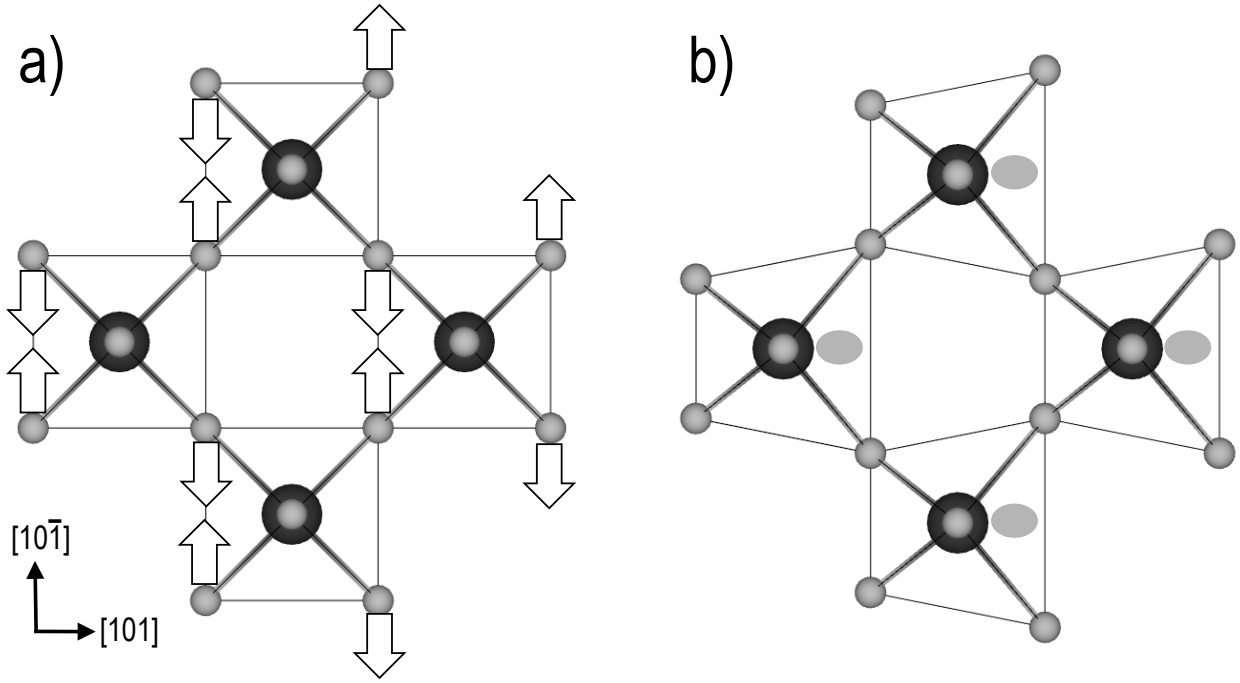

Figure 2.6: A schematic representation of a) how polarization along the [101] direction would move the F^- anions in $Pm\bar{3}m$, and b) the resulting distortions of the PbF_6 octahedra. For visual clarity, no octahedral rotations are present, F^- anions are only moved along the [10$\bar{1}$] direction, Pb^{2+} cations are not moved at all, and Cs^+ cations are not shown. Pb^{2+} are represented as large, black spheres, F^- as small, light gray spheres, Pb-F bonds as thick rods, F-F edges as thin lines, and localized Pb^{2+} lone pairs as pale gray ovals.

an arrangement would destroy the corner connectivity of the PbF_6 octahedra. Thus, not only to do anionic displacements mediate the interaction between the *B*-site lone pair-driven ferroelectricity of $CsPbF_3$ and the octahedral rotation pattern, but they also account for the polar, rather than antipolar, arrangement of the localized Pb^{2+} lone pairs in the ground state of $CsPbF_3$.

2.4.6 Implications for inorganic ABX_3 ferroelectrics, oxide perovskites, and hybrid perovskite photovoltaics

The Pb^{2+} lone pair cation stabilizes the ferroelectric ground state of $CsPbF_3$, just as *A*-site lone-pair cations may stabilize ferroelectric ground states in oxide perovskites. We showed in the previous section that *B*-site lone-pair cations will prefer to localize in a parallel arrangement, resulting in a global polarization. We therefore recommend the investigation of other ABX_3 compounds with *B*=Ge, Sn, Pb as potential ferroelectrics.

While $CsPbF_3$ is the only experimentally verified polar ABF_3 perovskite that we were able to locate in the literature, there are a few other polar ABX_3 perovskites with monoatomic, non-molecular A^+ and B^{2+} cations and *X* a halide. Thiele and colleagues [194] report that $CsGeX_3$ (*X*=Cl, Br, I) (*t*: 1.03, 1.01, 0.99) [4] all exist experimentally as *R*3*m* perovskites at room temperature, with a polarization along the [111] direction with respect to the cubic perovskite unit cell. $APbI_3$ (*A*=Cs, Rb) [30] (*t*: 0.91, 0.87) and $CsSnX_3$ (*X*=Cl, Br, I) [90] (*t*: 0.95, 0.93, 0.92) are computationally predicted to exhibit relatively high high-frequency dielectric constants and, in the case of $CsSnI_3$, imaginary-frequency polar modes [49], when constrained to the $Pm\bar{3}m$ perovskite structure. However, only $CsSnBr_3$ [141] and possibly $CsSnI_3$ [43] are experimentally stable in the perovskite structure at room temperature, and both are reported to form in non-polar structures. $CsPbI_3$ [200], $RbPbI_3$ [200], and $CsSnCl_3$ [159] are reported to form in non-perovskite phases at room temperature. $CsPbCl_3$ (*t*: 0.89) is experimentally reported to form as a non-polar perovskite with octahedral rotations [65]. $RbPbF_3$ (*t*: 0.89) is experimentally reported to form a non-perovskite structure at room temperature and undergo a phase transition to the $Pm\bar{3}m$ perovskite structure at high temperature [217].

As evidenced by the variety of both polar and non-polar phases reported in the literature, the simple presence of Ge^{2+}, Sn^{2+}, or Pb^{2+} is insufficient to guarantee a ferroelectric

perovskite ground state [187]. The stereoactivity of a lone pair cation depends not just on the cation itself but also on the anions to which it is bonded [207], as well as their interatomic spacing (bond length). Substitution of different halide anions may be used to tune the stereoactivity of a lone pair cation by changing the energetic proximity of the relevant orbitals [208]; substitution of larger or smaller *A*-site cations may be used to change the spatial overlap between those orbitals and further tune the lone pair stereoactivity, especially when tolerance factor is near or above unity and octahedral rotations are suppressed. In the non-perovskite ground state structures of $CsPbI_3$, $CsSnCl_3$, $RbPbI_3$, and $RbPbF_3$, the lone pair B^{2+} cation sits at a site with broken inversion symmetry, meaning that the lone pair may be active; in $CsSnCl_3$ and $RbPbF_3$ the *B* cations are also highly off-centered within their coordination polyhedra. It should be considered whether the *B* cation lone pairs in these latter two compounds are so highly stereoactive and favor such strongly distorted environments that the perovskite structure is destabilized.

Turning now to the applicability of our results for $CsPbF_3$ to the oxide perovskites, the reason for the weakening of ferroelectric instabilities by the $a^-b^+a^-$ rotation pattern does not depend on the presence of a *B*-site lone pair cation or on the particular chemical nature of the anion. This reasoning is therefore transferable to the oxides, though we note that *Pnma* has more than one polar subgroup, and our discussion has focused on just one of them, $P2_1ma$.

The transferability will be poorer from our findings regarding the effect of lone-pair cations on the *B*-site to the effect of lone-pair cations on the *A*-site. While we have argued that localized *B*-site lone-pair cations will prefer to orient in parallel, the equivalent statement cannot be made for localized *A*-site lone pairs: while the localized lone pairs of $PbTiO_3$ and $BiFeO_3$ orient in parallel, those of $PbZrO_3$ are oriented in an antiparallel fashion. How anionic displacements couple to the localization of *A*-site lone pairs is beyond the scope of this work, but is apparently in a manner distinct from their coupling to the

localization of *B*-site lone pairs.

We lastly turn to the organic-inorganic hybrid ABX_3 perovskite solar cell materials. Small organic molecules, protypically $CH_3NH_3^+$, sit on the *A* site; a divalent lone pair cation, nearly always Pb^{2+} but occasionally Sn^{2+}, sits on the *B* site; and heavy halides I^-, Br^-, and/or Cl^- sit on the *X* sites [73]. It is still not fully understood if the Pb^{2+} lone pairs are localized in these compounds at room temperature, or what the role of such localization would be on device performance [73]. A number of hybrid perovskite materials [63, 64, 189] with Pb^{2+} and/or Sn^{2+} on the *B*-site do form in polar structures or even exhibit ferroelectricity; however, as of yet studies have focused upon the role of the organic molecules in these phenomena [63, 64], not the cationic lone pair. The high dielectric constant of prototypical hybrid perovskite photovoltaic $(CH_3NH_3)PbI_3$ has been identified as an important contributor to its high efficiency [64]. Because the dielectric constant of a material will diverge as a proper ferroelectric transition is approached [161], we suggest tuning lone pair stereoactivity to approach a lone pair-driven ferroelectric transition as a means to further improve these already very successful materials.

We apply our design rules for tuning lone pair stereoactivity to the hybrid $APbX_3$ perovskites, using $(CH_3NH_3)PbI_3$ as an example. Approximating the *A*-site cation as a sphere, increasing its size in the absence of octahedral rotations will lengthen the Pb-*X* bonds and decrease lone pair stereoactivity. On the other hand, using smaller halides (Br^- and/or Cl^-) would increase lone pair stereoactivity both by favoring shorter Pb-*X* bonds and by increasing the energetic proximity of the relevant Pb and *X* orbitals [208]. While the efficiency of a photovoltaic device depends on many factors that we have not treated here, we believe that tuning the lone pair stereoactivity in this way has the potential to increase device performance.

2.5 Conclusions

We have used first-principles calculations to study the origin of ferroelectricity in the only ABF_3 compound that has been experimentally shown to exist as a perovskite with a polar ground state. Because the lone pair-free analogue of $CsPbF_3$, $CsSrF_3$, lacks a polar instability, we attribute the ferroelectricity of $CsPbF_3$ to the Pb^{2+} lone pair.

We find that the polar ground state of $CsPbF_3$, space group $R3c$, is in close energetic competition with a non-polar structure of space group *Pnma*, which lacks a polar instability. Even in the absence of antipolar displacements, the $a^-b^+a^-$ rotation pattern weakens ferroelectric instabilities relative to the $a^-a^-a^-$. There are no qualitative differences in the Pb *s*- and Pb *p*-projected densities of states among $R\bar{3}c$, fully-relaxed *Pnma*, and *Pnma* with antipolar displacements removed, indicating comparable chemical stereoactivity of the Pb^{2+} cation in the three structures.

While without its lone pair cation $CsPbF_3$ would not be ferroelectric, we find that there is also a significant *A*-site contribution to the ferroelectric eigenmode. *Pnma* symmetry prevents the ferroelectric eigenmode of $CsPbF_3$ from optimally coordinating all *A*-site cations of structures in this space group at once. This is not true in space group $R\bar{3}c$: $R\bar{3}c$ symmetry allows a globally-polar displacement pattern to simultaneously satisfy the coordination requirements of all *A*-site cations.

The localization of the Pb^{2+} lone pair requires a polar pattern of anionic displacements, placing lone pair localization and *A*-site optimization in direct competition when rotation pattern $a^-b^+a^-$ is present but not when $a^-a^-a^-$ is present instead. The ground state of $CsPbF_3$ has space group $R3c$ because in that space group the combination of octahedral rotations and ferroelectricity simultaneously satisfy the *A*-site bonding requirements and allow the Pb^{2+} lone pair to localize.

2.6 Author information

*Email: ehs73@cornell.edu (E.H.S.)

*Email: nicole.benedek@austin.utexas.edu (N.A.B.)

2.7 Acknowledgement

E. H. S. and C. J. F. were supported by the DOE-BES under Award No. DE-SC0005032. N. A. B. was supported by The Welch Foundation under Grant No. F-1803. The authors thank P. Shiv Halasyamani, Ram Seshadri, Pat Woodward, and Young-Moo Byun for useful discussions.

2.8 Supporting information

Version and potential information for computational software, phonon band structures and densities of states of $CsPbF_3$ and $CsSrF_3$, comparison of experimental and theoretical $R3c$ $CsPbF_3$ structures, electronic densities of states of polar and non-polar $CsPbF_3$ structures, energetic stabilization associated with the polar mode of $Pm\bar{3}m$ $CsPbF_3$ with and without anionic displacements, and coordinates of relaxed structures from first-principles calculations.

	$CsPbF_3$	$CsPbF_3$
Source	DFT	Experiment [23]
Space group	*R*3*c*	*R*3*c*
a, Å	6.83122	6.84993(6)
b, Å	6.83122	6.84993(6)
c, Å	16.09397	16.1205(1)
Cs z	0.74028	0.7428(5)
Pb z	0.49262	0.49240(3)
F x	0.21274	0.19857(3)
F y	0.30440	0.30063(4)
F z	0.08410	0.08333(4)

Table 2.3: Comparison of the ground state structures of $CsPbF_3$ as found with density functional theory and as reported at 148 K. In *R*3*c* $CsPbF_3$ the Cs and Pb sit at 6*a* Wyckoff sites, for which x and y are fixed at 0; the F sit at 18*b* sites, in which x, y, and z are all free parameters. We have used the hexagonal setting for *R*3*c*. Experimental data for *Pnma* $CsSrF_3$ were unavailable for comparison to our results.

2.9 Supplementary information

2.9.1 Version information

We used: VASP version 5.2; Wannier90 version 1.2; VESTA version 3; Phonopy version 1.9.5. We used VASP potentials: PAW_PBE Cs_sv 08Apr2002; PAW_PBE Pb_d 06Sep2000; PAW_PBE Sr_sv 07Sep2000; PAW_PBE F 08Apr2002.

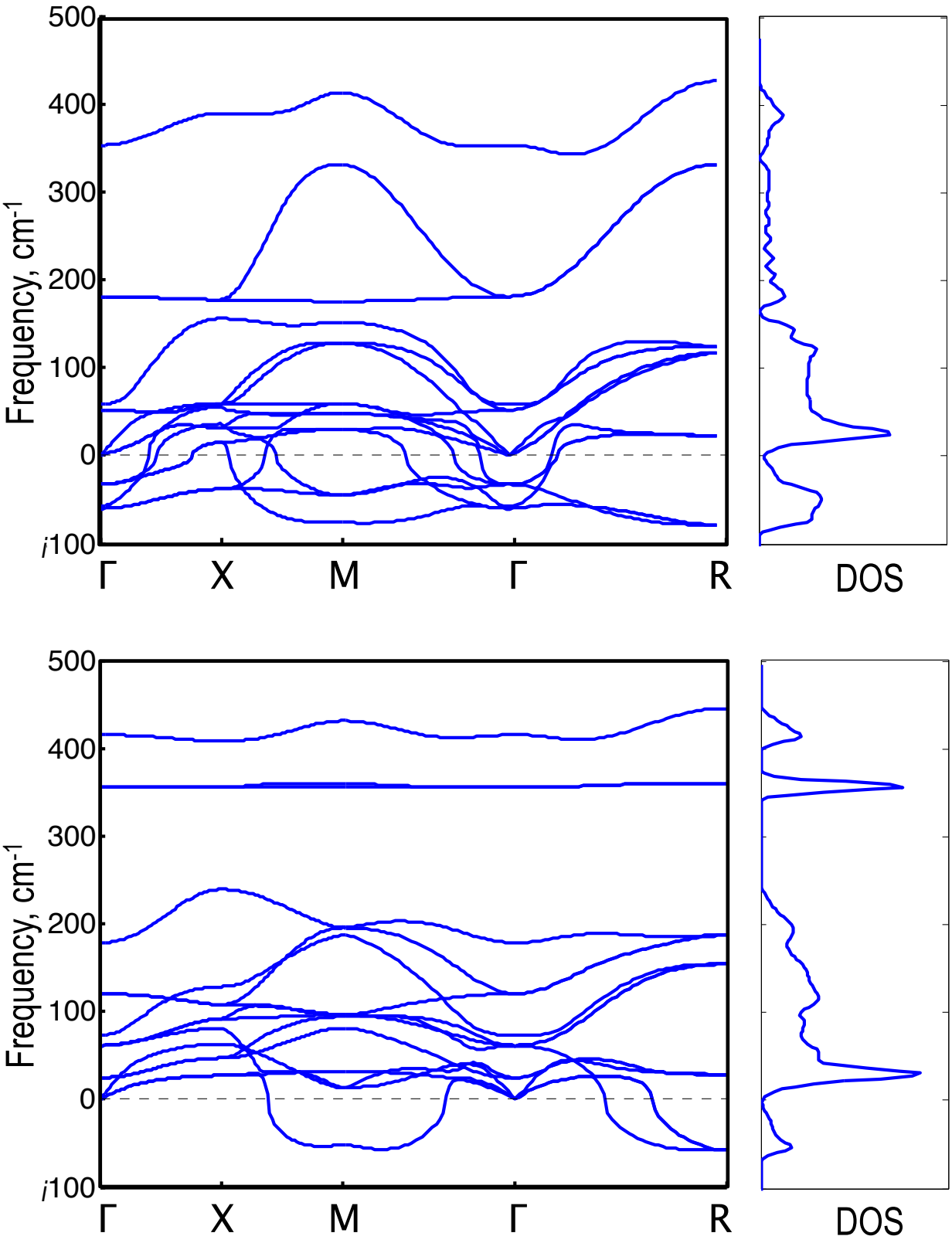

Figure 2.7: Phonon band structure and phonon density of states of $Pm\bar{3}m$ $CsPbF_3$ (top) and $CsSrF_3$ (bottom) calculated using Phonopy [199].

2.9.2 Additional data

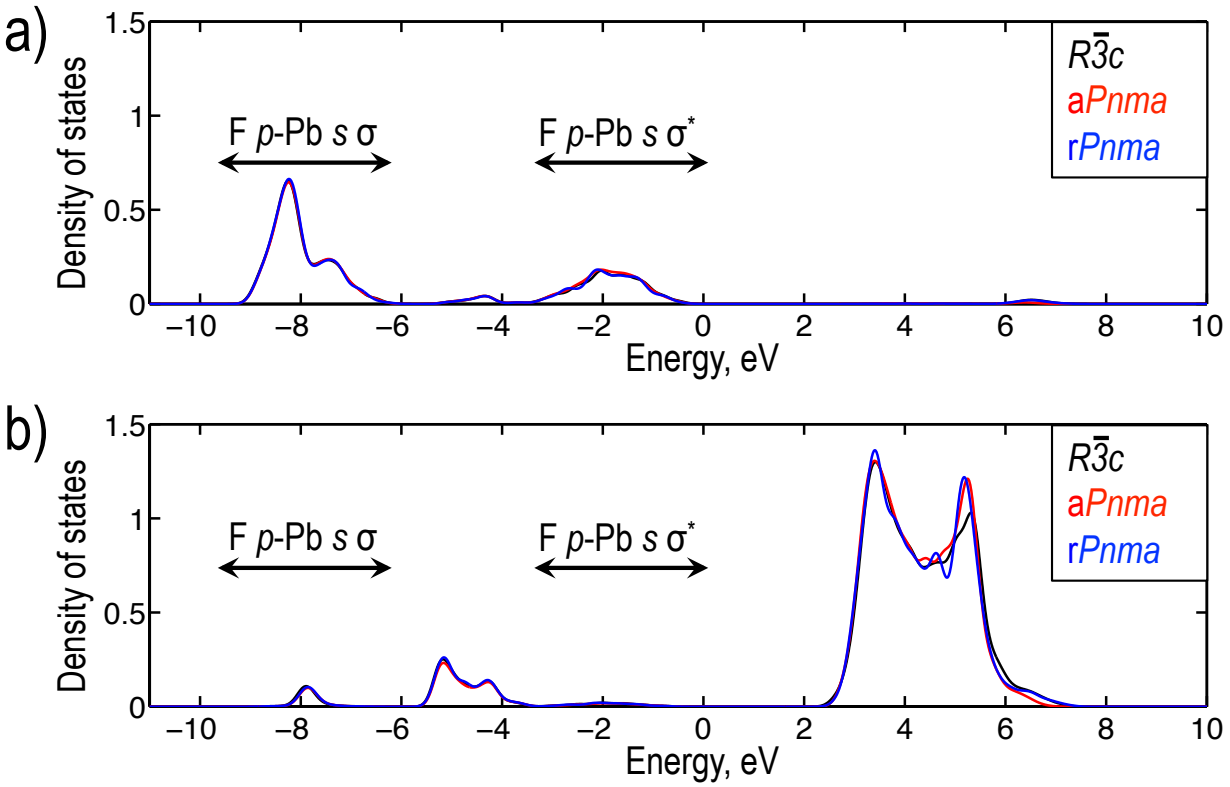

Figure 2.8: a) Pb *s* and b) Pb *p* orbital-projected densities of states of $CsPbF_3$ structures with equilibrium lattice constants, in units of states/(formula unit). For each structure energies are given with respect to their Fermi energy.

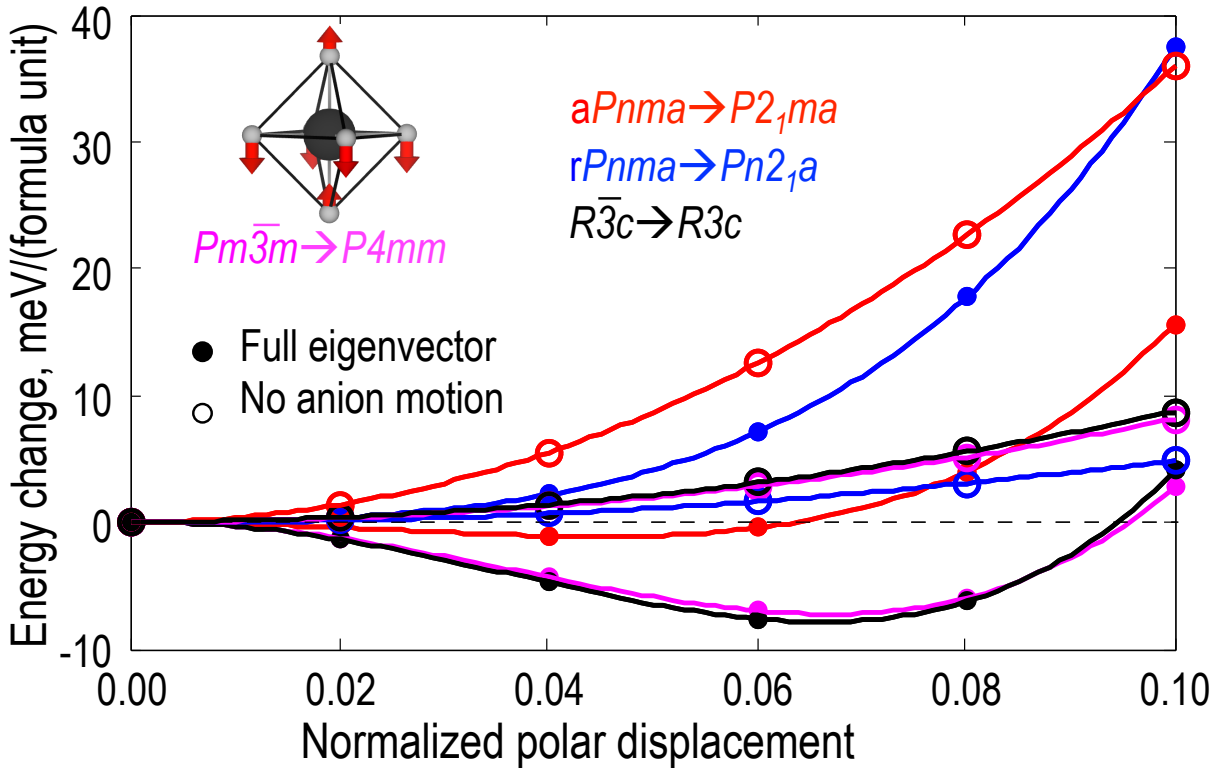

Figure 2.9: Variation of the total energy per formula unit with increasing polar displacement amplitude. For a full description of how this figure was generated, see the caption of Figure 2.5 in the main text. Inset: manner in which the softest polar force constant matrix eigenvector of $Pm\bar{3}m$ $CsPbF_3$ distorts the PbF_6 octahedra. Octahedron is oriented such that motion of the Cs^+ cations (not shown) is towards the top of the page.

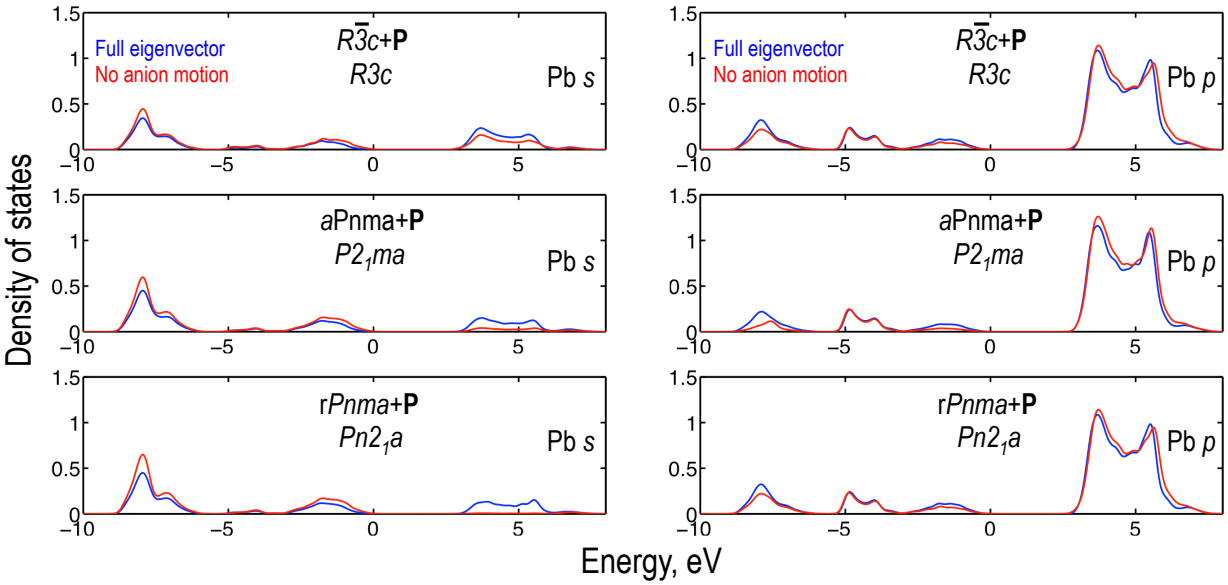

Figure 2.10: Pb *s* (left) and Pb *p* (right) orbital-projected densities of states of polar subgroups of fully-relaxed $R\bar{3}c$ (top) a*Pnma* (middle), and r*Pnma* (bottom) $CsPbF_3$. Structures are made in the same manner as described in the caption of Figure 2.5 in the main text but with the amplitude of the full polar force constant matrix eigenvector set to $0.06a$ per formula unit, where a is the $Pm\bar{3}m$ lattice constant. Densities of states are presented in units of states/(formula unit). Energies are given with respect to the Fermi energy of the polar structure with anionic displacements included.

2.9.3 Relevant structures

See Table 2.3 for comparison of experimental and computed $R3c$ ground state structures of $CsPbF_3$.

Atom	x	y	z
Cs ($1a$)	0	0	0
Pb ($1b$)	0.5	0.5	0.5
F ($3c$)	0	0.5	0.5

Table 2.4: Structure of fully-relaxed $Pm\bar{3}m$ $CsPbF_3$. a=4.80652 Å.

Atom	x	y	z
Cs (6a)	0	0	0.25
Pb (6b)	0	0	0
F (18e)	0.44072	0	0.25

Table 2.5: Structure of fully-relaxed $R\bar{3}c$ $CsPbF_3$. a=6.80864 Å, c=16.30620 Å. Hexagonal settings are used.

Atom	x	y	z
Cs (4c)	0.02509	0.25	0.49418
Pb (4a)	0	0	0
F (8d)	0.72014	-0.03444	0.78003
F (4c)	-0.01642	0.25	0.93567

Table 2.6: Structure of fully-relaxed *Pnma* $CsPbF_3$ (referred to as r*Pnma* in the main text). a=6.76261 Å, b=9.54286 Å, c=6.75431 Å.

Atom	x	y	z
Cs (4c)	0	0.25	0.5
Pb (4a)	0	0	0
F (8d)	0.72005	-0.03330	0.77995
F (4c)	0	0.25	0.93340

Table 2.7: Structure of *Pnma* $CsPbF_3$ with antipolar displacements manually removed (referred to as a*Pnma* in the main text). a=6.76261 Å, b=9.54286 Å, c=6.75431 Å.

Atom	x	y	z
Cs (4c)	-0.01899	0.25	0.50505
Sr (4a)	0	0	0
F (8d)	0.72616	-0.03214	0.77376
F (4c)	-0.01264	0.25	0.93978

Table 2.8: Structure of fully-relaxed *Pnma* $CsSrF_3$. a=6.67564 Å, b=9.42889 Å, c=6.69174 Å.

CHAPTER 3

EXPLOITING KINETICS AND THERMODYNAMICS TO GROW PHASE-PURE COMPLEX OXIDES BY MOLECULAR-BEAM EPITAXY UNDER CONTINUOUS CODEPOSITION

Manuscript accepted to *Phys. Rev. Mater.* as: Smith, Eva H.; Ihlefeld, Jon F.; Heikes, Colin A.; Paik, Hanjong; Nie, Yuefeng; Adamo, Carolina; Heeg, Tassilo; Liu, Zi-Kui; and Schlom, Darrell G. **2017** A few minor changes have been made.

3.1 Abstract

We report the growth of $PbTiO_3$ thin films by molecular-beam epitaxy utilizing continuous codeposition. Contrary to what would be expected from thermodynamics, whether the resulting film is single-phase $PbTiO_3$ or not at a particular temperature depends strongly on the film growth rate and the incident fluxes of all species, including titanium. We develop a simple theory for the kinetics of lead oxidation on the growing film surface and find that it qualitatively explains the manner in which the adsorption-controlled growth window of $PbTiO_3$ depends on lead flux, oxidant flux, and titanium flux. We successfully apply the kinetic theory to the dependence of the growth of $BiFeO_3$ on oxidant type and surmise that the theory may be generally applicable to the adsorption-controlled growth of complex oxides by MBE.

3.2 Introduction

Reactive molecular-beam epitaxy (MBE) is unique in its ability to grow high-quality films with atomically-sharp interfaces and high crystalline quality, including (and especially)

materials that do not exist in nature [173]. Component elements are generally deposited on a substrate starting from single-element sources as low-energy molecular beams; multicomponent materials, including heterostructures, may be deposited layer by layer. The layer-by-layer growth regime gives the grower a high degree of control, with film composition and structure being directed by the user with atomic layer precision. The ability to deposit precise monolayers via shuttering of the molecular beams depends directly on user knowledge of source fluxes, which may vary from day to day or even from hour to hour. Thus, the sensitivity of crystal structure and composition to grower input is both a strength and potential challenge of this growth technique; an uncontrolled flexible growth parameter causes chaos.

In contrast to shuttered growth, adsorption-controlled growth leverages thermodynamics to ensure phase purity. Such automatic composition control is key to the growth of compound semiconductors by MBE [13, 39, 40, 41, 62, 75, 82, 177, 201, 202]. Within a particular range of temperatures and pressures (the so-called adsorption-controlled growth window), one component of a multicomponent material has a sticking coefficient that depends strongly on surface composition. Within this growth window, the volatile species will only stick to the growing film surface and be incorporated into the film bulk if the result is the single-phase, multicomponent material of interest; any excess of the volatile material beyond the single-phase region will not stick or enter the film. Complex oxides that have been grown within the adsorption-controlled growth regime by molecular-beam epitaxy include $PbTiO_3$ [165, 166, 191, 192], $Bi_2Sr_2CuO_y$ [131], $Bi_4Ti_3O_{12}$ [132, 193], $BiFeO_3$ [92, 93, 94, 102], EuO [204], $SrTiO_3$ [98], $BiMnO_3$ [117], $LuFe_2O_4$ [31], $SrRuO_3$ [144, 178], $GdTiO_3$ [134], $BiVO_4$ [188], Ba_2IrO_4 [203], $BaTiO_3$ [127], $SrIrO_3$ [148], Sr_2IrO_4 [103, 148], $LaVO_3$ [219], Ba_2RuO_4 [9, 34], Sr_2RuO_4 [9, 34], $CaTiO_3$ [79], $(La,Sr)VO_3$ [27], $BaSnO_3$ [152, 153, 160], $CaRuO_3$ [123], Ca_2RuO_4 [145], and $PbZrO_3$ [210].

In contrast to what is suggested by thermodynamic theory, however, a significant

number of these multicomponent oxides are not actually grown by continuous codeposition [92, 93, 94, 102, 117, 131, 132, 165, 166, 188, 191, 192, 193]. Rather, in these cases the non-volatile species is supplied in monolayer doses, with pauses between the doses in which only the volatile species is supplied. When the materials are continuously codeposited, the complex oxide does not form as a single phase [165, 166, 192, 193]. The apparent requirement for the supply of the non-volatile species to be modulated is not explained within the thermodynamic theory, and furthermore confers clear disadvantages, such as substantially increasing growth times (as elements are deposited in series rather than parallel) and requiring calibration of the dose times. Thus, the advantages of adsorption-controlled growth are not, in general, fully utilized. The importance of oxidation kinetics has been conjectured for the adsorption-controlled growth of some oxides such as $PbTiO_3$ [165, 166, 191, 192] and MgO [124] but not fully or generally explored. Of the complex oxides that are grown by continuous codeposition, some circumvent possible oxidation challenges by employing oxidized precursors rather than elemental source materials plus an oxidant [27, 79, 127, 134, 153, 160, 219].

Using as a model system the growth of $PbTiO_3$ by continuous codeposition of lead, titanium, and distilled ozone, we measure the dependence of the adsorption-controlled growth window on flux of both the volatile and non-volatile species. We establish a simple kinetic model for adsorption-controlled growth that complements the existing thermodynamic theory, and delineate the factors controlling the kinetic growth window. We find that besides qualitatively explaining the dependence of the adsorption-controlled growth window of $PbTiO_3$ on flux of both volatile and non-volatile species, the kinetic theory also may be used to explain the dependence of the growth window of $BiFeO_3$ on oxidant mixture. We find that oxidation kinetics are critical to growing phase-pure materials by this method.

3.3 Methods

3.3.1 Growth and analysis of $PbTiO_3$

We grew thin films of $PbTiO_3$ by reactive MBE in a Veeco GEN 10 system using distilled ozone (approximately 80 mol% O_3) as an oxidant and elemental lead and titanium as source materials. We used lead fluxes from 30 to 60 $\times$ 10^{13} atoms cm^{-2} s^{-1} and titanium fluxes from 1 to 4.5 $\times$ 10^{13} atoms cm^{-2} s^{-1}, resulting in beam equivalent pressures [47] of 1 to 2 $\times$ 10^{-6} Torr and 5 to 20 $\times 10^{-8}$ Torr, respectively. Lead was supplied with an effusion cell and titanium was supplied with a Ti-Ball^{TM} [7, 80, 190, 213]. During all $PbTiO_3$ growths, lead, ozone, and titanium were continuously codeposited. Temperature was monitored using an optical pyrometer and the background chamber pressure was monitored with an ion gauge. We found that opening (closing) the titanium shutter to initiate (halt) growth caused the substrate temperature to increase (decrease) by 20°C and the chamber background pressure to drop (rise) by 10%. We believe this is due to low temperature of the substrate in comparison to that of the titanium source, which is near 1550°C in the latter case [80, 190, 213], and titanium acting as a getter pump with a large radiating area [80]. We report temperatures and pressures during growth, with both lead and titanium shutters open. All $PbTiO_3$ films were grown using (001)-oriented TiO_2-terminated $SrTiO_3$ substrates [110] with a miscut of less than 0.2°.

The crystalline phases present in the films and their orientations were monitored *in situ* with reflection high-energy electron diffraction (RHEED) along the <100> and <110> azimuths and *ex situ* with four-circle X-ray diffraction (XRD) on a PANalytical X'Pert PRO using Cu $K\alpha_1$ radiation monochromated with a four-bounce Ge 220 monochromater.

3.3.2 Growth and analysis of $BiFeO_3$

We grew thin films of $BiFeO_3$ by reactive MBE in a Veeco 930 system described elsewhere [191] using as an oxidant either 9 mol% ozone directly out of the ozone generator or 90 mol% ozone following distillation, and elemental bismuth and iron as source materials. Both iron and bismuth were supplied with effusion cells. $BiFeO_3$ was grown in an adsorption-controlled regime, as described previously [92, 93, 94], under a constant bismuth flux of 1.4×10^{14} atoms cm^{-2} s^{-1}. Growth was controlled by supplying monolayer doses of iron at a flux of 2×10^{13} atoms cm^{-2} s^{-1} and allowing equivalent bismuth-only time intervals between iron doses. Unlike the $PbTiO_3$ thin films, the $BiFeO_3$ thin films were not grown by continuous codeposition. The substrate temperature during growth was monitored *in situ* via band edge spectroscopy of the $SrTiO_3$ substrate [85, 101]. All $BiFeO_3$ films were grown on (001)-oriented TiO_2-terminated $SrTiO_3$ substrates [110].

The growth surface and phase assemblage were monitored *in situ* with RHEED along the substrate <110> azimuth and verified *ex situ* using XRD.

3.4 Results

Figure 3.1 shows the expected dependance [16, 192] of the adsorption-controlled growth window of $PbTiO_3$ on temperature and pressure as predicted from thermodynamics. The themodynamic growth window is a region in gas pressure and substrate temperature; because experimental ozone pressures are many orders of magnitude greater than what is required thermodynamically to oxidize lead, the gas pressure relevant to the thermodynamics of $PbTiO_3$ formation is the partial pressure of PbO gas. When the gas pressure is too high or the substrate temperature too low, solid PbO is expected to accumulate on the film surface. When the gas pressure is too low or the substrate temperature too high,

all PbO is expected to desorb and not be incorporated into the growing film, resulting in the film being just TiO_2. We note that the width of the window (in temperature) has only a very weak dependence on gas pressure (increasing pressure from 1×10^{-8} Torr to 1×10^{-7} Torr widens the window from 105°C to 111°C, a change of only 6%) and that there is no explicit dependence on titanium flux of the growth window at all [192]. Indeed, thermodynamics is all about equilibrium and not about growth.

The RHEED and XRD patterns we observed corresponding to PbO excess, pyrochlore $Pb_2Ti_2O_6$, and TiO_2 excess, as well as phase-pure $PbTiO_3$, are shown in Fig. 3.1. We discuss the secondary phases we observe in the Supplementary Information.

Next, we characterized the conditions under which the continuous codeposition of lead, titanium, and ozone will yield each of the three sets of product described in Fig. 3.1(b). In this way we delineate our experimental (rather than theoretical) growth window. In agreement with previous reports, we observed that when the titanium flux is relatively high in comparison with the lead flux (Pb:Ti=7:1 in this work; between 2:1 and 5:1 in previous reports), phase-pure $PbTiO_3$ cannot be grown by continuous codeposition of the constituents [166, 192, 193]. When we increase the Pb:Ti ratio by decreasing the titanium flux, however, we are able to grow $PbTiO_3$ by continuous codeposition, as shown in Fig. 3.2(a). This finding – that the adsorption-controlled growth window of $PbTiO_3$ depends strongly on titanium flux – cannot be explained by the thermodynamic window shown in Fig. 3.1(a). Because the growth rate of the $PbTiO_3$ (within the growth window) is controlled by the titanium flux, the dependence on the titanium flux may equivalently be considered a dependence on growth rate.

To further understand the role played by kinetics in the growth of $PbTiO_3$ by continuous codeposition, we also measure the dependence on the lead flux and oxidant flux of the phases grown. While the width of the thermodynamic growth window shown in Fig. 3.1(a) is only very weakly dependent upon PbO gas pressure, we observe a significant

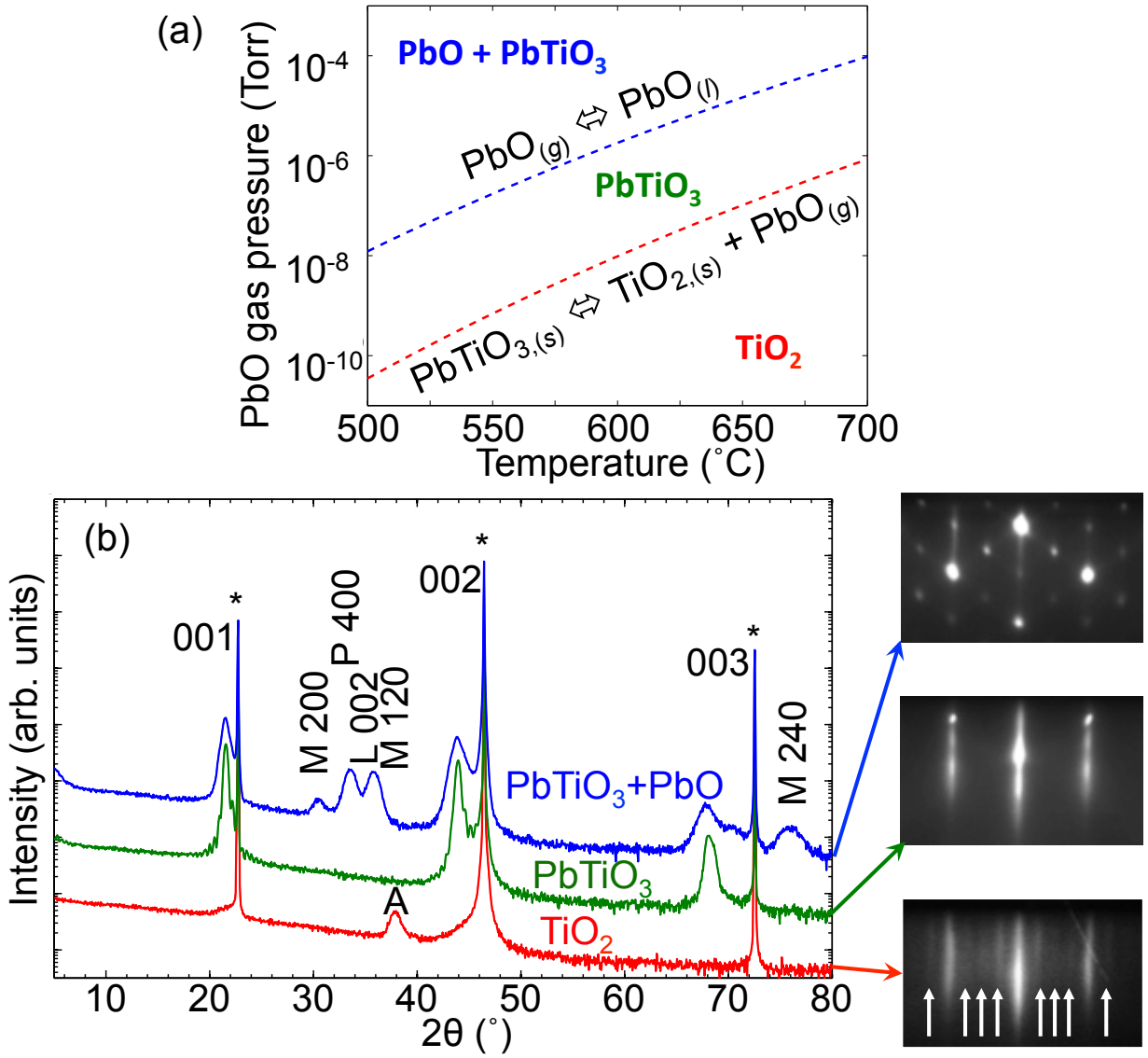

Figure 3.1: (a) The adsorption-controlled growth window of $PbTiO_3$ as a function of PbO gas pressure and substrate temperature, as calculated from thermodynamics [16, 192]. (b) Indexed x-ray diffraction patterns and RHEED images taken along the substrate <100> azimuth of films grown within each of the three regions of condensed phases: (i) PbO + $PbTiO_3$; (ii) $PbTiO_3$ only; and (iii) TiO_2. Arrows have been added to aid the eye in the TiO_2-phase RHEED image. Impurities are labeled as follows: A=anatase TiO_2; M=massicot PbO; L=litharge PbO; P=pyrochlore $Pb_2Ti_2O_6$. See Supplementary Information for a full list of growth conditions and a description of secondary phases appearing in part (b).

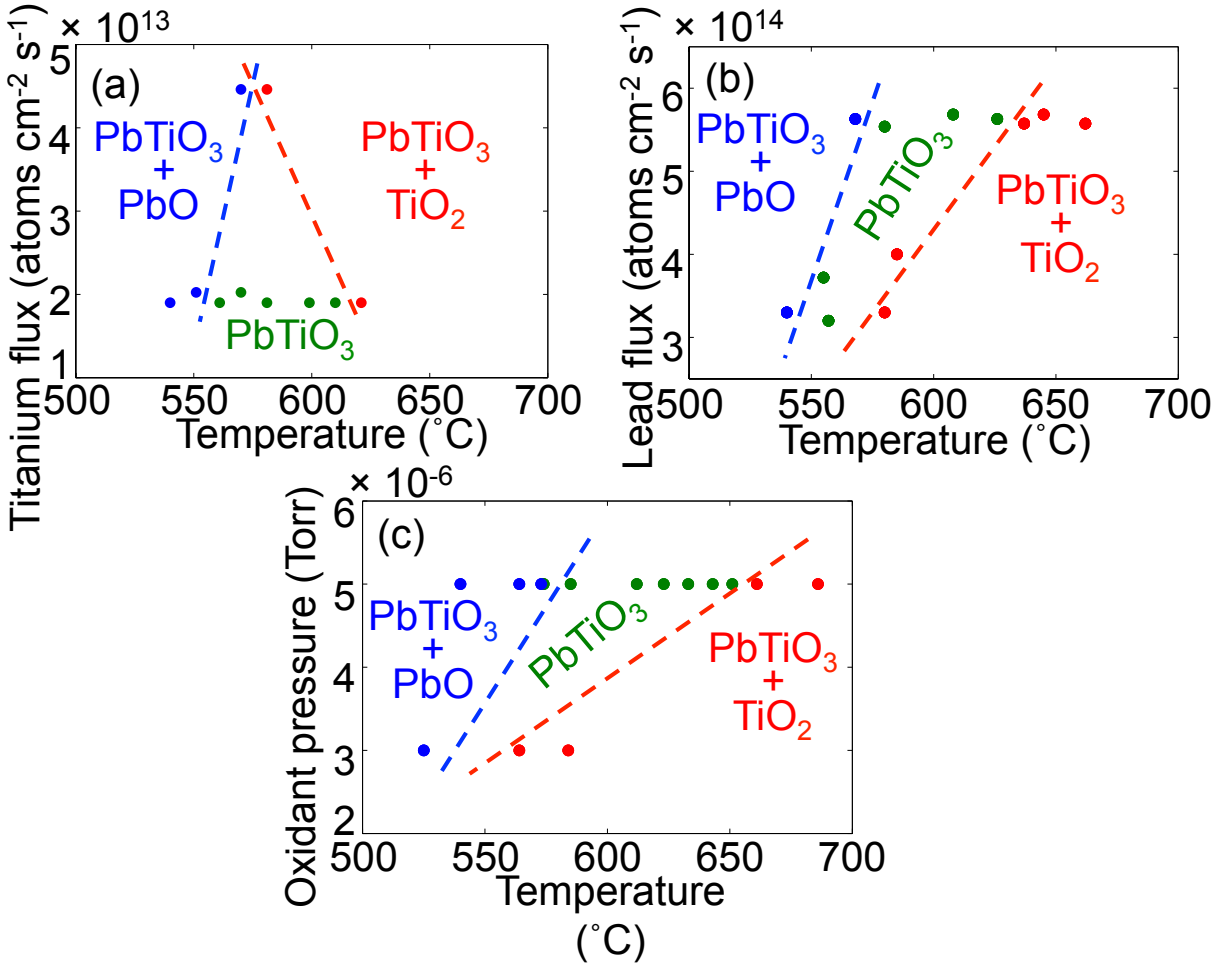

Figure 3.2: Dependence of observed film phase as a function of titanium flux, lead flux, or oxidant pressure. Only one variable (source flux or oxidant pressure) was varied, in addition to temperature, at a time. Phases observed when (a) oxidant background pressure and lead flux were fixed; (b) oxidant background pressure and titanium flux were fixed; (c) titanium flux and lead flux were fixed. See Supplementary Information for a full list of growth conditions.

dependence of the width of the experimental growth window on the lead flux, shown in Fig. 3.2(b). Furthermore, while we supply many orders of magnitude more ozone than the amount necessary to thermodynamically favor oxidation of lead into PbO at growth temperature [16, 192], we see in Fig. 3.2(c) that the growth window is highly sensitive to chamber background pressure as well.

The dependence of the observed growth window on ozone flux and on the lead flux

is the inverse of that observed for the titanium flux: increasing either the ozone flux or the lead flux has the effect of widening the growth window. Based on the thermodynamic theory, changing the lead or ozone flux should shift the growth window to higher or lower temperatures without significantly altering its width. In the next section we develop a simple theory of the role of kinetics of lead oxidation in the growth of $PbTiO_3$ and see that it may be used to qualitatively explain these results. We then test this theory on a completely different system: the growth of $BiFeO_3$ by adsorption-controlled MBE when the iron is supplied in sequential monolayer doses (shuttered) rather than being continuously deposited (as are all sources in our growths of $PbTiO_3$). We find that while thermodynamics cannot explain the dependence of the $BiFeO_3$ growth window on oxidant type [molecular oxygen (O_2) versus ozone (O_3)], the observed dependence is in agreement with the kinetic theory.

3.5 Discussion: Role of kinetics in adsorption-controlled growth

3.5.1 Formulation of the kinetic model using $PbTiO_3$ as an example

We established in the previous section that, in contrast to what is expected from thermodynamic theory, the window in temperature for the adsorption-controlled growth of $PbTiO_3$ depends strongly on lead flux, titanium flux, and oxidant pressure. During growth of $PbTiO_3$ by adsorption-controlled MBE, the majority of PbO is formed on the film surface [192]; in this section we apply the Langmuir-Hinshelwood model [51, 126] of bimolecular, surface-catalyzed reactions to the formation of PbO from lead and oxygen adsorbed on the film surface and find that this model suitably explains the dependence of the growth window of $PbTiO_3$ on lead, oxidant, and titanium flux. The Langmuir-Hinshelwood model, an extension of the Langmuir adsorption isotherm, has been used

successfully to explain the rate data of surface-catalyzed reactions such as oxidation of CO by O_2 on Pt(111) and Rh(111); decomposition of ammonia to N_2 and H_2 on Pt(111), Rh(111), or Fe(111); and the water shift reaction on platinum; as well as many others [126].

We consider the formation of PbO on the growing film surface by the reaction of an adsorbed lead atom and an adsorbed oxygen atom:

$$Pb_{(ad)} + O_{(ad)} \xrightarrow{k_{3.1}} PbO_{(ad)}. \tag{3.1}$$

$Pb_{(ad)}$ and $O_{(ad)}$ are both formed on the surface when gas-phase atoms strike the surface; we assume that the film surface is at steady state during growth by continuous codeposition. We also assume that the adsorption and desorption of lead and oxygen atoms are very rapid in comparison with the reaction in Eq. (3.1), and that Eq. (3.1) is thus the rate-limiting step in the formation of PbO on the film surface, though we will return to this latter assumption at the end of this section. Within the Langmuir-Hinshelwood model, the rate of PbO formation will then be [51, 126]

$$r_{PbO} = k_{3.1}[Pb_{(ad)}][O_{(ad)}], \tag{3.2}$$

where $[Pb_{(ad)}]$ and $[O_{(ad)}]$ are the concentrations of the adsorbed species in molecules cm^{-2}. Later on we will discuss the factors that determine $[Pb_{(ad)}]$ and $[O_{(ad)}]$.

After PbO is formed on the surface, it may either remain adsorbed or evaporate. Depending on temperature, $PbO_{(g)}$ gas pressure, and surface composition, the following equilibrium will either move towards reactants (high pressure, low temperature) or products (low pressure, high temperature):

$$PbO_{(ad)} \underset{k_{-3.3}}{\overset{k_{3.3}}{\rightleftharpoons}} PbO_{(g)} + 2*, \tag{3.3}$$

where * denotes unoccupied surface sites. The particular value of the equilibrium constant $K_{PbO} = k_{3.3}/k_{-3.3} = [PbO_{(g)}]/[PbO_{(ad)}]$ at a given temperature and pressure may be found with thermodynamics; K_{PbO} determines the thermodynamic growth window.

The chemical reactions involving titanium and oxygen atoms are:

$$\mathrm{Ti}_{(g)} + * \underset{k_{-3.4}}{\overset{k_{3.4}}{\rightleftharpoons}} \mathrm{Ti}_{(ad)} \tag{3.4}$$

and

$$\mathrm{Ti}_{(ad)} + 2\mathrm{O}_{(ad)} \underset{k_{-3.5}}{\overset{k_{3.5}}{\rightleftharpoons}} \mathrm{TiO}_{2,(ad)}. \tag{3.5}$$

Based on the observations that (i) titanium exhibits unity sticking [192], and thus Eq. (3.4) is zeroth-order in concentration of surface sites [*]; (ii) titanium will be oxidized even with much lower oxidant pressure than is present in our system, and thus Eq. (3.5) is zeroth-order in oxidant pressure and in $[\mathrm{O}_{(ad)}]$; and (iii) the above two reactions are irreversible under our growth conditions; we find that the rate of TiO_2 formation is just the titanium flux, Φ_{Ti}:

$$r_{\mathrm{TiO}_2} = k_{3.4}[\mathrm{Ti}_{(g)}] = \Phi_{\mathrm{Ti}}. \tag{3.6}$$

$PbTiO_3$ formation is given by

$$\mathrm{TiO}_{2,(ad)} + \mathrm{PbO}_{(ad)} \xrightarrow{k_{3.7}} \mathrm{PbTiO}_{3,(ad)}. \tag{3.7}$$

For $PbTiO_3$ to be formed as a single phase without excess TiO_2 accumulation in the film, r_{PbO} must equal or exceed r_{TiO_2}. When this is true and conditions are within the thermodynamic growth window, the rate of $PbTiO_3$ formation $r_{\mathrm{PbTiO}_3} = r_{\mathrm{TiO}_2}$. On the other hand, if $r_{\mathrm{PbO}} < r_{\mathrm{TiO}_2}$ then $PbTiO_3$ will not form as a phase-pure material; rather, deposition of TiO_2 will "outrun" formation of PbO and the excess TiO_2 will accumulate as a secondary phase. It is possible for this to occur within the thermodynamic growth window; we would consider such growth conditions to be within the thermodynamic growth window but outside the *kinetic* growth window.

We delineate the kinetic growth window, within which $PbTiO_3$ may grow because $r_{\mathrm{PbO}} \geq r_{\mathrm{TiO}_2}$, by substituting in the preceeding inequality Eqs. (3.2) and (3.6):

$$k_{3.1}[\mathrm{Pb}_{(ad)}][\mathrm{O}_{ad}] \geq \Phi_{\mathrm{Ti}}. \tag{3.8}$$

We immediately see that for higher titanium fluxes, more lead and oxygen must be present on the surface in order for PbO formation to keep up with TiO_2 formation. This explains the result in Fig. 3.2(a), that increasing the titanium flux while holding other conditions constant has the effect of closing the growth window and preventing growth of phase-pure $PbTiO_3$.

We describe the relationship between $[Pb_{(ad)}]$ and the beam equivalent gas pressure $[Pb_{(g)}]$ using thermodynamics [16] and the relationship between the lead flux Φ_{Pb} and $[Pb_{(g)}]$ using the kinetic theory of gases [47]. Combining these relationships, $[Pb_{(ad)}]$ relates to the lead flux as

$$[Pb_{(ad)}] \propto \Phi_{Pb} e^{-\Delta H_{Pb_{(g)} \rightarrow Pb_{(l)}}/k_B T}. \tag{3.9}$$

At MBE-amenable chamber pressures and substrate temperatures, the concentration of adsorbed, possibly-activated oxygen atoms available for oxidizing the film appears to be a linear function of ozone flux [24, 115, 171, 175, 176]. See the Supplementary Information for a fuller discussion of these relationships.

Substituting in to Eq. (3.15) the relationship between lead flux Φ_{Pb} and $[Pb_{(ad)}]$ described in Eq. (3.14) and assuming a linear relationship between ozone flux Φ_{O_3} and $[O_{(ad)}]$, we may summarize the kinetic growth window as

$$k\Phi_{Pb} e^{-\Delta H_{Pb_{(g)} \rightarrow Pb_{(l)}}/k_B T} \Phi_{O_3} \geq \Phi_{Ti}, \tag{3.10}$$

for k a proportionality constant; or, in terms of a flux ratio,

$$\frac{\Phi_{Pb}\Phi_{O_3}}{\Phi_{Ti}} \geq \kappa e^{+\Delta H_{Pb_{(g)} \rightarrow Pb_{(l)}}/k_B T}. \tag{3.11}$$

The term on the right side of Eq. (3.11) will *increase* exponentially with increasing temperature: at higher substrate temperatures larger flux ratios will be required to grow $PbTiO_3$ by continuous codeposition. At constant temperature, this flux ratio describes the effect on the kinetic growth window of changing the lead flux, ozone flux, or titanium flux ob-

served experimentally in Fig. 3.2: increasing titanium flux closes the growth window, while increasing the lead or ozone flux opens it.

This kinetic growth window theory complements, rather than replaces, the thermodynamic growth window theory. Growth conditions must be within both windows for $PbTiO_3$ to be grown as a single phase by continuous codeposition. At high titanium flux, it is possible to be within the thermodynamic growth window (any PbO that forms is incorporated into the film at no more than a 1:1 ratio with TiO_2) but outside the kinetic growth window (PbO formation cannot keep up with TiO_2 formation, and excess TiO_2 accumulates as a secondary phase). As noted in the previous paragraph, at larger flux ratios $\Phi_{Pb}\Phi_{O_3}/\Phi_{Ti}$ the temperature at which TiO_2 formation outruns PbO formation is higher; given the independence of the thermodynamic growth window on titanium flux, increasing the flux ratio has the effect of widening the overall growth window. Increasing the lead flux and titanium flux by equal measure, on the other hand, which does not alter the flux ratio, has the effect of shifting the growth window to higher temperatures while leaving its width unchanged.

The fact that increasing ozone flux is observed experimentally in Fig. 3.2 to have a larger effect on the width of the growth window than does increasing the lead flux brings into question our earlier approximation that the rate-limiting step in the formation of PbO is the collision of an adsorbed lead atom and an adsorbed oxygen atom, Eq. (3.1). If $[Pb_{(ad)}] \gg [O_{(ad)}]$, then the rate of PbO formation on the surface may be less than first order in $[Pb_{(ad)}]$, and Φ_{Pb} in Eqs. (3.10) and (3.11) could be replaced by Φ_{Pb}^{x} for $0 < x < 1$. Such a factor could help explain why such extraordinary excesses of lead relative to titanium are required. Further increases to ozone flux at the film surface might permit reduction of the Pb:Ti flux ratio.

That the kinetic growth window of $PbTiO_3$ may be more dependent upon the ozone flux than the lead flux might explain our success in growing $PbTiO_3$ by continuously

codeposited MBE. In addition to our use of distilled ozone as an oxidant, our ozone delivery tube is rather close to the 10 mm × 10 mm substrate (5.1 cm from the end of the ozone delivery tube to the substrate center at a 40° angle of incidence). If ozone flux were more rate-limiting to the kinetics of lead oxidation than lead flux, it would follow that maximizing ozone flux at the substrate would be key to the growth of $PbTiO_3$ by continuous codeposition at reasonable growth rates. In addition to $PbTiO_3$, another complex oxide, $CaRuO_3$, has been grown for the first time by continuous codeposition of source elements in our modified chamber [123], and we have grown $BiFeO_3$ by continuous codeposition [84, 146] in a chamber with a similar ozone delivery tube geometry, though in the next section we employ shuttering in our growth of $BiFeO_3$.

3.5.2 Application of model to growth of $BiFeO_3$

To test the generality of the importance of oxidation kinetics to adsorption-controlled growth, we turn our consideration to another system: the adsorption-controlled growth of $BiFeO_3$ by reactive MBE from metallic bismuth, iron, and oxidant [molecular oxygen (O_2) and ozone (O_3]). For this portion of our experiments, we continuously supplied bismuth and oxidant, while supplying monolayer doses of iron interspersed with pauses. This "shuttered" growth technique is how many complex oxides are grown by adsorption-controlled MBE [92, 93, 94, 102, 117, 131, 132, 165, 166, 188, 191, 192, 193].

$BiFeO_3$ may be grown by MBE using a relatively low quantity of ozone in comparison to that required to grow $PbTiO_3$. At a 5:1 Pb:Ti ratio, distilled ozone at a background pressure of 1×10^{-5} Torr is necessary to oxidize lead even when the titanium is shuttered [192]; however, at a 7:1 Bi:Fe ratio, we find that $BiFeO_3$ may be grown when the iron is shuttered at 1×10^{-6} Torr of oxidant using either distilled ozone (90% in this study) or ozone at the concentration produced by the ozone generator, *i.e.*, 9% O_3 + 91% O_2. Thus, con-

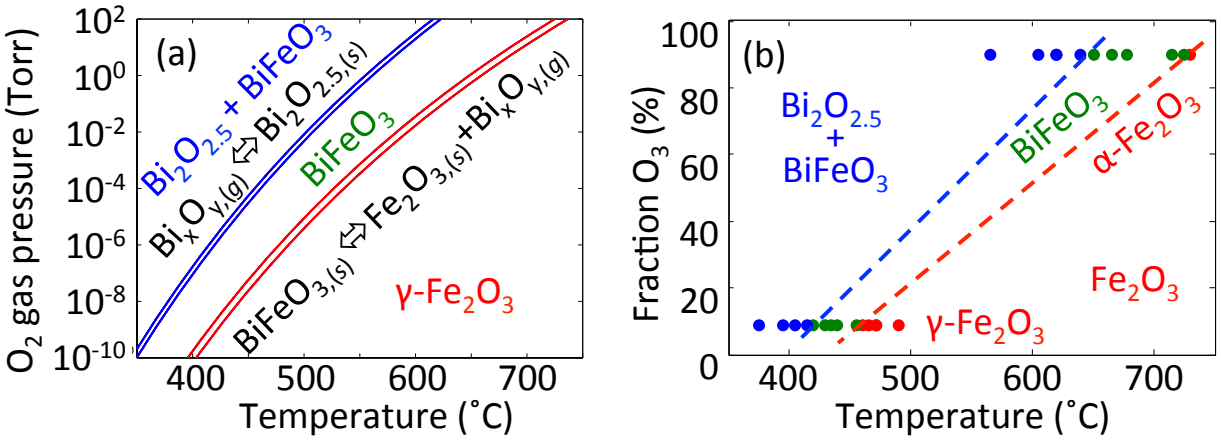

Figure 3.3: (a) Adsorption-controlled growth window of $BiFeO_3$ as a function of molecular oxygen pressure as calculated from thermodynamics, after Ihlefeld and co-workers [93]. (b) Dependence of observed phase as a function of fraction ozone in the oxidant blend. We note that different phases of Fe_2O_3 appear as secondary phases outside the growth window at the two different oxidant mixtures. Ozone is 250× more active in oxidizing bismuth than diatomic oxygen in the process chamber in which we grew $BiFeO_3$. See Supplementary Information for a full list of growth conditions and for our measurements of ozone activity.

sideration of $BiFeO_3$ allows us to study the effect of different oxidant mixtures. Similar to $PbTiO_3$, however, the width of the thermodynamic adsorption-controlled growth window of $BiFeO_3$ (shown in Fig. 3.3(a), after Ihlefeld and co-workers [93]) only shows a very weak dependence on gas pressure. Increasing the oxygen pressure by an order of magnitude, from 1×10^{-7} Torr to 1×10^{-6} Torr, increases the width of the thermodynamic window by only 4°C, an increase of less than 10%. In our chamber ozone has about 250 times the activity of molecular oxygen for the oxidation of bismuth. Similar activity enhancement for ozone over molecular oxygen has been observed for the oxidation of copper as well [175]. Replacing oxygen with ozone in Fig. 3.3(a) would be expected to shift the growth window to lower pressures without otherwise changing its form. See Supplementary Information for our measurements of ozone activity.

We present in Fig. 3.3(b) the observed dependence of the growth window of $BiFeO_3$ on ozone concentration. Using 9% ozone, $Bi_2O_{2.5}$ appears in the RHEED up to 415°C, and

Fe_2O_3 appears at 460°C, giving a window for the growth of $BiFeO_3$ 45°C wide. Using 90% ozone both moves the growth window up by roughly 200°C in substrate temperature, and doubles its width: $Bi_2O_{2.5}$ appears in the RHEED up to 640°C, and Fe_2O_3 appears at 725°C, giving a window for growth of $BiFeO_3$ of 90°C. The shift in the growth window to higher oxygen pressure at higher temperature is expected from thermodynamics, but the increase in the width of the growth window can only be explained by our kinetic model.

The change in phase of Fe_2O_3 that appears as an impurity outside the $BiFeO_3$ growth window, from γ-Fe_2O_3 at low ozone fraction to α-Fe_2O_3 at high ozone fraction, may be attributable to the effect of epitaxial strain combined with thermodynamics. See Supplementary Information.

3.6 Conclusions

We have grown $PbTiO_3$ by MBE using continuous codeposition of all source elements for the first time. We find the successful growth of phase-pure $PbTiO_3$ by this method depends on achieving a sufficient ratio of fluxes $\Phi_{Pb}\Phi_{O_3}/\Phi_{Ti}$, with increasing lead or oxidant flux favoring $PbTiO_3$ growth and increasing titanium flux disfavoring $PbTiO_3$ growth. The thermodynamics of $PbTiO_3$ growth within the adsorption-controlled regime depends on the equilibrium between adsorption and desorption of PbO; we argue that the kinetics of PbO formation on the growing film surface are also of high importance, and present a simple theory that describes it. In conjunction with the existing thermodynamic theory, our kinetic theory qualitatively explains our observed dependence of the growth window on the flux ratio $\Phi_{Pb}\Phi_{O_3}/\Phi_{Ti}$, as well as substrate temperature. We find that this model may also be used to qualitatively explain the dependence of the growth window of $BiFeO_3$ on oxidant mixture.

3.7 Acknowledgements

E.H.S. and D.G.S. acknowledge helpful discussions with Roman Engel-Herbert and support by the National Science Foundation (NSF) MRSEC program (DMR-1420620). This work made use of the Cornell Center for Materials Research (CCMR) Shared Facilities, which are supported through the NSF MRSEC program (DMR-1120296). Substrate preparation was performed in part at the Cornell NanoScale Facility, a member of the National Nanotechnology Coordinated Infrastructure (NNCI), which is supported by the NSF (Grant ECCS-15420819). J.F.I. acknowledges funding from the Office of Naval Research Grant No. N00014-04-1-0426.

3.8 Supplementary information

3.8.1 Secondary phases that appear in the growth of $PbTiO_3$

Below the bottom of the growth window in temperature, we observed a mixture of litharge and massicot PbO, indexed as L and M respectively in Fig. 1 in the main text. At times we also observed, along with peaks corresponding to these PbO phases, a peak in the XRD pattern that we could not index to either phase of PbO or a higher oxidation state oxide of lead; we believe that this peak corresponds a phase described in the literature as a pyrochlore [100]. This phase may be associated with lower temperatures [209, 212]. In the XRD pattern we mark this peak P. Above the top of the growth window in temperature, we exclusively observed TiO_2 in the anatase phase, denoted A. Although the anatase polymorph of TiO_2 is metastable at all temperatures (the stable polymorph is rutile) [16], the favorable lattice match between (001) anatase and the (001) perovskite surface epitaxially stabilizes this metastable TiO_2 polymorph [38, 99].

3.8.2 Growth conditions in figures from main text

Fig. 1: All three x-ray patterns were taken from films grown at a lead flux of 3.1×10^{14} atoms cm^{-1} s^{-1}, a titanium flux of 1.0×10^{13} atoms cm^{-1} s^{-1}, and oxidant background pressure of 5×10^{-6} Torr; the only parameter changed was substrate temperature.

Fig. 2: (a) The oxidant background pressure was fixed at 5×10^{-6} Torr and the lead flux was fixed at 3.1×10^{14} atoms cm^{-1} s^{-1}; (b) the oxidant background pressure was fixed at 5×10^{-6} Torr and the titanium flux was fixed at 1.1×10^{13} atoms cm^{-1} s^{-1}; (c) the lead flux was fixed at 2.4×10^{14} atoms cm^{-1} s^{-1} and the titanium flux was fixed at 2.4×10^{13} atoms cm^{-1} s^{-1}.

Fig. 3: All films were grown with a bismuth flux of 1.4×10^{14} atoms cm^{-1} s^{-1}, an iron flux of 2×10^{13} atoms cm^{-1} s^{-1}, and oxidant background pressure of 1×10^{-6} Torr; the only parameters changed were substrate temperature and oxidant mixture.

3.8.3 Factors controlling concentrations of adsorbed lead and adsorbed oxygen

To understand the dependence on the lead flux and oxidant pressure seen in the main text, Figs. 2(b) and 2(c), we consider the factors controlling the concentrations of adsorbed lead and oxygen, $[Pb_{(ad)}]$ and $[O_{(ad)}]$. To grow $PbTiO_3$ as a single phase we supply at least 15 times more lead than titanium and at least 40 times more ozone than titanium. Thus, the the fraction of lead and oxygen consumed by reaction to PbO is relatively small near the edge of the kinetic growth window, when $r_{PbO} \approx r_{TiO_2}$, and we model the lead and oxygen adsorption/desorption assuming that they are independent of each other and of the titanium flux. We also assume low surface coverage of each, though we discuss

this latter assumption in the main text. We do not explicitly consider the true reaction mechanism or the density of surface sites of type suitable for these particular reactions; we do note, however, that all $PbTiO_3$ grown within this study was grown on the same type of substrate, prepared in the same way, with a miscut angle between 0° and 0.2°, suggesting that there may be comparable densities of the sites of interest.

Our growth temperatures are well above the equilibrium sticking temperature of metallic Pb^0 at our chamber pressure; lead only resides briefly on the surface, at equilibrium with empty surface sites $*$:

$$Pb_{(g)} + * \underset{k_{-3.12}}{\overset{k_{3.12}}{\rightleftharpoons}} Pb_{(ad)}. \tag{3.12}$$

The concentration of adsorbed lead atoms $[Pb_{(ad)}]$ may be found from the equilibrium constant of this reaction $K_{Pb}=k_{3.12}/k_{-3.12}=[Pb_{(ad)}]/[Pb_{(g)}]$. The equilibrium constant itself is related to the Gibbs energy of condensation of a lead atom onto a surface:

$$\begin{aligned}[Pb_{(ad)}] &= K_{Pb}[Pb_{(g)}] \\ &= [Pb_{(g)}]e^{-\Delta G_{Pb_{(g)}\rightarrow Pb_{(l)}}/k_BT}.\end{aligned} \tag{3.13}$$

We may relate $[Pb_{(g)}]$ with lead flux Φ_{Pb} using the kinetic theory of gases. The relationship between flux and equivalent gas pressure depends on chamber geometry (held constant for all $PbTiO_3$ growths) and the square root of *source* temperature [47], the latter of which does not vary significantly [2] within the course of this experiment. Thus, we approximate the equivalent lead gas pressure to be linearly dependent on the lead flux. $\Delta G=\Delta H-T\Delta S$; $e^{-\Delta G/k_BT}=e^{-\Delta H/k_BT}e^{+\Delta S/k_B}$. The entropy term $e^{+\Delta S/k_B}$ is a constant in Eq. (3.13). Adsorbed lead $[Pb_{(ad)}]$ will relate to lead flux Φ_{Pb} and substrate temperature T as

$$[Pb_{(ad)}] \propto \Phi_{Pb}e^{-\Delta H_{Pb_{(g)}\rightarrow Pb_{(l)}}/k_BT}. \tag{3.14}$$

$-\Delta H_{Pb_{(g)}\rightarrow Pb_{(l)}}$ is negative under growth conditions; the exponential term on the right

side of Eq. (3.14) decreases with increasing substrate temperature, giving the expected result that at constant lead flux, less lead is available on the surface to form PbO when the substrate is hotter than when the substrate is colder. At *constant* substrate temperature, the concentration of adsorbed lead available to form PbO is directly dependent on lead flux. Considering how the kinetic growth window described by in the main text,

$$k_1[\mathrm{Pb}_{(ad)}][\mathrm{O}_{ad}] \geq \Phi_{\mathrm{Ti}}, \tag{3.15}$$

depends on $[\mathrm{Pb}_{(ad)}]$, we see then that increasing the lead flux has the inverse effect of decreasing the titanium flux: increasing the lead flux will widen the kinetic growth window, as is observed experimentally in Fig. 2(b) of the main text.

The relationship between ozone flux and adsorbed oxygen concentration is more difficult to describe. At pressures near and above one atmosphere and at or below room temperature, adsorbed oxygen on an MnO_2 catalyst is found to vary as $a\log([\mathrm{O}_3])+b/\mathrm{T}$ for a and b constants [119, 120]; however, the observed mechanism of oxygen desorption proceeds through collision of a gas-phase ozone molecule with the adsorbed oxygen atom, which will be significantly rarer at our lower pressures. Thus, this result is unlikely to accurately describe our system.

Oxidation kinetics play an extremely important role in the growth of the superconducting oxide $YBa_2Cu_3O_{7-x}$ by MBE [24, 171, 175], as well as the growth of related oxides by MBE [176], and has therefore been studied extensively. It has been observed that the necessary ozone flux to grow superconducting $YBa_2Cu_3O_{7-x}$ films by codeposited MBE [115, 171] is linearly dependent on combined metal flux. Based on these studies, at MBE-amenable chamber pressures and substrate temperatures, the concentration of adsorbed, possibly-activated oxygen atoms available for oxidizing the film appears to be a linear function of ozone flux.

A linear relationship between ozone flux Φ_{O_3} and $[\mathrm{O}_{(ad)}]$ more closely mirrors the find-

ing shown in Fig. 2(c) in the main text than a logarithmic relationship. Assuming a linear relationship between Φ_{O_3} and $[O_{(ad)}]$, increasing the ozone flux would have an equivalent effect on the kinetic growth window width as does increasing the lead flux.

3.8.4 Measurement of ozone fraction and ozone activity

The ozone concentration originating from the generator was measured to be approximately 9 mol% at the MBE gas inlet as determined with a PCI ozone monitor [155]. To calibrate the activity of ozone at the sample surface a quartz crystal monitor (QCM) was lowered into the substrate position and the mass accumulation rate was monitored as a continuous flux of bismuth was deposited under varying chamber background pressures with diatomic oxygen, generator ozone, and distilled ozone. Using the atomic masses of each species, it was possible to determine the stoichiometry of the depositing material from the mass accumulation rate. The results are shown in Fig. 3.4.

It was observed that pure diatomic oxygen was not sufficient to oxidize bismuth to a 3+ state at a chamber background pressure of 1×10^{-6} Torr. The activity of ozone compared to diatomic oxygen for the oxidation of bismuth was calculated by comparing the pressure necessary to obtain Bi_2O for pure oxygen and 9 mol% ozone. Assuming unity sticking coefficients for both oxygen and bismuth at room temperature, a mass accumulation rate consistent with Bi_2O formation was observed at a chamber background pressure of 1×10^{-6} Torr for pure oxygen and 4.6×10^{-8} Torr for 9 mol% ozone (4.1×10^{-9} Torr ozone partial pressure). This results in a 250:1 pressure ratio for diatomic oxygen to partial pressure ozone, suggesting that ozone is 250× more active in oxidizing bismuth than diatomic oxygen in the process chamber in which we grew $BiFeO_3$.

9 mol% ozone oxidizes bismuth to a 3+ state, allowing formation of Bi_2O_3, at a chamber background pressure of 6×10^{-7} Torr. Distilled ozone allows formation of Bi_2O_3 at a

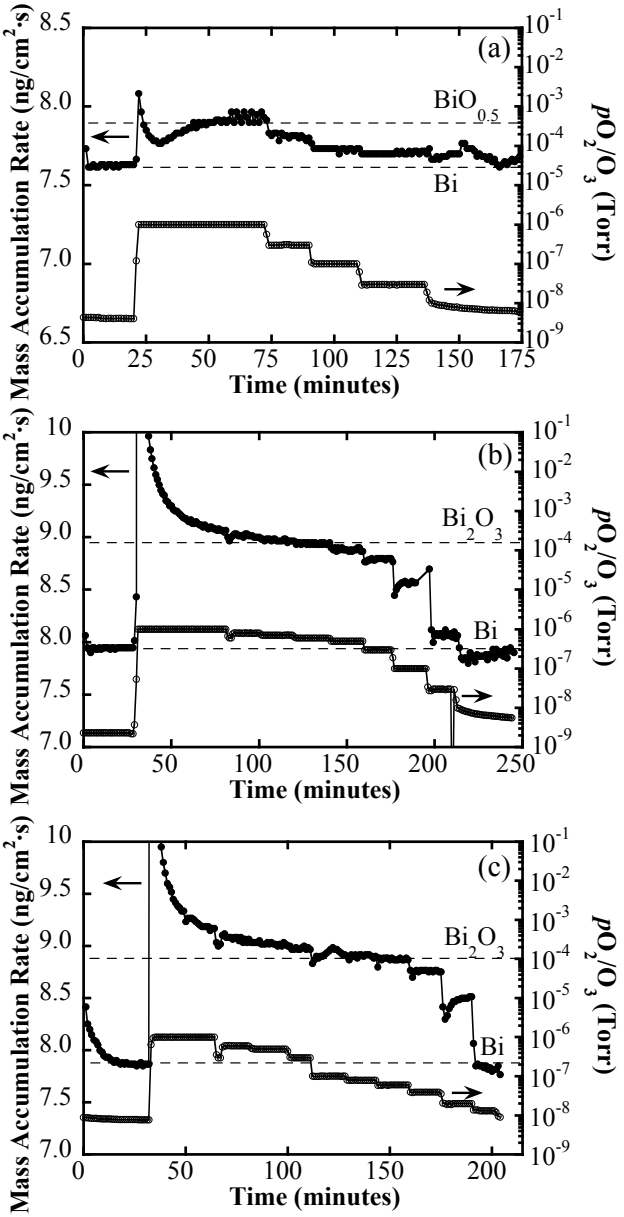

Figure 3.4: Mass accumulation rates measured on a QCM with constant bismuth flux and various oxidants and background pressures. (a) Accumulation of Bi_2O in pure diatomic oxygen (100% O_2). (b) Accumulation of Bi_2O and Bi_2O_3 in generator ozone (9% O_3, 91% O_2). (c) Accumulation of Bi_2O_3 in generator ozone (calculated to be 90% O_3, 10% O_2).

background pressure of 6×10^{-8} Torr. This results in a 10:1 pressure ratio for 9 mol% ozone to distilled ozone, suggesting that the distilled ozone is 90 mol% ozone (O_3) and 10 mol% diatomic oxygen (O_2).

3.8.5 Secondary phases that appear in the growth of $BiFeO_3$

At lower ozone fraction and at high temperatures, γ-Fe_2O_3 is favored by thermodynamics. At high temperatures and high ozone fraction, Fe_3O_4 is favored as a bulk phase. We hypothesize that one contributor to the difference between what is predicted theoretically and what is observed experimentally stems from crystallographic symmetry considerations. α-Fe_2O_3 possesses rhombohedral symmetry (space group $R\bar{3}c$), which is similar to that of $BiFeO_3$ (space group $R3c$). α-Fe_2O_3 possesses a pseudocubic lattice parameter of 3.56 Å that is, however, significantly smaller than that of the $SrTiO_3$ substrate (3.905) and $BiFeO_3$ (3.96). From strain considerations, the overall film strain would be decreased with the presence of the smaller lattice parameter of α-Fe_2O_3 epitaxially embedded in the $BiFeO_3$ matrix. Contrarily, Fe_3O_4 is a cubic spinel (space group $Fd\bar{3}m$) with a lattice parameter of 8.375 . If it were to exist in a (111)-orientation similar to γ-Fe_2O_3, a tensile lattice mismatch of approximately 1.1% would exist. This lattice match difference could be a contributor in the system preference toward the α-Fe_2O_3 phase. The presence of α-Fe_2O_3 as the secondary phase at high oxidant pressures is also consistent with results observed for growth of epitaxial $BiFeO_3$ in high-oxygen concentration containing atmospheres by pulsed-laser ablation [18] and rf-sputtering [50].

CHAPTER 4

MULTIPLE X-RAY SCATTERING MAY BE WIDESPREAD IN COHERENT, EPITAXIAL OXIDE THIN FILMS

Manuscript in preparation as: Smith, Eva H.; King, Phil D. C.; Dawley, Natalie M.; and Schlom, Darrell G. **2017**. A few minor changes have been made.

4.1 Abstract

In numerous symmetric θ-2θ scans of phase-pure epitaxial oxide thin films grown on single-crystal substrates, we observe x-ray diffraction peaks that correspond to neither the film nor the substrate crystal structure. These peaks are the result of multiple, sequential diffraction events that occur from both the film and substrate. The occurrence of so-called "hybrid" reflections, while described in the literature, is not widely reported within the oxide thin-film community. We describe a simple method to predict and identify peaks resulting from hybrid reflections and show examples from epitaxial oxide films of perovskite and Ruddlesden-Popper phases.

4.2 Introduction

Four-circle x-ray diffraction is an essential tool for the characterization of epitaxial thin films, giving information about crystalline phases present, their orientation, and structural perfection. Of particular importance is the ability of x-ray diffraction to determine whether a particular sample consists of a single phase or a mixture of phases. For a phase identification to be considered correct, all features (peaks in intensity) in a scan of intensity *versus* 2θ must be identified. Any unidentified peaks call into question the phase purity of the thin film.

Multiple scattering events have been described in x-ray diffraction since 1937 [164] as causing unexpected intensity at symmetry-forbidden reflections from single crystals. More recently, hybrid scattering events, in which a beam that is diffracted by the substrate is then diffracted a second time by the film, have been identified as giving rise to reflections that correspond to neither the film reciprocal lattice nor the substrate reciprocal lattice, but rather, a "hybrid" reciprocal lattice, whose reflections are measured at angles 2θ at which no film or substrate reflections occur [139]. Almost every discussion or report in the literature of hybrid reflections in x-ray diffraction experiments uses either synchrotron radiation sources or reciprocal-space maps to search for and characterize them [52, 130, 137, 138, 139, 140]. These methods, while giving a great deal of information, require either specialized facilities or a significant time investment, and are generally only performed on a few select films rather than as a matter of course. Furthermore, we are not aware of any reports in peer-reviewed journals of hybrid reflections from oxide thin films. We argue here that such reflections may be sufficiently common that checking for hybrid reflections should be a matter of course when analyzing diffraction data from high-quality oxide thin films.

For identification of hybrid reflections in symmetric 2θ scans, we calculate the expected angle 2θ at which a hybrid reflection is expected to occur in the following way. Consider the hybrid reflection arising from the $h_s k_s l_s$ reflection from a substrate with reciprocal lattice vectors $\vec{a_s^*}$, $\vec{b_s^*}$, $\vec{c_s^*}$ and the $h_f k_f l_f$ reflection from a film with reciprocal lattice vectors $\vec{a_f^*}$, $\vec{b_f^*}$, $\vec{c_f^*}$. We define reciprocal lattice vectors from the real-space lattice vectors $\vec{a}$, $\vec{b}$, $\vec{c}$ as follows:

$$\vec{a^*} = \frac{\vec{b}\times\vec{c}}{\vec{a}\cdot\vec{b}\times\vec{c}}\,; \quad \vec{b^*} = \frac{\vec{c}\times\vec{a}}{\vec{a}\cdot\vec{b}\times\vec{c}}\,; \quad \vec{c^*} = \frac{\vec{a}\times\vec{b}}{\vec{a}\cdot\vec{b}\times\vec{c}}\,. \tag{4.1}$$

The scattering vector of the hybrid reflection $\vec{G_u}$ will be the sum of the scattering vectors

of the reflection from the substrate, $\vec{G}_s$, and the reflection from the film, $\vec{G}_f$ [139]:

$$\begin{aligned}\vec{G}_s &= h_s\vec{a}_s^* + k_s\vec{b}_s^* + l_s\vec{c}_s^* \\ \vec{G}_f &= h_f\vec{a}_f^* + k_f\vec{b}_f^* + l_f\vec{c}_f^* \\ \vec{G}_u &= \vec{G}_f + \vec{G}_s.\end{aligned} \tag{4.2}$$

Bragg's law may be used to find the angle 2θ at which the peak occurs:

$$2\theta = 2\mathrm{Sin}^{-1}\left(\frac{\lambda|\vec{G}_u|}{2}\right). \tag{4.3}$$

For coherently-strained, epitaxial films grown "cube-on-cube" relative to their substrates, the in-plane lattice vectors of the film and substrate are the same, and $\vec{a}_s^*=\vec{a}_f^*$ and $\vec{b}_s^*=\vec{b}_f^*$. Then when $h_s=-h_f$ and $k_s=-k_f$, the in-plane component of the hybrid reflection $h_s\vec{a}_s^* + h_f\vec{a}_f^* + k_s\vec{b}_s^* + k_f\vec{b}_f^*$ is null and the resulting hybrid reflection is a symmetric reflection, able to be observed during ordinary θ-2θ x-ray diffraction scans [139].

Many epitaxial oxide thin films grown by pulsed-laser deposition (PLD), molecular-beam epitaxy (MBE), and chemical vapor deposition (CVD) are grown with high structural quality, *e.g.* highly oriented relative to their substrates in-plane [26, 55, 79, 127, 129, 143, 162, 216, 219], film rocking curve full-width half maximum $\leq 0.01^\circ$ [60, 97, 143]. For such films, we present a simple relationship between film and substrate lattice constants and the angles 2θ at which hybrid reflections can be expected to occur. For substrates and films with cubic, tetragonal, or orthorhombic symmetry, the norm of the hybrid scattering vector $|\vec{G}_u|$ relates to the scalar substrate out-of-plane lattice parameter, c_s, and the scalar film out-of-plane lattice parameter, c_f, by

$$|\vec{G}_u| = \frac{l_s}{c_s} + \frac{l_f}{c_f}, \tag{4.4}$$

and the angle 2θ at which this reflection is observed is found by plugging in $|\vec{G}_u|$ from Eq. (4.4) into Eq. (4.3):

$$2\theta = 2\mathrm{Sin}^{-1}\left(\frac{\lambda}{2}\left|\frac{l_s}{c_s} + \frac{l_f}{c_f}\right|\right). \tag{4.5}$$

We will use Eq. (4.5) to predict the 2θ angles for hybrid reflections in this manuscript.

In addition to comparing predicted 2θ values for hybrid reflections to peak positions measured experimentally, we also identify hybrid reflections through the dependence of their intensity on azimuthal rotation angle ϕ. In contrast to symmetric reflections from the film or substrate, the intensity of hybrid reflections is strongly dependent on ϕ, commonly showing hundreds of distinct peaks as intensity is measured as a function of azimuthal angle. This dependence may be understood by the fact that while these hybrid reflections have no net in-plane scattering component, they arise as a sum of reflections that do, in general, have finite in-plane components. Measuring the ϕ-dependence of a peak present in a θ-2θ scan is a traditional method for identifying the contribution of multiple diffraction events to its intensity [37, 46, 164, 167].

In the examples that follow, we focus our discussion on the appearance of hybrid reflections in θ-2θ scans, a standard scan for phase characterization [48], and their verification with ϕ scans. Due to the increasing numbers of reports of high-quality, heteroepitaxial oxide films, we expect that hybrid reflections are observed more commonly than they are mentioned in the literature.

4.3 Methods

Thin films were grown by reactive molecular-beam epitaxy on single-crystal substrates. $SrTiO_3$ (001) substrates were TiO_2-terminated [110].

$PbTiO_3$ was grown in an absorption-controlled growth regime using a procedure described elsewhere [184]. In brief, the substrate temperature was 580°C, the lead flux was 2×10^{14} atoms cm^{-2} s^{-1}, the titanium flux was 9×10^{12} atoms cm^{-2} s^{-1}, the distilled ozone (~80% O_3 + 20% O_2) background pressure was 6×10^{-6} Torr, and all constituent molecular

beams were supplied at the same time (continuous codeposition).

La_2NiO_4 was grown on (001) LSAT as described in previously [104]. In short, the film was grown by sequential deposition of binary oxide monolayers $[LaO\text{-}NiO_2\text{-}LaO]_{40}$.

To grow $Ba_{0.2}Sr_{0.8}TiO_3$, the strontium, barium, and titanium fluxes were calibrated such that, when sequential doses of strontium and titanium were deposited, the strontium deposition time was 1.25 times the titanium deposition time; and that when sequential doses of (codeposited strontium and barium) and titanium were deposited, the (strontium and barium) deposition time was equal to the titanium deposition time. The substrate temperature was 800°C, the titanium flux was ~1.5×10^{13} atoms cm^{-2} s^{-1}, and the oxidant was the ~10% ozone output of a commercial ozone generator yielding a chamber background pressure of 9×10^{-7} Torr. After individual source doses were calibrated, films of $Ba_{0.2}Sr_{0.8}TiO_3$ were grown by continuous codeposition of all sources while the sample was continuously rotated and the surface monitored by reflection high-energy electron diffraction (RHEED) for signs of either *A*-site or *B*-site excess [211]. Films were grown by codeposition to increase growth rates and with the goal of increasing uniformity at the atomic level. Source temperatures (fluxes) were adjusted as necessary throughout growth to maintain correct stoichiometry.

X-ray diffraction measurements were performed in θ-2θ geometry at room temperature on a commercial Rigaku SmartLab using Cu $K\alpha_1$ radiation monochromated with a double crystal Ge 220 monochromator. Film out-of-plane lattice parameters are found using Nelson-Riley fitting [147] of the $00l$ film peak positions from symmetric θ-2θ scans. In the ϕ scans, $\phi = 0$ corresponds to where the in-plane component of the diffraction vector is aligned parallel to the [100] direction of the substrate.

4.4 Results

In this section we consider the x-ray diffraction patterns from three films: 50 nm-thick $PbTiO_3/SrTiO_3$ (001); 200 nm-thick $Ba_{0.2}Sr_{0.8}TiO_3/SrTiO_3$ (001); and 25 nm-thick La_2NiO_4/LSAT (001). The first two films are both tetragonal perovskites with the long tetragonal axis oriented out-of-plane; the first forms in space group $P4mm$ and the second in space group $P4/mmm$. The third sample, La_2NiO_4, is the $n = 1$ member of the homologous Ruddlesden-Popper series $La_{n+1}Ni_nO_{3n+1}$. This structure also belongs to a tetragonal space group $I4/mmm$ at room temperature, with the long axis out of plane. $SrTiO_3$ and LSAT are cubic perovskites at room temperature, forming in space group $Pm\bar{3}m$.

For each film we present θ-2θ patterns taken at several values of ϕ and observe how the peaks arising from hybrid reflections change dramatically in intensity while the peaks arising from single diffraction from the film or substrate stay constant. We also present ϕ scans of the hybrid reflections and film reflections. ϕ scans of the film and substrate lattice verifying cube-on-cube epitaxy are shown in the Supplementary Materials.

In Fig. 4.1 we show θ-2θ scans (a-b) and ϕ scans (c) of a 50-nm-thick $PbTiO_3/SrTiO_3$ (001) sample. As ϕ is changed, four extra peaks beyond what would be expected from a superposition of the $SrTiO_3$ and $PbTiO_3$ patterns appear and disappear in the θ-2θ scan: two extra peaks near the film and substrate 001 reflections, and two extra peaks near the film and substrate 002 reflections. We see the first two of these extra peaks at 24.1° and 25.4°; we see the second two at 45.8° and 47.9°. Using the measured c-lattice constant for this $PbTiO_3$ film of 4.138 Å and a c-lattice constant of 3.905 Å for the $SrTiO_3$ substrate [8], Eq. (4.5) predicts that hybrid reflections between $PbTiO_3$ and $SrTiO_3$, will occur at the angles marked with dashed lines in the θ-2θ scans of Fig. 4.1. All four extra peaks fall at angles predicted for hybrid reflections.

To solidify our belief that the "extra" peaks result from hybrid reflections, we rotate

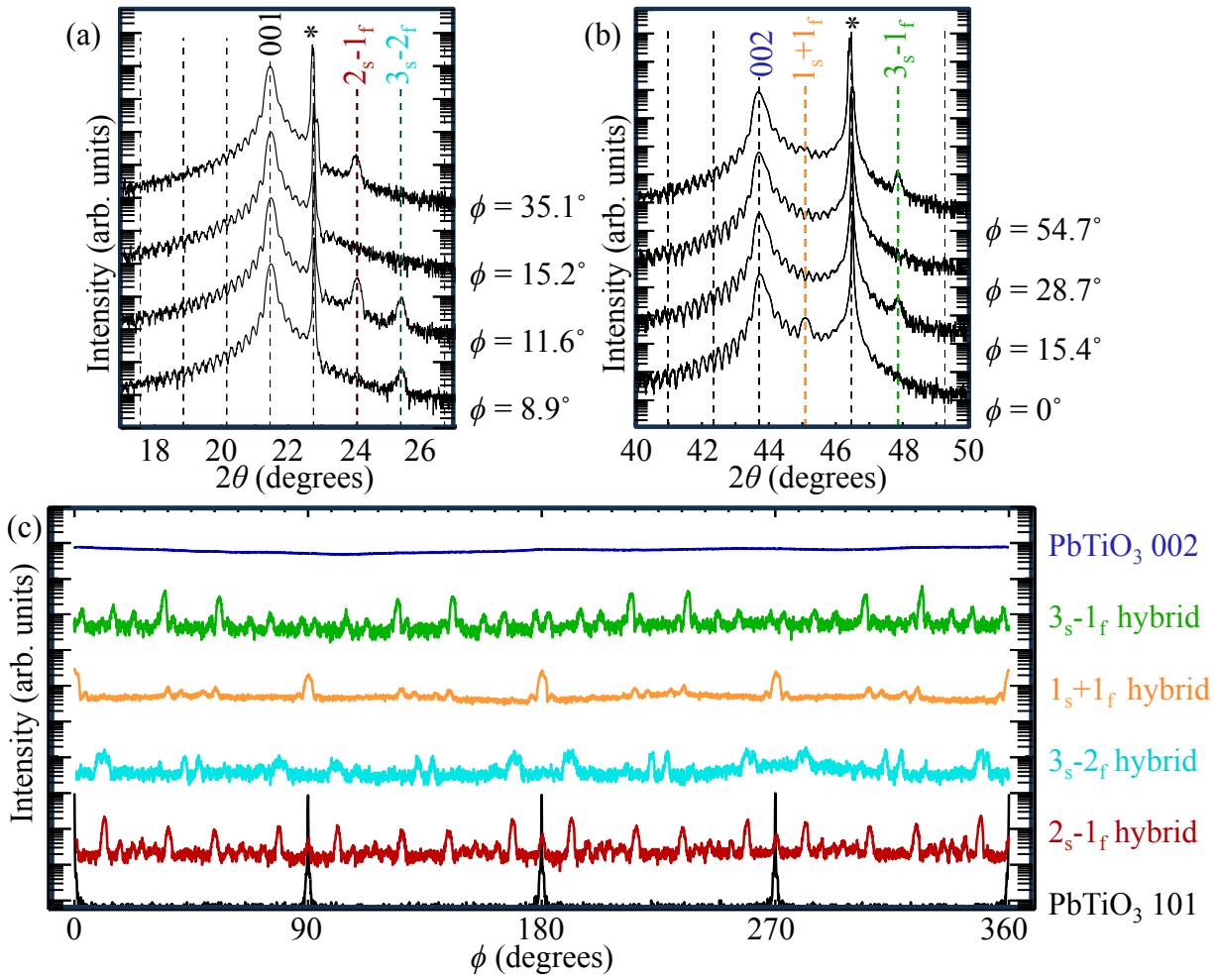

Figure 4.1: Dependence of regular and hybrid reflections on (a), (b) 2θ and (c) ϕ in a 50 nm-thick film of $PbTiO_3$ grown on $SrTiO_3$ (001). The dashed lines in the θ-2θ scan correspond to the expected positions of hybrid reflections calculated using Eq. (4.5). Hybrid reflections are indexed by l_s and l_f.

the sample about ϕ and measure the changing x-ray intensity at each of the four extra reflections. For reference, we also measure how the intensity of a symmetric, singly-diffracted film reflection varies with ϕ; and we measure the position in ϕ of the film 101 peak. The film and hybrid reflections depend very differently on ϕ. The intensity of the $PbTiO_3$ 002 reflection is nearly constant as a function of ϕ, while the intensities of the hybrid reflections vary rapidly.

Similar features are seen in the θ-2θ x-ray diffraction pattern near the film and substrate

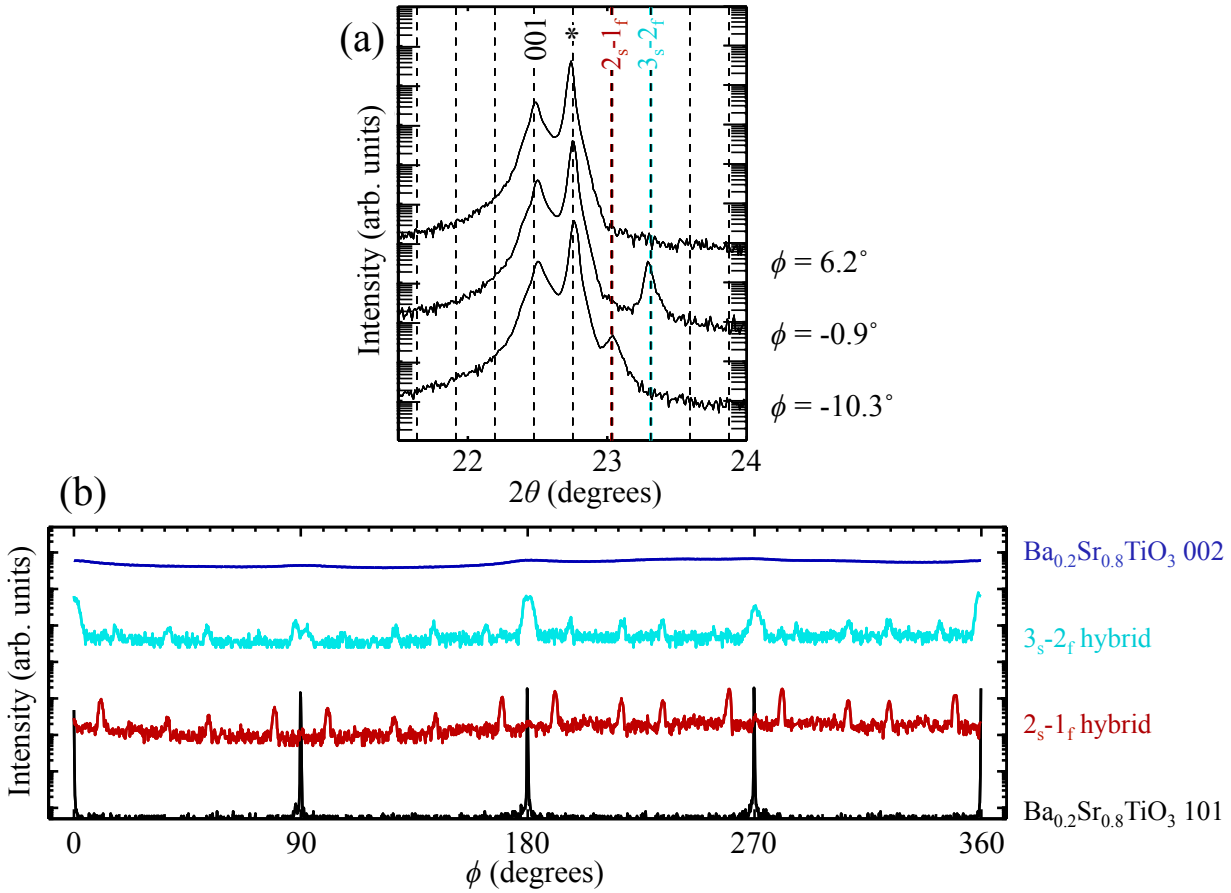

Figure 4.2: Dependence of regular and hybrid reflections on (a) 2θ and (b) ϕ in a 200-nm-thick film of $Ba_{0.2}Sr_{0.8}TiO_3$ grown on $SrTiO_3$ (001). The dashed lines in (a) correspond to the expected positions of hybrid reflections calculated using Eq. (4.5). Hybrid reflections are indexed by l_s and l_f.

001 reflections of a 200 nm-thick film of $Ba_{0.2}Sr_{0.8}TiO_3$ grown on $SrTiO_3$ (001), shown in Fig. 4.2(a). Two peaks at slightly higher angle than the substrate 001 peak appear or disappear as ϕ is rotated. These peaks appear at the angles in θ-2θ calculated for hybrid reflections using the measured lattice constant for this film: c_f=3.953 Å and c_s=3.905 Å [8]. While these peaks occur at different angles than the two hybrid reflections in the $PbTiO_3$ film, they show similar, rapidly-varying behavior with respect to ϕ rotation, as shown in Fig. 4.2(b) and thus may also be attributed to hybrid diffraction.

Having considered hybrid reflections from two perovskite thin films, we next consider

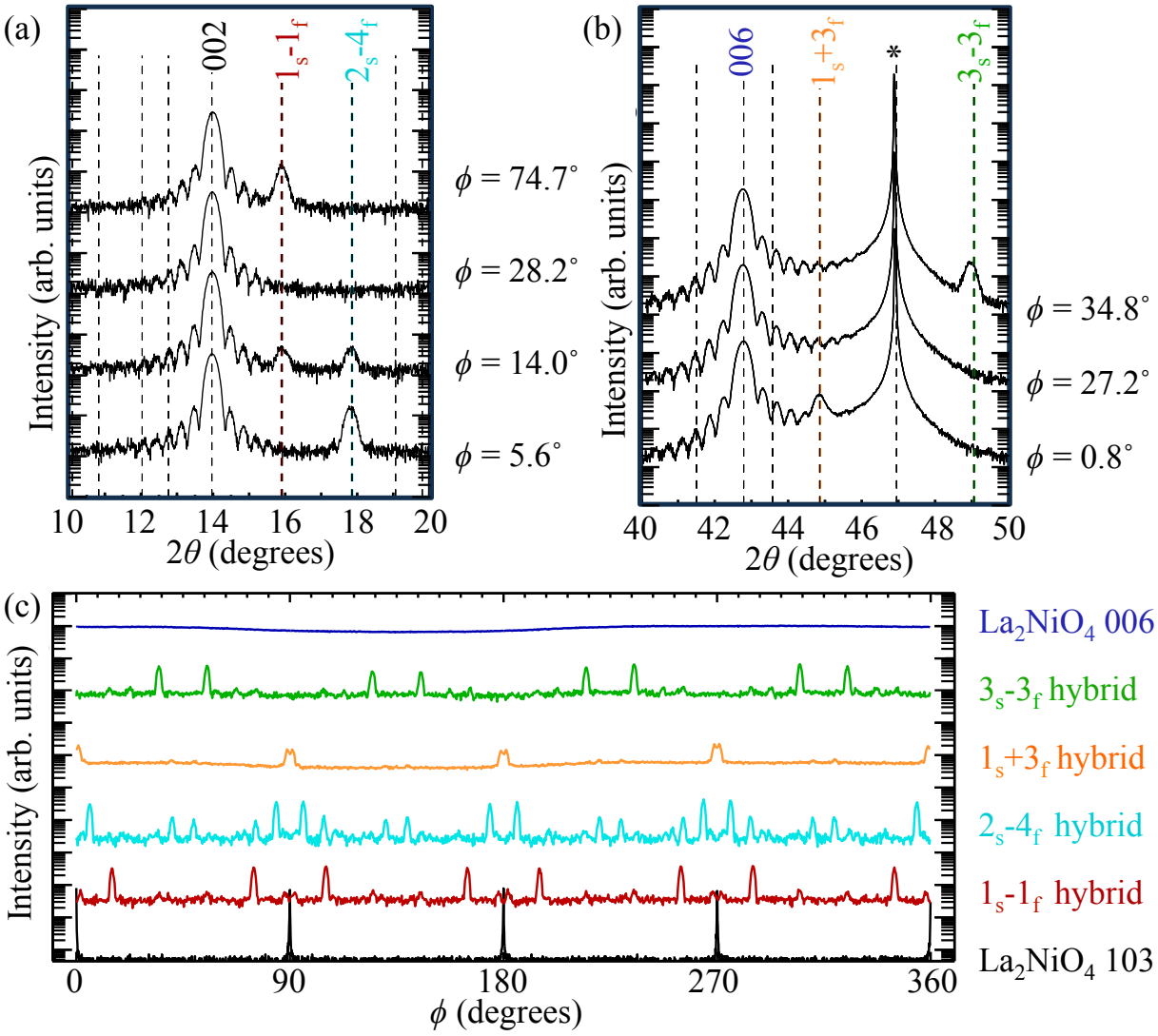

Figure 4.3: Dependence of regular and hybrid reflections on (a), (b) 2θ and (c) ϕ in a 25-nm-thick film of La_2NiO_4 grown on LSAT (001). The dashed lines in (a) and (b) correspond to the expected positions of hybrid reflections calculated using Eq. (4.5). Hybrid reflections are indexed by l_s and l_f.

hybrid reflections from a Ruddlesden-Popper film, a structural relative to the perovskite [15, 169, 170]. θ-2θ scans at various ϕ, and ϕ-scans at various values of 2θ, from a 25-nm-thick film of La_2NiO_4 grown on LSAT (001), are shown in Fig. 4.3. Four hybrid reflections appear in the θ-2θ x-ray diffraction patterns near the film 002 and the film 006 reflection, shown in Fig. 4.3(a) and Fig. 4.3(b), respectively. The hybrid reflections near the film 002 reflection appear to show thickness fringes, similar to the film reflections. The hybrid

reflections appear at values of 2θ predicted using Eq. (4.5) using c_s=3.8672 Å and the measured out-of-plane lattice constant of the film, c_f=12.6695 Å. The many discreet peaks of intensity in ϕ seen in Fig. 4.3(c) adds further support to our belief that these four extra reflections are also due to hybrid diffraction.

4.5 Discussion

Based on the appearance of hybrid reflections in the three films, belonging to two distinct structural types, considered in Section 4.4, we believe that it is likely that such hybrid reflections may occur in symmetric θ-2θ scans of high-crystalline quality thin films as long as they meet the crystallographic requirements described below. Such peaks will furthermore be detectable with a commercial benchtop diffractometer when the intensity of an x-ray beam diffracted (once) from the film is sufficiently large. This latter condition is met if the film is sufficiently thick, the film contains a high concentration of atoms with high atomic number, the film and substrate have a sufficiently-large number of high-intensity reflections, or the x-ray source is sufficiently bright. We may approximate a ceiling for the intensity of a hybrid reflection using a procedure like that described in the Supplementary Information. Based on this method we expect that the most intense hybrid reflection in all three samples considered here combines the most intense substrate-only reflection with the most intense film-only reflection; this prediction is in agreement with our observations.

In deriving Eq. (4.5) we assumed that the film would be coherently strained, epitaxial, and grown cube-on-cube relative to the substrate. Growth of single-crystal, coherently strained, heteroepitaxial oxide films with high structural perfection (film rocking curve full-width half maximum $\leq 0.01^\circ$) is increasingly common [60, 97, 143] and also increasingly accessible [3].

Interestingly, we also have observed hybrid reflections from films that do not strictly meet the structural criteria described in the Introduction. First, we have measured hybrid reflections from a 300-nm thick film of $PbTiO_3$ grown on $SrTiO_3$ that is relaxed, with a mixture of *a*- and *c*-domains, though still cube-on-cube epitaxial. Second, we have measured hybrid reflections from a 100-nm-thick film of $BaSr_2Ti_2O_7$ grown on $DyScO_3$ (110); $DyScO_3$ is orthorhombic, while the $BaSr_2Ti_2O_7$ is tetragonal. The hybrid reflections from these two films that appear in symmetric θ-2θ scans likely are broadened, with finite intensity along the in-plane direction as well as that which was detected along the out-of-plane direction. Many high-quality, single-crystal, heteroeptiaxial oxide films are highly oriented relative to their substrates in-plane, as were these two films, as shown through reciprocal-space maps or reflection high energy electron diffraction of both film and substrate [26, 55, 79, 127, 129, 143, 162, 216, 219].

We conclude that hybrid reflections may be expected from heteroepitaxial oxide thin films that: (1) are grown close to cube-on-cube relative to their substrates; (2) have an in-plane lattice constant close to that of the underlying substrate, though not necessarily perfectly coherent; (3) have low mosaicity [36]; and (4) scatter sufficiently brightly. The combination of more films being grown and studied that meet the criteria for hybrid reflections with awareness of how to predict and verify hybrid reflections by thin-film scientists makes us anticipate that reports of hybrid reflections in the literature will grow.

4.6 Conclusions

We have presented three cases in which multiple x-ray diffraction events are observed in symmetric θ-2θ scans of epitaxial oxide thin films. We demonstrate how these hybrid reflections may be identified based on the angle 2θ at which they appear and their rapidly changing intensity as the sample is rotated about the azimuthal angle ϕ. Based on the

diversity of films in which we observe such behavior, the fact that we use no special techniques or equipment to collect our diffraction data, and the growing numbers of reports of heteroepitaxial thin films with high crystalline quality, we believe that hybrid reflections may be more common they are mentioned in the literature.

4.7 Acknowledgements

E. H. S. wishes to acknowledge Ard H. G. Vlooswijk, without whose dissertation, written under the guidance of Prof. dr. B. Noheda and Prof. dr. T. T. M. Palstra at the Rijksuniverseiteit Groningen, she may have never considered the phenomenon of hybrid reflections in the context of thin films nor appreciated the facility with which such reflections could be predicted or identified. E.H.S. and D.G.S. acknowledge support by the National Science Foundation (NSF) MRSEC program (DMR-1420620). This work made use of the Cornell Center for Materials Research (CCMR) Shared Facilities, which are supported through the NSF MRSEC program (DMR-1120296). Substrate preparation was performed in part at the Cornell NanoScale Facility, a member of the National Nanotechnology Coordinated Infrastructure (NNCI), which is supported by the NSF (Grant ECCS-15420819).

4.8 Supplementary Information

4.8.1 Proof of cube-on-cube epitaxy

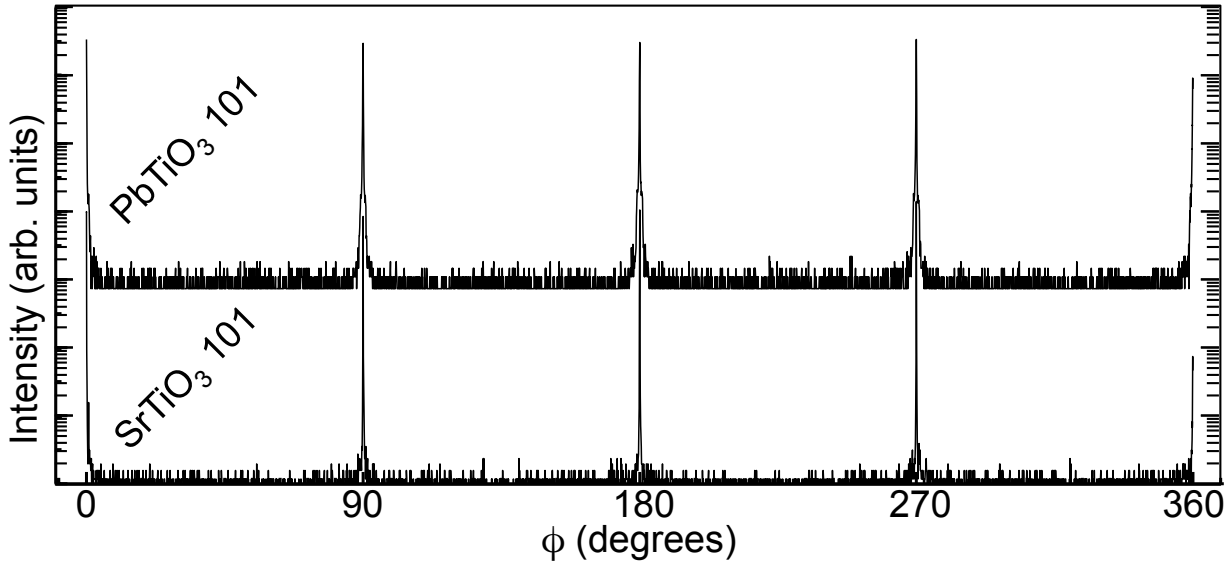

Figure 4.4: ϕ scans of the film and substrate 101 peaks of the 50-nm-thick $PbTiO_3/SrTiO_3$ (001) film, demonstrating cube-on-cube epitaxy.

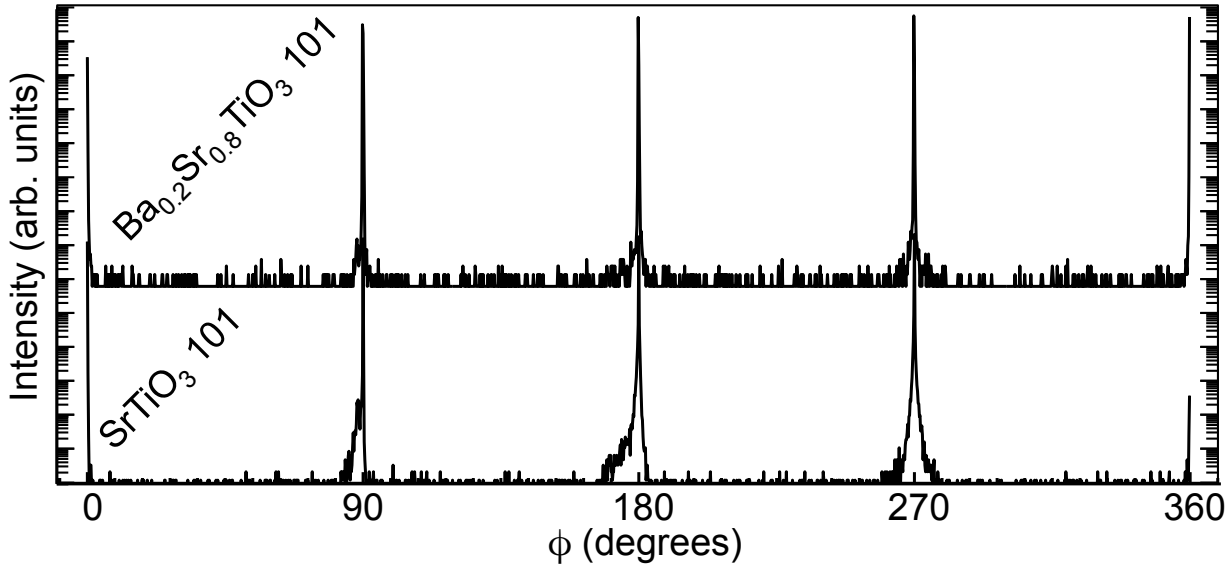

Figure 4.5: ϕ scans of the film and substrate 101 peaks of the 200-nm-thick $Ba_{0.2}Sr_{0.8}TiO_3/SrTiO_3$ (001) film, demonstrating cube-on-cube epitaxy.

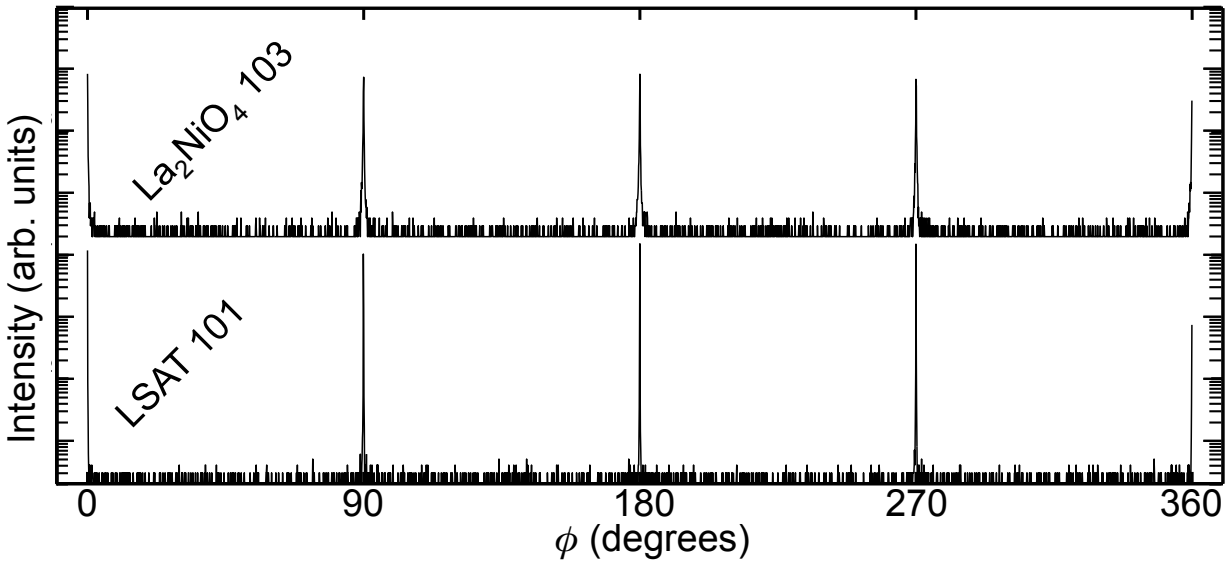

Figure 4.6: ϕ scans of the film 103 and substrate 101 peaks of the 25-nm-thick La_2NiO_4/LSAT (001) film, demonstrating cube-on-cube epitaxy.

4.8.2 Simple method for calculating the ceiling of a hybrid reflection intensity

Consider a hybrid reflection that may arise from a substrate reflection $h_s k_s l_s$ followed by a film reflection $h_f k_f l_f$, appearing at angle 2θ=$2\theta_u$. The intensity of the substrate reflection I_s, if it does not undergo a second scattering event but simply is transmitted through the film, may be measured by suitable alignment of the detector. This intensity will be related to the intensity of the once-diffracted beam as it leaves the substrate $I_{s,0}$ through an attenuation factor [58]:

$$I_s = I_{s,0} \exp\left[-\frac{\mu_f t_f}{\sin(\omega_s)}\right], \tag{4.6}$$

for t_f the film thickness, μ_f the film linear attenuation coefficient, and ω_s half of the angle 2θ at which the once-diffracted beam is measured, as shown in Fig. 4.7. The linear attenuation coefficient can be found as the product of the mass attenuation coefficient and the density [150]. The mass attenuation coefficient for a compound is a weighted sum of the mass attenuation coefficients for each constituent atom at the appropriate photon

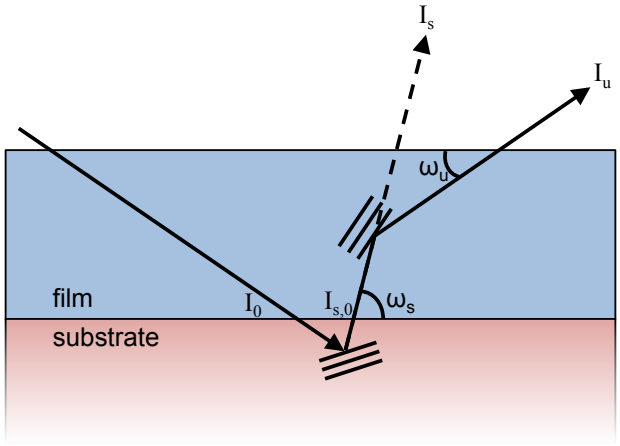

Figure 4.7: Geometry of sample.

energy [91]. Atomic mass attenuation coefficients may be found through tables such as those compiled by NIST [91].

The intensity of the hybrid reflection I_u can be found by the standard methods for calculating the intensity of a diffracted spot from a film at diffraction angle θ_f associated with the film reflection $h_f k_f l_f$, weighted by the probability that the beam will interact with the film [58]:

$$I_u = I_{s,0} F_f(\theta_f) \left(1 - \exp\left[-\mu_f t_f \left(\frac{1}{\sin(\omega_s)} + \frac{1}{\sin(\omega_u)}\right)\right]\right) \tag{4.7}$$

for $F_f(\theta_f)$ including terms for structure factor, general angular intensity dependence, and degeneracy, with the requirement that the beam reflected from the film must have a positive, non-zero component out-of-plane, and ω_u half of the angle $2\theta_u$ at which the two-diffracted beam is measured.

The intensity ratio of the hybrid reflection to the substrate-only reflection may then be approximated by:

$$\frac{I_u}{I_s} = F_f(\theta_f) \exp\left[+\mu_f t_f \frac{1}{\sin(\omega_s)}\right]\left(1 - \exp\left[-\mu_f t_f \left(\frac{1}{\sin(\omega_s)} + \frac{1}{\sin(\omega_u)}\right)\right]\right). \tag{4.8}$$

We note first that this calculated value corresponds to the total intensity of the hybrid reflection integrated over reciprocal space, and that this value corresponds to a maximum

value with no scattering from the surface or grain boundaries and perfect cube-on-cube epitaxy and perfect coherence between the film and substrate; the intensity of hybrid reflections from real films should be expected to be less.

CHAPTER 5

SUMMARY AND FUTURE DIRECTIONS

5.1 Summary

I have described cases of prediction, growth, and characterization of three perovskite systems. In the Introduction I mentioned that I hoped my dissertation would make at least a small contribution to the answers of three important questions to materials scientists. In summary, within the circumstances of each chapter, my answers to each were as follows.

How does a collection of atoms decide what structure to take in the solid state? Assuming sufficiently fast diffusion that the collection of atoms may find its thermodynamic ground state, the atoms will take the structure that is the best compromise among the bonding requirements of each species. Within perovskite $CsPbF_3$, the ground state structure is that which permits localization of the Pb^{2+} lone pair while allowing the large Cs^+ cation a sufficiently large coordination number, within the topological constraints of the three-dimensional anion sublattice.

How can I facilitate the growth of the crystal phases and structures that I want? Even when thermodynamics favor formation of a particular phase, the role of kinetics in thin film growth cannot be discounted. Consideration of the rate-limiting chemical reactions in material synthesis allows rational selection of growth conditions and reproducible growth of high-quality films. $PbTiO_3$ is formed by reaction of TiO_2 and PbO; formation of either TiO_2 or PbO may be rate-limiting to the overall growth. If TiO_2 deposition is rate-limiting, then the resulting film is phase-pure $PbTiO_3$, but if TiO_2 formation is faster than lead oxidation, then the resulting film will be an impure mixture of $PbTiO_3$ and TiO_2. To grow phase-pure $PbTiO_3$, then, the lead oxidation must be allowed to proceed as quickly as possible; in practice this requires supplying as much ozone as possible

and significantly more lead than titanium.

How do I confirm that my interpretation of an x-ray diffraction pattern is correct? In a symmetric x-ray diffraction scan, the lattice planes measured by single diffraction events are normal to sample azimuthal axis, and thus rotation of the sample about the azimuthal axis ϕ should not change the peak intensity. When multiple diffraction events occur, however the route taken by the x-ray beam is more circuitous and will in general involve reflections with a finite in-plane component of the scattering vector. As a result, rotation of the sample about ϕ will dramatically change the peak intensity. The position 2θ of doubly-diffracted peaks may be predicted mathematically and their identification verified by measuring their intensity dependence upon ϕ. In this way a scientist can be certain that the extra peak in her pattern is due to this unusual phenomenon.

5.2 Future directions

The following are ongoing or unfinished projects as of June 2017.

Optimizing the ferroelectric hysteresis of $PbTiO_3$ thin films grown by MBE. $PbTiO_3$ is a prototypical ferroelectric, with a large remnant polarization. Molecular-beam epitaxy is a prime method to grow thin films with high crystalline quality. It may be considered surprising, then, that the ferroelectric properties of thin $PbTiO_3$ films grown by MBE are generally poor, with significant leakage being a particular problem. Research assistant Ariel Seidner has done ferroelectric measurements on some of my MBE-grown $PbTiO_3$ thin films and found remarkably good ferroelectric properties, in particular low leakage. This project, if taken on by a new researcher, would attempt to pinpoint the reason the films have such good ferroelectric properties. I suspect that issues with stoichiometry control – and, in particular, the presence of lead vacancies due to incomplete lead oxida-

tion – may be to blame for the poor ferroelectric properties of other thin films grown by MBE. One could grow $PbTiO_3$ thin films in which the substrate is held fixed, rather than continuously rotated, during growth, resulting in films with a spatial composition gradient. Measurement of the ferroelectric properties as a function of position on the sample could illuminate the role of composition in the ferroelectric properties of thin $PbTiO_3$ films grown by MBE. Measurement of the thermal conductivity as a function of position could also illuminate the region(s) of the film that have lowest concentration of point defects and which are therefore likely to have stoichiometry closest to the nominal $Pb_1Ti_1O_3$.

Effect of the ferroelectric phase transition on thermal conductivity near room temperature Phonons are the primary heat-carriers in crystalline insulators. Phonons also mediate displacive phase transitions, including ferroelectric phase transitions. As the temperature of a displacive phase transition is approached from above, a phonon will soften (decrease in frequency) until, at the phase transition temperature, the restoring force on the atomic displacements will vanish and the phonon mode will "freeze in." Just above the phase transition temperature this phonon mode has the potential to interact with heat-carrying phonons, possibly resulting in significant changes to thermal conductivity. I have grown several $Ba_xSr_{1-x}TiO_3$ thin films coherently strained on various substrates, giving a range of Curie temperatures. In this project, collaborators will measure thermal conduction in these films as a function of temperature to assess the effect of the phase transition. One could also grow more films to probe the different effects of strain and composition (each of which changes the Curie temperature) on the thermal conductivity.

Crystal chemistry and stability of Ruddlesden Poppers I did a first-principles project probing the chemistry and stability of Ruddesden Poppers, with emphases on those in which n=1 and Ca_2TiO_4 in particular. Part of this project was predicting the epitaxial strain conditions under which Ca_2TiO_4 would be a stable phase in the CaO-TiO_2 phase

diagram, with the prediction that this stability could potentially be realized on $LuAlO_3$ (110) substrates. This project seems unlikely to ever be finished or published, but anyone interested is welcome to email me to chat about it at eva.h.smith@gmail.com.

BIBLIOGRAPHY

[1] TEM/EELS map courtesy of Dr. Ye Zhu and Professor David Muller. Film courtesy of Che-Hui Li and Professor Darrell Schlom.

[2] There is a small dependence on the source temperature of the relationship between Pb flux and equivalent Pb gas pressure. The square root of source temperature varies by less than 5 percent throughout the course of the PbTiO3 growth experiements.

[3] http://paradim.cornell.edu/.

[4] Bond valences for Ge^{2+} compounds were calculated using Shannon radii.

[5] In addition to the X_5^+ mode we also remove the M_2^+ and R_5^+, leaving only the octahedral rotations.

[6] SpringerMaterials - The Landolt-Börnstein Database.

[7] Ti-Ball is a registered trademark of Varian Associates, Vacuum Products Division, Lexington, MA.

[8] M. Adachi, Y. Akishige, T. Asahi, K. Deguchi, K. Gesi, K. Hasebe, T. Hikita, T. Ikeda, Y. Iwata, Other, and Authors. *Oxides*, volume 36A1 of *Landolt-Börnstein - Group III Condensed Matter*. Springer-Verlag, Berlin, 2001.

[9] Carolina Adamo. Personal communication, April 2017.

[10] M. I. Aroyo, A. Kirov, C. Capillas, J. M. Perez-Mato, and H. Wondratschek. Bilbao Crystallographic Server II: Representations of crystallographic point groups and space groups. *Acta Crystallographica A*, 62:115–128, 2006.

[11] M. I. Aroyo, J. M. Perez-Mato, C. Capillas, E. Kroumova, S. Ivantchev, G. Gadariaga, A. Kirov, and H. Wondratschek. Bilbao Crystallographic Server I: Databases and

crystallographic computing programs. *Zeitschrift für Kristallographie*, 221(1):15–27, 2006.

[12] M. I. Aroyo, J. M. Perez-Mato, D. Orobengoa, E. Tasci, G. de la Flor, and A. Kirov. Crystallography online: Bilbao Crystallographic Server. *Bulgarian Chemical Communications*, 43(2):183–197, 2011.

[13] J. R. Jr. Arthur. Interaction of Ga and As_2 Molecular Beams with GaAs Surfaces. *Journal of Applied Physics*, 39(8):4032–4034, 1968.

[14] Dietrich Babel and Alain Tressaud. *Inorganic Solid Fluorides: Chemistry and Physics*, chapter 3: Crystal Chemistry of Fluorides. Academic Press, Inc.: Orlando, FL, 1985.

[15] D. Balz and K. Plieth. Die Struktur des Kaliumnickelfluorids, K_2NiF_4. *Z. Elektrochem.*, 59:545–551, 1955.

[16] Ihsan Barin. *Thermochemical Data of Pure Substances*. VCH, 1995.

[17] Stefano Baroni and Raffaele Resta. Ab initio calculation of the macroscopic dielectric constant in silicon. *Phys. Rev. B*, 33(10):7017–7021, 1986.

[18] H. Bea, M. Bibes, A. Barthelemy, K. Bouzehouane, E. Jacquet, A. Khodan, J. P. Contour, S. Fusil, F. Wyczisk, A. Forget, D. Lebeugle, D. Colson, and M. Viret. Influence of parasitic phases on the properties of $BiFeO_3$ epitaxial thin films. *Applied Physics Letters*, 87(7):072508, 2005.

[19] Alexei A. Belik, Satoshi Iikubo, Katsuaki Kodama, Naoki Igawa, Shin-ichi Shamoto, Makoto Maie, Takuro Nagai, Yoshio Matsui, Sergey Yu. Stefanovich, Bogdan I. Lazoryak, and Eiji Takayama-Muromachi. $BiScO_3$: Centrosymmetric $BiMnO_3$-Type Oxide. *Journal of the American Chemical Society*, 128(3):706–707, 2006.

[20] Alexei A. Belik, Tuerxun Wuernisha, Takashi Kamiyama, Kazuhiro Mori, Makoto Maie, Takuro Nagai, Yoshio Matsui, and Eiji Takayama-Muromachi. High-

Pressure Synthesis, Crystal Structures, and Properties of Perovskite-like $BiAlO_3$ and Pyroxene-like $BiGaO_3$. *Chemistry of Materials*, 18(1):133–139, 2006.

[21] Nicole A. Benedek and Craig J. Fennie. Why are there so few perovskite ferroelectrics? *Journal of Physical Chemistry C*, 117(26):13339–13349, 2013.

[22] L. Benguigui. Disordered Ferroelectrics: $Ba_xSr_{1-x}TiO_3$ Single Crystals. *Physica Statis Solidi (A)*, 46(1):337–342, 1978.

[23] P. Berastegui, S. Hull, and S.-G. Eriksson. A low-temperature structural phase transition in $CsPbF_3$. *Journal of Physics: Condensed Matter*, 13:5077–5088, May 2001.

[24] D. D. Berkley, B. R. Johnson, N. Anand, K. M. Beauchamp, L. E. Conroy, A. M. Goldman, J. Maps, K. Mauersberger, M. L. Mecartney, J. Morton, M. Tuominen, and Y.-J. Zhang. In situ formation of superconducting $YBa_2Cu_3O_{7-x}$ thin films using pure ozone vapor oxidation. *Applied Physics Letters*, 53:1973, 1988.

[25] Satadeep Bhattacharjee, Eric Bousquet, and Philippe Ghosez. Engineering Multiferroism in $CaMnO_3$. *Physical Review Letters*, 102(11):117602, March 2009.

[26] H. Boschker, M. Huikben, A. Vailionis, J. Verbeeck, S. van Aert, M. Luysberg, S. Bals, G. van Tendeloo, E. P. Houwman, G. Koster, D. H. A. Blank, and G. Rijnders. Optimized fabrication of high-quality $La_{0.67}Sr_{0.33}MnO_3$ thin films considering all essential characteristics. *J. Phys. D: Appl. Phys.*, 44(20):205001, 2011.

[27] Matthew Brahlek, Lei Zhang, Hai-Tian Zhang, Jason Lapano, Liv. R. Dedon, Lane W. Martin, and Roman Engel-Herbert. Mapping growth windows in quaternary perovskite oxide systems by hybrid molecular beam epitaxy. *Appl. Phys. Lett.*, 109(10):101903, 2016.

[28] Wolfgang Braun. *Applied RHEED: Reflection High-Energy Electron Diffraction During*

Crystal Growth, volume 154 of *Springer Tracts in Modern Physics*. Springer, Berlin, Germany, 1999.

[29] N. E. Brese and M. O'Keeffe. Bond-valence parameters for solids. *Acta Crystallographica Section B Structural Science*, 47(2):192–197, April 1991.

[30] Jakoah Brgoch, Anna J. Lehner, Michael Chabinyc, and Ram Seshadri. Ab Initio Calculations of Band Gaps and Absolute Band Positions of Polymorphs of $RbPbI_3$ and $CsPbI_3$: Implications for Main-Group Halide Perovskite Photovoltaics. *Journal of Physical Chemistry C*, 118(48):27721–27727, 2014.

[31] Charles M. Brooks, Rajiv Misra, Julia A. Mundy, Lei A. Zhang, Kenneth R. Holinsworth, Brian S. O'Neal, Tassilo Heeg, Willi Zander, Jürgen Schubert, Janice L. Musfeldt, Zi-Kui Liu, David A. Muller, Peter Schiffer, and Darrell G. Schlom. The adsorption-controlled growth of $LuFe_2O_4$ by molecular-beam epitaxy. *Applied Physics Letters*, 101(13):132907, 2012.

[32] Ian David Brown. Bond Valences-A Simple Structural Model for Inorganic Chemistry. *Chemical Society Reviews*, 7:359–376, 1978.

[33] Ian David Brown. Recent developments in the methods and applications of the bond valence model. *Chemical reviews*, 109(12):6858–919, December 2009.

[34] Bulat Burganov, Carolina Adamo, Andrew Mulder, M. Uchida, P. D. C. King, J. W. Harter, D. E. Shai, A. S. Gibbs, A. P. Mackenzie, Reinhard Uecker, M. Bruetzam, M. R. Beasley, Craig J. Fennie, Darrell G. Schlom, and Kyle M. Shen. Strain control of fermiology and many-body interactions in two-dimensional ruthenates. *Physical Review Letters*, 116(19):197003, 2016.

[35] G. Catalan, A. Lubk, A. H. G. Vlooswijk, E. Snoeck, C. Magen, A. Janssens, Gijsbert Rispens, Guus J. H. M. Rijnders, Dave H. A. Blank, and Beatriz Noheda. Flexoelec-

tric rotation of polarization in ferroelectric thin films. *Nature Materials*, 10(12):963–967, 2011.

[36] S. Caticha-Ellis. Simultaneous reflections and the mosaic spread in a crystal plate. *Acta Crystallographica A*, 25(6):666–673, 1969.

[37] Shih-Lin Chang. *Multiple Diffraction of X-Rays in Crystals*, volume 50 of *Springer Series in Solid-State Sciences*. Springer-Verlag, Berlin, 1984.

[38] Samuel Chen, M. G. Mason, H. J. Gysling, G. R. Paz-Pujalt, T. N. Blanton, T. Castro, K. M. Chen, C. P. Fictorie, W. L. Gladfelter, A. Franciosi, P. I. Cohen, and J. F. Evans. Ultrahigh vacuum metalorganic chemical vapor deposition growth and in situ characterization of epitaxial TiO_2 films. *Journal of Vacuum Science and Technology A*, 11(5):2419–2429, 1993.

[39] A. Y. Cho. Epitaxy by periodic annealing. *Surface Science*, 17(2):494–503, 1969.

[40] A. Y. Cho. Morphology of Epitaxial Growth of GaAs by a Molecular Beam Method: The Observation of Surface Structures. *Journal of Applied Physics*, 41(7):2780–2786, 1970.

[41] A. Y. Cho. GaAs Epitaxy by a Molecular Beam Method: Observations of Surface Structure on the (001) Face. *Journal of Applied Physics*, 42(5):2074–2081, 1971.

[42] K. J. Choi, Michael Biegalski, Y. L. Li, A. Sharan, J. Schubert, Reinhard Uecker, P. Reiche, X. Q. Chen, Y. B. Pan, Venkatraman Gopalan, Long-Qing Chen, Darrell G. Schlom, and C. B. Eom. Enhancement of Ferroelectricity in Strained $BaTiO_3$ Thin Films. *Science*, 306:1005–1009, 2004.

[43] In Chung, Jung-Hwan Song, Jino Im, John Androulakis, Christos D. Malliakas, Hao Li, Arthur J. Freeman, John T. Kenney, and Mercouri G. Kanatzidis. $CsSnI_3$: Semiconductor or Metal? High Electrical Conductivity and Strong Near-Infrared Pho-

toluminescence from a Single Material. High Hole Mobility and Phase-Transitions. *Journal of the American Chemical Society*, 134(20):8579–8587, 2012.

[44] Ronald E Cohen. Origin of ferroelectricity in perovskite oxides. *Nature*, 358, 1992.

[45] Ronald E. Cohen and Henry Krakaur. Electronic structure studies of the differences in ferroelectric behavior of $BaTiO_3$ and $PbTiO_3$. *Ferroelectrics*, 136:65–83, 1992.

[46] H. Cole, F. W. Chambers, and H. M. Dunn. Simultaneous diffraction: Indexing umweganregung peaks in simple cases. *Acta Crystallographica*, 26:138, 1962.

[47] Douglas M. Collins. Pressure, density, and flux formulas of importance of molecular beam epitaxy. Technical Report CRM-346, Varian, 1979.

[48] B. D. Cullity and S. R. Stock. *Elements of X-Ray Diffraction*. Prentice Hall, Upper Saddle River, New Jersey, 2001.

[49] E. Lora da Silva, Jonathan M. Skelton, Stephen C. Parker, and Aron Walsh. Phase stability and transformations in the halide perovskite $CsSnI_3$. *Phys. Rev. B*, 91(14):144107, 2015.

[50] R. R. Das, D. M. Kim, S. H. Baek, C. B. Eom, F. Zavaliche, S. Y. Yang, Ramamoorthy Ramesh, Y. B. Chen, X. Q. Pan, X. Ke, M. S. Rzchowski, and S. K. Streiffer. Synthesis and ferroelectric properties of epitaxial $BiFeO_3$ thin films grown by sputtering. *Applied Physics Letters*, 88(24):242904, 2006.

[51] Mark E. Davis and Robert J. Davis. *Fundamentals of Chemical Reaction Engineering*. Dover Publications, Inc., Mineola, New York, 2003.

[52] Jaroslaw Z. Domagala, Sérgio L. Morelhão, Marcin Sarzynski, Marcin Mazdziarz, Pawel Dluzewski, and Michal Leszczynski. Hybrid reciprocal lattice: application to layer stress determination in GaAlN/GaN(0001) systems with patterned substrates. *Journal of Applied Crystallography*, 49, 2016.

[53] G. J. M. Dormans, P. J. van Veldhoven, and M. de Keijser. Composition-controlled growth of $PbTiO_3$ on $SrTiO_3$ by organometallic chemical vapour deposition. *Journal of Crystal Growth*, 123:537–544, 1992.

[54] Martin T. Dove. Theory of displacive phase transitions in minerals. *American Mineralogist*, 82:213–244, 1997.

[55] C. Eaton, J. A. Moyer, H. M. Alipour, E. D. Grimley, M. Brahlek, J. M. LeBeau, and R. Engel-Herbert. Growth of $SrVO_3$ thin films by hybrid molecular beam epitaxy. *J. Vac. Sci. Technol. A*, 33(6):061504, 2015.

[56] C.-J. Eklund, C. J. Fennie, and K. M. Rabe. Strain-induced ferroelectricity in orthorhombic $CaTiO_3$ from first principles. *Physical Review B*, 79(22):220101(R), June 2009.

[57] Eberhard Engel and Reiner M. Dreizler. *Density Functional Theory: An Advanced Course*. Springer-Verlag, Berlin, 2011.

[58] P. F. Fewster. X-ray analysis of thin films and multilayers. *Rep. Prog. Phys.*, 59:1339–1407, 1996.

[59] FIZ Karlsruhe. International Crystal Structure Database.

[60] D. D. Fong, A. M. Kolpak, J. A. Eastman, S. K. Streiffer, P. H. Fuoss, G. B. Stephenson, Carol Thompson, D. M. Kim, K. J. Choi, C. B. Eom, I. Grinberg, and A. M. Rappe. Stabilization of Monodomain Polarization in Ultrathin $PbTiO_3$ Films. *Phys. Rev. Lett.*, 96(12):127601, 2006.

[61] C. M. Foster, Z. Li, M. Buckett, D. Miller, P. M. Baldo, L. E. Rehn, G. R. Bai, D. Guo, H. You, and K. L. Merkle. Substrate effects on the structure of epitaxial $PbTiO_3$ thin films prepared on MgO, $LaAlO_3$, and $SrTiO_3$ by metalorganic chemical-vapor deposition. *Journal of Applied Physics*, 78(4):2607–2622, 1995.

[62] H. Freller and K. G. Günther. Three-temperature method as an origin of molecular beam epitaxy. *Thin Solid Films*, 88(4):291–307, 1982.

[63] Jarvist M. Frost, Keith T. Butler, Federico Brivio, Christopher H. Hendon, Mark van Schilfgaarde, and Aron Walsh. Atomistic Origins of High-Performance in Hybrid Halide Perovskite Solar Cells. *Nano Letters*, 14(5):2584–2590, 2014.

[64] Jarvist M. Frost, Keith T. Butler, and Aron Walsh. Molecular ferroelectric contributions to anomalous hysteresis in hybrid perovskite solar cells. *Applied Physics Letters: Materials*, 2(8):081506, August 2014.

[65] Y. Fujii, S. Hoshino, Y. Yamada, and G. Shirane. Neutron-scattering study on phase transitions of $CsPbCl_3$. *Physical Review B*, 9(10), 1974.

[66] M. Gajdos, K. Hummer, G. Kresse, J. Furthmüller, and F. Bechstedt. Linear optical properties in the projector-augmented wave methodology. *Phys. Rev. B*, 73(4):045112, 2006.

[67] E. Galdecka. *International Tables for Crystallography*, volume C, Section 5.3. International Union of Crystallography, 2006.

[68] A. C. Garcia-Castro, N A. Spaldin, A. H. Romero, and E. Bousquet. Geometric Ferroelectricity in Fluoroperovskites. *Physical Review B*, 89(10):104107, 2014.

[69] Philippe Ghosez, E. Cockayne, U. V. Waghmare, and K. M. Rabe. Lattice dynamics of $BaTiO_3$, $PbTiO_3$, and $PbZrO_3$: A comparative first-principles study. *Physical Review B*, 60(2):836–843, 1999.

[70] Peter M. W. Gill. *Encylopedia of Computational Chemistry*, chapter Density Functional Theory (DFT), Hartree-Fock (HF), and the Self-consistent Field. John Wiley and Sons, Limited, 1998.

[71] A. M. Glazer. The classification of tilted octahedra in perovskites. *Acta Crystallographica B*, 28(11):3384–3392, November 1972.

[72] Victor M. Goldschmidt. Die Gesetze der Krystallochemie. *Die Naturwissenschaften*, 21:477–485, 1926.

[73] Martin A. Green, Anita Ho-Baillie, and Henry Snaith. The emergence of perovskite solar cells. *Nature Photonics*, 8:506–514, 2014.

[74] I. Grinberg and A. M. Rappe. First principles calculations, crystal chemistry and properties of ferroelectric perovskites. *Phase Transitions*, 80(4-5):351–368, April 2007.

[75] K. G. Günther. Aufdampfschichten aus halbleitenden III-V-Verbindungen. *Die Naturwissenschaften*, 45(17):415–416, 1958.

[76] J. H. Haeni, P. Irvin, W. Chang, Reinhard Uecker, P. Reiche, Y. L. Li, S. Choudhury, W. Tian, M. E. Hawley, A. K. Craigo, B. Tagantsev, Xiaoqing Pan, S. K. Streiffer, Long-Qing Chen, S. W. Kirchoefer, J. Levy, and Darrell G. Schlom. Room-temperature ferroelectricity in strained $SrTiO_3$. *Nature*, 430:758–761, 2004.

[77] J. H. Haeni, C. D. Theis, D. G. Schlom, W. Tian, X. Q. Pan, H. Chang, I. Takeuchi, and X.-D. Xiang. Epitaxial growth of the first five members of the $Sr_{n+1}Ti_nO_{3n+1}$ Ruddlesden–Popper homologous series. *Applied Physics Letters*, 78(21):3292, 2001.

[78] J. H. Haeni, Chris D. Theis, and Darrell G. Schlom. RHEED Intensity Oscillations for the Stoichiometric Growth of $SrTiO_3$ Thin Films by Reactive Molecular Beam Epitaxy. *Journal of Electroceramics*, 4(2):385–391, 2000.

[79] Ryan C. Haislmaier, Everett D. Grimley, Michael D. Biegalski, James M. LeBeau, Susan Trolier-McKinstry, Venkatraman Gopalan, and Roman Engel-Herbert. Unleashing strain induced ferroelectricity in complex oxide thin films via precise stoichiometry control. *Advanced Functional Materials*, 26:7271–7279, 2016.

[80] D. J. Harra and T. W. Snouse. A radiant heated titanium sublimator. *J. Vac. Sci. Technol.*, 9(1):552–555, 1972.

[81] D. R. Hartree. The Wave Mechanics of an Atom with a Non-Coulomb Central Field. Part I. Theory and Methods. *Mathematical Procedings of the Cambridge Philosophical Society*, 24(1):89–110, 1928.

[82] R. Heckingbottom, G. J. Davies, and K. A. Prior. Growth and doping of gallium arsenide using molecular beam epitaxy (MBE): Thermodynamic and kinetic aspects. *Surface Science*, 132(1-3):375–389, 1983.

[83] Tassilo Heeg. *DOPICUv2: Distilled Ozone Process Integrated Control Unit v2.0*, 2010.

[84] C. Heikes. (private communication), May 2017.

[85] E. S. Hellman and J. S. Harris. Infra-red transmission electron spectroscopy of GaAs during molecular beam epitaxy. *Journal of Crystal Growth*, 81(1–4):38–42, 1987.

[86] Marian A. Herman and Helmut Sitter. *Molecular Beam Epitaxy: Fundamentals and Current Status*. Springer Series in Materials Science. Springer-Verlag, Berlin, second edition edition, 1996.

[87] P. Hohenberg and W. Kohn. Inhomogeneous electron gas. *Physical Review B*, 136(3):864–871, 1964.

[88] G. Höltzer, M. Fritsch, M. Deutsch, J. Härtwig, and E. Förster. $K\alpha_{1,2}$ and $K\beta_{1,3}$ x-ray emission lines of the 3*d* transition metals. *Physical Review A*, 56(6):4554–4568, 1997.

[89] M. Horváth, L. Bilitzky, and J. Jüttner. *Ozone*. Topics in Inorganic and General Chemistry. Elsevier Science Publishing Co., Inc., New York, 1985.

[90] Ling-yi Huang and Walter R. L. Lambrecht. Electronic band structure, phonons, and exciton binding energies of halide perovskites $CsSnCl_3$, $CsSnBr_3$, and $CsSnI_3$. *Physical Review B*, 88(16):165203, 2013.

[91] J. H. Hubbell and S. M. Seltzer. *X-Ray Mass Attenuation Coefficients*. https://www.nist.gov/pml/x-ray-mass-attenuation-coefficients. 21 September, 2016.

[92] J. F. Ihlefeld, A. Kumar, V. Gopalan, Darrell G. Schlom, Y. B. Chen, X. Q. Pan, Tassilo Heeg, Jürgen Schubert, X. Ke, P. Schiffer, J. Orenstein, L. W. Martin, Y. H. Chu, and R. Ramesh. Adsorption-controlled molecular-beam epitaxial growth of $BiFeO_3$. *Applied Physics Letters*, 91(07):071922, 2007.

[93] J. F. Ihlefeld, N. J. Podraza, Z. K. Liu, R. C. Rai, X. Xu, Tassilo Heeg, Y. B. Chen, J. Li, R. W. Collins, J. L. Musfeldt, X. Q. Pan, Jürgen Schubert, R. Ramesh, and Darrell G. Schlom. Optical band gap of $BiFeO_3$ grown by molecular-beam epitaxy. *Applied Physics Letters*, 92(14):142908, 2008.

[94] J. F. Ihlefeld, Wei Tian, Zi-Kui Liu, Alan W. Doolittle, Margitta Bernhagen, Peter Reiche, Reinhard Uecker, Ramamoorthy Ramesh, and Darrell G. Schlom. Adsorption-Controlled Growth of $BiFeO_3$ by MBE and Integration with Wide Band Gap Semiconductors. *IEEE Transactions on Ultrasonics, Ferroelectrics, and Frequency Control*, 56(8):1528–1533, 2009.

[95] Katsuhiko Inaba. X-ray thin-film measurement techniques. *The Rigaku Journal*, 24(1):10–15, 2008.

[96] International Union of Crystallography, March 2015.

[97] Bharat Jalan, Roman Engel-Herbert, Nicolas J. Wright, and Susanne Stemmer. Growth of high-quality $SrTiO_3$ films using a hybrid molecular beam epitaxy approach. *Journal of Vacuum Science and Technology A*, 27:461, 2009.

[98] Bharat Jalan, Pouya Moetakef, and Susanne Stemmer. Molecular beam epitaxy of $SrTiO_3$ with a growth window. *Appl. Phys. Lett.*, 95(03):032906, 2009.

[99] B.-S. Jeong, J. D. Budai, and D. P. Norton. Epitaxial stabilization of single crystal anatase films via reactive sputter deposition. *Thin Solid Films*, 422:166–169, 2002.

[100] Jing Ju, Dejun Wang, Jianhua Lin, Guobao Li, Jing Chen, Liping You, Fuhui Liao, Nianzu Wu, Huizhong Huang, and Guangqing Yao. Hydrothermal synthesis and structure of lead titanate pyrochlore compounds. *Chemistry of Materials*, 15:3530–3536, 2003.

[101] k Space Associates. *BANDiT*, Ann Arbor, MI.

[102] J. Kabelac, S. Ghosh, P. Dobal, and R. Katiyar. rf oxygen plasma assisted molecular beam epitaxy growth of $BiFeO_3$ thin films on $SrTiO_3$ (001). *Journal of Vacuum Science and Technology B*, 25(3):1049–1052, 2007.

[103] Jason K. Kawasaki, Masaki Uchida, Hanjong Paik, Darrell G. Schlom, and Kyle M. Shen. Evolution of electronic correlations across the rutile, perovskite, and ruddelsden-popper iridates with octahedral connectivity. *Physical Review B*, 94(12):121104(R), 2016.

[104] P. D. C. King, H. I. Wei, Yuefeng F. Nie, M. Uchida, Carolina Adamo, S. Zhu, X. He, I. Bozovic, Darrell G. Schlom, and Kyle M. Shen. Atomic-scale control of competing electronic phases in ultrathin $LaNiO_3$. *Nature Nanotechnology*, 9:443–447, 2014.

[105] Wolfram Koch and Roland H. Hertwig. *Encylopedia of Computational Chemistry*, chapter Density Functional Theory Applications to Transition Metal Problems. John Wiley and Sons, Limited, 1998.

[106] Wolfram Koch and Max C. Holthausen. *A Chemist's Guide to Density Functional Theory: Second Edition*. Wiley-VCH, Weinheim, 2001.

[107] Walter Kohn and L. J. Sham. Self-consistent equations including exchange and correlation effects. *Physical Review A*, 140(4):1133–1138, 1965.

[108] Akihiro Kojima, Kenjiro Teshima, Yasuo Shirai, and Tsutomu Miyasaka. Organometal Halide Perovskites as Visible-Light Sensitizers for Photovoltaic Cells. *Journal of the American Chemical Society*, 131(17):6050–6051, 2009.

[109] Richard Korytar, Miguel Pruneda, Javier Junquera, Pablo Ordejon, and Nicolas Lorente. Band selection and disentanglement using maximally localized Wannier functions: the cases of Co impurities in bulk copper and the Cu(111) surface. *Journal of Physics: Condensed Matter*, 22(38):385601, 2010.

[110] Gertjan Koster, Boike L. Kropman, Guus J. H. M. Rijnders, Dave H. A. Blank, and Horst Rogalla. Quasi-ideal strontium titanate crystal surfaces through formation of strontium hydroxide. *Applied Physics Letters*, 73(20):2920–2922, 1998.

[111] G Kresse and J Furthmüller. Efficient iterative schemes for ab initio total-energy calculations using a plane-wave basis set. *Physical Review B*, 54(16):11169–11186, October 1996.

[112] G. Kresse and J. Hafner. Ab initio molecular dynamics for liquid metals. *Physical Review B*, 47(1):558–561, 1993.

[113] G Kresse and D Joubert. From ultrasoft pseudopotentials to the projector augmented-wave method. *Physical Review B*, 59(3):1758–1775, 1999.

[114] Georg Kresse, Martijn Marsman, and Jürgen Furthmüller. *Vienna Ab-initio Simulation Package: VASP the GUIDE*. Computational Materials Physics, Faculty of Physics, Universität Wien, Sensengasse, Wien, Austria, April 2016.

[115] D. J. Kubinski, D. W. Hoffman, R. E. Soltis, and E. M. Logothetis. Reactive codeposition of in situ Y-Ba-Cu-O superconducting films using dilute mixtures of ozone in oxygen. *Journal of Applied Physics*, 71:1860–1867, 1992.

[116] A. I. Lebedev. Ab initio calculations of phonon spectra in $ATiO_3$ perovskite crystals (A = Ca, Sr, Ba, Ra, Cd, Zn, Mg, Ge, Sn, Pb). *Physics of the Solid State*, 51(2):362–372, February 2009.

[117] J. H. Lee, X. Ke, R. Misra, J. F. Ihlefeld, X. S. Xu, Z. G. Mei, Tassilo Heeg, M. Roeckerath, Jürgen Schubert, Zi-Kui Liu, J. L. Musfeldt, P. Schiffer, and Darrell G. Schlom. Adsorption-controlled growth of $BiMnO_3$ films by molecular-beam epitaxy. *Applied Physics Letters*, 96(26):262905, 2010.

[118] Michael M. Lee, Joël Teuscher, Tsutomu Miyasaka, Takurou N Murakami, and Henry J Snaith. Efficient hybrid solar cells based on meso-superstructured organometal halide perovskites. *Science*, 338(6107):643–7, November 2012.

[119] Wei Li, G. V. Gibbs, and S. Ted Oyama. Mechanism of Ozone Decomposition on a Manganese Oxide Catalyst. 1. In Situ Raman Spectroscopy and Ab Initio Molecular Orbital Calculations. *Journal of the American Chemical Society*, 120:9041–9046, 1998.

[120] Wei Li and S. Ted Oyama. Mechanism of Ozone Decomposition on a Manganese Oxide Catalyst. 2. Steady-State and Transient Kinetic Studies. *Journal of the American Chemical Society*, 120:9047–9052, 1998.

[121] Z. Li, C. M. Foster, D. Guo, H. Zhang, G. R. Bai, P. M. Baldo, and L. E. Rehn. Growth of high quality single-domain single-crystal films of $PbTiO_3$. *Applied Physics Letters*, 65:1106–1108, 1994.

[122] Malcolm E. Lines and A. M. Glass. *Principles and applications of ferroelectrics and related materials*. Clarendon Press: Oxford, U.K., 2001.

[123] Yang Liu, Hari P. Nair, Jacob P. Ruf, Darrell G. Schlom, and Kyle M. Shen. Revealing the Hidden Heavy Fermi Liquid in $CaRuO_3$. (unpublished).

[124] M. D. Losego, H. S. Craft, E. A. Paisley, S. Mita, R. Collazo, Z. Sitar, and J.-P. Maria. Critical examination of growth rate for magnesium oxide (MgO) thin films deposited by molecular beam epitaxy with a molecular oxygen flux. *J. Mater. Res.*, 25(4):670–679, 2010.

[125] M W Lufaso and P. M. Woodward. Prediction of the crystal structures of perovskites using the software program SpUDS. *Acta Crystallographica B*, 57:725, 2001.

[126] Richard I. Masel. *Principles of Adsorption and Reaction on Solid Surfaces*. Wiley Series in Chemical Engineering. John Wiley and Sons, Inc., 1996.

[127] Yuya Matsubara, Kei S. Takahashi, Yoshinori Tokura, and Masashi Kawasaki. Single-crystalline $BaTiO_3$ films grown by gas-source molecular beam epitaxy. *Applied Physics Express*, 7(12):125502, 2014.

[128] J. W. Matthews and A. E. Blakeslee. Defects in epitaxial multilayers. *Journal of Crystal Growth*, 27:118–125, 1974.

[129] S. J. May, P. J. Ryan, J. L. Robertson, J.-W. Kim, T. S. Santos, E. Karapetrova, J. L. Zarestky, X. Zhai, S. G. E. te Velthuis, J. N. Eckstein, S. D. Bader, and A. Bhattacharya. Enhanced ordering temperatures in antiferromagnetic manganite superlattices. *Nature Materials*, 8:892–897, 2009.

[130] Alan S. de Menezes, Adenilson O. dos Santos, Juliana M. A. Almeida, Jose R. R. Bortoleto, Monica A. Cotta, Sérgio L. Morelhão, and Lisandro P. Cardoso. Direct Observation of Tetragonal Distortion in Epitaxial Structures through Secondary Peak Split in a Synchrotron Radiation Renninger Scan. *Crystal Growth and Design*, 20:3436–3441, 2010.

[131] Shinji Migita, Yuji Kasai, Huroyuki Ota, and Shigeki Sakai. Self-limiting process for the bismuth content in molecular beam epitaxial growth of $Bi_2Sr_2CuO_y$ thin films. *Applied Physics Letters*, 71(25):3712–3714, 1997.

[132] Shinji Migita, Huroyuki Ota, H. Fujino, Yuji Kasai, and Shigeki Sakai. Epitaxial $Bi_4Ti_3O_{12}$ thin film growth using Bi self-limiting function. *Journal of Crystal Growth*, 200:161–168, 1999.

[133] MKS Technology for Productivity: ASTeC Products. *AX8401 Ozone Generator*.

[134] Pouya Moetakef, Jack Y. Zhang, Santosh Raghavan, Adam P. Kajdos, and Susanne Stemmer. Growth window and effect of substrate symmetry in hybrid molecular beam epitaxy of a Mott insulating rare earth titanate. *Journal of Vacuum Science and Technology A*, 31(04):041503, 2013.

[135] K. Momma and F. Izumi. VESTA 3 for three-dimensional visualization of crystal, volumetric and morphology data. *Journal of Applied Crystallography*, 44:1272–1276, 2011.

[136] Eric J. Monkman, Carolina Adamo, Julia A. Mundy, Daniel E. Shai, John W. Harter, Dawei Shen, Bulat Burganov, David A. Muller, Darrell G. Schlom, and Kyle M. Shen. Quantum many-body interactions in digital oxide superlattices. *Nature Materials*, 11:855–859, 2012.

[137] S. L. Morelhao and L. P. Cardoso. Structural properties of heteroepitaxial systems using hybrid multiple diffraction in Renninger scans. *Journal of Applied Physics*, 73(9):4218–4226, 1993.

[138] Sérgio L. Morelhão, H. Avanci, M. A. Hayashi, L. P. Cardoso, and S. P. Collins. Observation of coherent hybrid reflection with synchrotron radiation. *Applied Physics Letters*, 73(15):2194–2196, 1998.

[139] Sérgio L. Morelhão and Jarek Z. Domagala. Hybrid reciprocal space for x-ray diffraction in epitaxic layers. *Journal of Applied Crystallography*, 40:546–551, 2007.

[140] Sérgio L. Morelhão, A. A. Quivy, and J. Härtwig. Hybrid and effective satellites for studying superlattices. *Microelectronics Journal*, 34:695–699, 2003.

[141] Masahiro Mori and Haruo Saito. An x-ray study of successive phase transitions in $CsSnBr_3$. *Journal of Physics C*, 19(14):2391–2401, 1986.

[142] Arash A. Mostofi, Jonathan R. Yates, Young-Su Lee, Ivo Souza, David Vanderbilt, and Nicola Marzari. Wannier90: A Tool for Obtaining Maximally-Localized Wannier Functions. *Computer Physics Communications*, 178(9):685–699, 2008.

[143] J. A. Moyer, C. Eaton, and R. Engel-Herbert. Highly Conductive $SrVO_3$ as a Bottom Electrode for Functional Perovskite Oxides. *Advanced Materials*, 25:3578–3582, 2013.

[144] Hari Nair. Personal communication, April 2017.

[145] Hari Nair, J. P. Ruf, Y. Liu, N. Shukla, B. Grisafe, C. Chang, Q. Han, E. Levenson-Falk, M. Bernhagen, P. Reiche, Reinhard Uecker, Carolina Adamo, A. Kapitulnik, A. Millis, David A. Muller, S. Datta, Kyle M. Shen, and Darrell G. Schlom. Strain tuning of electronic ground state in Ca_2RuO_4 epitaxial thin films. Unpublished.

[146] C. T. Nelson, P. Gao, J. R. Jokisaari, C. Heikes, C. Adamo, A. Melville, S.-H. Baek, C. M. Folkman, B. Winchester, Y. Gu, Y. Liu, K. Zhang, E. Wang, J. Li, L.-Q. Chen, C.-B. Eom, D. G. Schlom, and X. Pan. Domain Dynamics During Ferroelectric Switching. *Science*, 334(6058):968–971, 2011.

[147] J. B. Nelson and D. P. Riley. An experimental investigation of extrapolation methods in the derivation of accurate unit-cell dimensions of crystals. *Proc. Phys. Soc. London*, 57:160, 1945.

[148] Yuefeng F. Nie, P. D. C. King, C. H. Kim, M. Uchida, H. I. Wei, Brendan D. Faeth, J. P. Ruf, J. P. C. Ruff, L. Xie, X. Pan, Craig J. Fennie, Darrell G. Schlom, and Kyle M. Shen.

Interplay of Spin-Orbit Interactions, Dimensionality, and Octahedral Rotations in Semimetallic $SrIrO_3$. *Physical Review Letters*, 114(01):016401, 2015.

[149] Julie Nucci. Personal communication.

[150] Online Dictionary of Crystallography. *Linear attenuation coefficient*. http://reference.iucr.org/dictionary/Linear˙attenuation˙coefficient. 20 May, 2017.

[151] D. Orobengoa, C. Capillas, M. I. Aroyo, and J. M. Perez-Mato. AMPLIMODES: symmetry-mode analysis on the Bilbao Crystallographic Server. *Journal of Applied Crystallography*, 42:820–833, 2009.

[152] Hanjong Paik. (private communication).

[153] Hanjong Paik, Ed Lochocki, Z. Chen, Ariel Seidner, Amit K. Verma, Nick Tanen, M. Uchida, S. L. Shang, B.-C. Zhou, Z. K. Liu, Debdeep Jena, David A. Muller, Kyle M. Shen, and Darrell G. Schlom. Adsorption-Controlled Growth of La-doped $BaSnO_3$ by Molecular-Beam Epitaxy. Manuscript in preparation.

[154] PANalytical. *X'Pert PRO: X-ray diffraction system*.

[155] PCI Ozone & Control Systems, Inc. West Caldwell, NJ.

[156] John P. Perdew, Adrienn Ruzsinszky, Gabor I. Csonka, Oleg A. Vydrov, Gustavo E. Scuseria, Lucian A. Constantin, Xiaolan Zhou, and Kieron Burke. Restoring the density-gradient expansion for exchange in solids and surfaces. *Physical Review Letters*, 100(13):136406, 2008.

[157] J M Perez-Mato, D Orobengoa, and M I Aroyo. Mode crystallography of distorted structures. *Acta Crystallographica A*, 66(5):558–90, September 2010.

[158] Warren E. Pickett. Pseudopotential methods in condensed matter applications. *Computer Physics Reports*, 9(3):115–198, 1989.

[159] Finn Reibke Poulsen and Svend Erik Rasmussen. Crystal structure and phase transition of cesium trichlorostannate(II). *Acta Chemica Scandinavica*, 24(1):150–156, 1970.

[160] Abhinav Prakash, Peng Xu, Xuewang Wu, Greg Haugstad, Xiaojia Wang, and Bharat Jalan. Adsorption-controlled growth and the influence of stoichiometry on electronic transport in hybrid molecular beam epitaxy-grown $BaSnO_3$ films. *Journal of Materials Chemistry C*, 2017.

[161] Karin M. Rabe, Charles H. Ahn, and Jean-Marc Triscone, editors. *Physics of Ferroelectrics: A Modern Perspective*, volume 105 of *Topics in Applied Physics*. Springer: Berlin, Germany, 2007.

[162] S. Raghavan, T. Schumann, H. Kim, J. Y. Zhang, T. A. Cain, and S. Stemmer. High-mobility $BaSnO_3$ grown by oxide molecular beam epitaxy. *APL Mater.*, 4(01):016106, 2016.

[163] Ramamoorthy Ramesh and Nicola A. Spaldin. Multiferroics: progress and prospects in thin films. *Naterual Materials*, 6:21–29, 2007.

[164] M. Renninger. "umweganregung," eine bisher unbeachtete wechselwirkungserscheinung bei raumgitterinterferenzen. *Zeitschrift für Physik*, 106(3):141–176, 1937.

[165] G. Rispens and B. Noheda. Ultra-thin Lead Titanate Films Grown by Molecular Beam Epitaxy. *Integr. Ferroelectr.*, 92(1):30–39, 2007.

[166] Gijsbert Rispens. *Strain and composition effects in epitaxial ferroelectrics: Structural studies on PbxSr1-xTiO3 thin films grown by MBE*. PhD thesis, University of Groningen, Zernike Institute for Advanced Materials, 2010.

[167] Elisabeth Rossmanith. Approximate calculation of multiple-diffraction patterns

based on Renninger's kinematical 'simplest approach'. *Journal of Applied Crystallography*, 33:921–927, 2000.

[168] W. L. Roth and R. C. Devries. Crystal and Magnetic Structure of $PbCrO_3$. *Journal of Applied Physics*, 38(3):951–952, 1967.

[169] S. N. Ruddlesden and P. Popper. New compounds of the K_2NIF_4 type. *Acta Crystallographica*, 10(8):538–539, August 1957.

[170] S. N. Ruddlesden and P. Popper. The compound $Sr_3Ti_2O_7$ and its structure. *Acta Crystallographica*, 11:54–55, 1958.

[171] Akihito Sawa, Haruhiko Obara, and Shin Kosaka. Effect of using pure ozone on in situ molecular beam epitaxy of $YBa_2Cu_3O_{7-x}$ thin films at low pressure. *Applied Physics Letters*, 64:649–651, 1994.

[172] Darrell G. Schlom. Epitaxial vs. textured vs. randomly-oriented films. Personal communication.

[173] Darrell G. Schlom. Perspective: Oxide molecular-beam epitaxy rocks! *APL Materials*, 3(06):062403, 2015.

[174] Darrell G. Schlom, Long-Qing Chen, Ziaoqing Pan, Andreas Schmehl, and Mark A. Zurbuchen. A thin films approach to engineering functionality into oxides. *Journal of the American Ceramic Society*, 91(8):2429–2454, 2008.

[175] Darrell G. Schlom and James S. Harris Jr. *Molecular beam epitaxy: Applications to Key Materials*, chapter Chapter 6: MBE Growth of High Tc Superconductors. Noyes Publications, 1995.

[176] Darrell G. Schlom, A. F. Marshall, J. T. Sizemore, Z. J. Chen, J. N. Eckstein, I. Bozovic, K. E. von Dessonneck, J. S. Harris Jr., and J. C. Bravman. Molecular beam epitaxial

growth of layered Bi-Sr-Ca-Cu-O compounds. *Journal of Crystal Growth*, 102:361–375, 1990.

[177] Hisashi Seki and Akinori Koukitu. Thermodynamic Analysis of Molecular Beam Epitaxy of III-V Semiconductors. *Journal of Crystal Growth*, 78(2):342–352, 1986.

[178] D. E. Shai, Carolina Adamo, D. W. Shen, Charles M. Brooks, J. W. Harter, Eric J. Monkman, Bulat Burganov, Darrell G. Schlom, and Kyle M. Shen. Quasiparticle Mass Enhancement and Temperature Dependence of the Electronic Structure of Ferromagnetic $SrRuO_3$ Thin Films. *Physical Review Letters*, 119(08):087004, 2013.

[179] R. D. Shannon. Revised Effective Ionic Radii and Systematic Studies of Interatomie Distances in Halides and Chaleogenides. *Acta Crystallographica A*, 32:751–767, 1976.

[180] Gen Shirane and Sadao Hoshino. On the phase transition in lead titanate. *Journal of the Physical Society of Japan*, 6(4):265–270, 1951.

[181] V. B. Shirokov, Yu. I. Yuzyuk, B. Dkhil, and V. V. Lemanov. Phenomenological theory of phase transitions in epitaxial $Ba_xSr_{1-x}TiO_3$ thin films. *Physical Review B*, 79(14):144118, 2009.

[182] V. B. Shirokov, Yu. I. Yuzyuk, and V. V. Lemanov. Phenomenological Description of thin $SrTiO_3$ Films. *Lattice Dynamics and Phase Transitions*, 51(5):1025–1032, 2009.

[183] Eva H. Smith, Nicole A. Benedek, and Craig J. Fennie. Interplay of Octahedral Rotations and Lone Pair Ferroelectricity in $CsPbF_3$. *Inorganic Chemistry*, 54(17):8536–8543, 2015.

[184] Eva. H. Smith, J. F. Ihlefeld, Zi-Kui Liu, Hanjong Paik, Yuefeng Nie, Carolina Adamo, Tassilo Heeg, and Darrell G. Schlom. Exploiting kinetics and thermodynamics to grow phase-pure complex oxides by molecular-beam epitaxy under continuous codeposition. Manuscript in press.

[185] Eva H. Smith, Yakun Yuan, Byron Lara, Haricharan Padmanabhan, Venkatraman Gopalan, and Darrell G. Schlom. Thermal conductivity of $Ba_xSr_{1-x}TiO_3$ thin films. Unpublished.

[186] Harold T. Stokes, Dorian M. Hatch, and Branton J. Campbell. ISOTROPY software suite, 2014.

[187] Matthew W Stoltzfus, Patrick M Woodward, Ram Seshadri, Jae-hyun Klepeis, and Bruce Bursten. Structure and Bonding in $SnWO_4$, $PbWO_4$, and $BiVO_4$: Lone Pairs vs Inert Pairs. *Inorganic Chemistry*, 46(10):3839–3850, 2007.

[188] S. Stoughton, M. Showak, Q. Mao, P. Koirala, D. A. Hillsberry, S. Sallis, Lena Fitting Kourkoutis, K. Nguyen, L. F. J. Piper, D. A. Tenne, N. J. Podraza, David A. Muller, Carolina Adamo, and Darrell G. Schlom. Adsorption-controlled growth of $BiVO_4$ by molecular-beam epitaxy. *APL Materials*, 1(04):042112, 2013.

[189] Constantinos C. Stoumpos, Christos D. Malliakas, and Mercouri G. Kanatzidis. Semiconducting Tin and Lead Iodide Perovskites with Organic Cations: Phase Transitions, High Mobilities, and Near-Infrared Photoluminescent Properties. *Inorganic Chemistry*, 52(15):9019–9038, 2013.

[190] Chris D. Theis and Darrell G. Schlom. Cheap and stable titantium source for use in oxide molecular beam epitaxy systems. *Journal of Vacuum Science and Technology A*, 14:2677–2679, 1996.

[191] Chris D. Theis and Darrell G. Schlom. Epitaxial lead titanate grown by MBE. *Journal of Crystal Growth*, 174:473–479, 1997.

[192] Chris D. Theis, J. Yeh, Darrell G. Schlom, M. E. Hawley, and G. W. Brown. Adsorption-controlled growth of $PbTiO_3$ by reactive molecular beam epitaxy. *Thin Solid Films*, 325:107–114, 1998.

[193] Chris D. Theis, J. Yeh, Darrell G. Schlom, M. E. Hawley, G. W. Brown, J. C. Jiang, and X. Q. Pan. Adsorption-controlled growth of $Bi_4Ti_3O_{12}$ by reactive MBE. *Applied Physics Letters*, 72(22):2817–2819, 1998.

[194] Gerhard Thiele, Heinz Wilhelm Rotter, and Klaus Dieter Schmidt. Kristallstrukturen und Phasentransformationen von Caesiumtrihalogenogermanaten(II) $CsGeX_3$ (X = CI, Br, I). *Zeitschrift fur anorganische und allgemeine Chemie*, 545:148–156, 1987.

[195] N. W. Thomas. The compositional dependence of octahedral tilting in orthorhombic and tetragonal perovskites. *Acta Crystallographica B*, 52(1):16–31, February 1996.

[196] N. W. Thomas and A. Beitollahi. Inter-relationship of octahedral geometry, polyhedral volume ratio and ferroelectric properties in rhombohedral perovskites. *Acta Crystallographica B*, 50(5):549–560, October 1994.

[197] W. Tian, J. H. Haeni, Darrell G. Schlom, E. Hutchinson, B. L. Sheu, M. M. Rosario, P. Schiffer, Y. Liu, Mark A. Zurbuchen, and Xiaoqing Pan. Epitaxial growth and magnetic properties of the first five members of the layered $Sr_{n+1}Ru_nO_{3n+1}$ oxide series. *Applied Physics Letters*, 90(09):022507, 2007.

[198] W. Tian, Xiaoqing Pan, J. H. Haeni, and Darrell G. Schlom. Transmission electron microscopy study of n = 1-5 $Sr_{n+1}TinO_{3n+1}$ epitaxial thin films. *Journal of Materials Research*, 16(7):2013–2026, 2001.

[199] A. Togo, F. Oba, and I. Tanaka. First-principles calculations of the ferroelastic transition between rutile-type and $CaCl_2$-type SiO_2 at high pressures. *Physical Review B*, 78(13):134106, 2008.

[200] D. M. Trots and S. V. Myagkota. High-temperature structural evolution of caesium and rubidium triiodoplumbates. *Journal of Physics and Chemistry of Solids*, 69(10):2520–2526, 2008.

[201] J. Y. Tsao. Phase equilibria during InSb molecular beam epitaxy. *Journal of Crystal Growth*, 110(3):595–603, 1991.

[202] Jeffrey Y. Tsao. *Materials Fundamentals of Molecular Beam Epitaxy*. Academic Press, Boston, 1993.

[203] M. Uchida, Y. F. Nie, P. D. C. King, C. H. Kim, C. J. Fennie, D. G. Schlom, and K. M. Shen. Correlated vs. conventional insulating behavior in the $J_{\text{eff}} = \frac{1}{2}$ vs. $\frac{3}{2}$ bands in the layered iridate Ba_2IrO_4. *Phys. Rev. B*, 90(07):075142, 2014.

[204] Ross W. Ulbricht, Andreas Schmehl, Tassilo Heeg, Jürgen Schubert, and Darrell G. Schlom. Adsorption-controlled growth of EuO by molecular-beam epitaxy. *Applied Physics Letters*, 93(10):102105, 2008.

[205] J. H. Van der Merwe. Crystal Interfaces. Part I. Semi-Infinite Crystals. *Journal of Applied Physics*, 34(1):117–122, 1963.

[206] Sriram Venkatesan, Ard Vlooswijk, Bart J. Kooi, Alessio Morelli, George Palasantzas, Jeff T. M. De Hosson, and Beatriz Noheda. Monodomain strained ferroelectric $PbTiO_3$ thin films: Phase transition and critical thickness study. *Physical Review B*, 78(10):104112, 2008.

[207] U. Waghmare, N. Spaldin, H. Kandpal, and Ram Seshadri. First-principles indicators of metallicity and cation off-centricity in the IV-VI rocksalt chalcogenides of divalent Ge, Sn, and Pb. *Physical Review B*, 67(12):125111, 2003.

[208] Aron Walsh, David J Payne, Russell G Egdell, and Graeme W Watson. Stereochemistry of post-transition metal oxides: revision of the classical lone pair model. *Chemical Society reviews*, 40(9):4455–63, September 2011.

[209] Yuguo Wang, Peilin Zhang, Baodong Qu, and Weilie Zhong. Oriented pbtio3 films from metalorganic percursors. *Journal of Applied Physics*, 71(12):6121, 1992.

[210] Z. Wang, H. Paik, A. Seidner, Z. Chen, D. A. Muller, and D. G. Schlom. Adsorption-controlled growth of $PbZrO_3$ thin film via molecular-beam epitaxy. (unpublished).

[211] Maitri P. Warusawithana, Cheng Cen, Charles R. Sleasman, Joseph C. Woicik, Yulan Li, Lena Fitting Kourkoutis, Jeffrey A. Klug, Hao Li, Philip Ryan, Li-Peng Wang, Michael Bedzyk, David A. Muller, Long-Qing Chen, Jeremy Levy, and Darrell G. Schlom. A ferroelectric oxide made directly on silicon. *Science*, 324:367, 2009.

[212] Kiyotaka Wasa, Makoto Kitabatake, and Hideaki Adachi. *Thin Film Materials Technology: Sputtering of Compound Materials*. William Andrew, Inc.; Springer-Verlag GmbH and Co. KG, 2004.

[213] K. M. Welch. *Capture Pumping Technology, An Introduction, 1st ed.*, pages 210–212. Pergamon, New York, 1991.

[214] Anthony R. West. *Basic Solid State Chemistry, Second Edition*. John Wiley and Sons, Limited, 1999.

[215] P. M. Woodward. Octahedral Tilting in Perovskites. II. Structure Stabilizing Forces. *Acta Crystallographica Section B Structural Science*, 53(1):44–66, February 1997.

[216] A. K. Yadav, C. T. Nelson, S. L. Hsu, Z. Hong, J. D. Clarkson, C. M. Schlepütz, A. R. Damodaran, P. Shafer, E. Arenholz, L. R. Dedon, D. Chen, A. Vishwanath, A. M. Minor, L. Q. Chen, J. F. Scott, L. W. Martin, and R. Ramesh. Observation of polar vortices in oxide superlattices. *Nature*, 530:198–201, 2016.

[217] Y. Yamane, K. Yamada, and K. Inoue. Mechanochemical synthesis and order-disorder phase transition in fluoride ion conductor $RbPbF_3$. *Solid State Ionics*, 179(605-610), 2008.

[218] M. H. Yang and C. P. Flynn. Growth of Alkali Halides from Molecular Beams: Global Growth Characteristics. *Physical Review Letters*, 62(21), 1989.

[219] Hai-Tian Zhang, Liv. R. Dedon, Lane W. Martin, and Roman Engel-Herbert. Self-regulated growth of $LaVO_3$ thin films by hybrid molecular beam epitaxy. *Applied Physics Letters*, 106(23):233102, 2015.

[220] W Zhong, Rd King-Smith, and D Vanderbilt. Giant LO-TO splittings in perovskite ferroelectrics. *Physical review letters*, 72(22):3618–3621, May 1994.